MICROFLUIDIC LABEL-FREE FERROHYDRODYNAMIC CELL SEPARATION

by

WUJUN ZHAO

(Under the Direction of Leidong Mao and Jin Xie)

ABSTRACT

Microfluidic cell separation based on negative magnetophoresis in ferrofluids (ferrohydrodynamics) has unique advantages over other competing techniques. Magnetic force does not interact directly with cells, minimizing potential detrimental effects on them. Systems based on negative magnetophoresis are simple and low-cost, only requiring microchannels and permanent magnets or electromagnetic coils. As a result, negative magnetophoresis has been used to manipulate particles and cells. Negative magnetophoresis also eliminates the labeling steps through the incorporation of a special medium into the assay. This medium, typically magnetic liquids such as a paramagnetic salt solution or a ferrofluid, possesses a larger magnetization than the cells. An external magnetic field attracts the magnetic medium, which causes the cells to be preferentially pushed away. Consequently, cells can be manipulated magnetically without the need for labeling them. A water-based biocompatible ferrofluid that not only maintains its colloidal stability under strong magnetic fields but also keeps cells alive was developed for cell separation. Ferrohydrodynamic cell separation in this biocompatible ferrofluids offered moderate throughput (~10^6 cells h^{-1} in this study) and extremely high separation efficiency (>99%) for HeLa and blood cells without the use of labels. A microfluidic

device was further designed and optimized specifically to shorten the time of live cells' exposure to ferrofluids from hours to seconds, by eliminating time-consuming off-chip sample preparation and extraction steps and integrating them on-chip to achieve a one-step process. As a proof-of-concept demonstration, a ferrofluid with 0.26% volume fraction was used in this microfluidic device to separate spiked cancer cells from cell lines at a concentration of ~100 cells per mL from white blood cells with a throughput of 1.2 mL h^{-1}. The average separation efficiency was 82.2% and the separated cancer cells' purity was between 25.3%-28.8%. Later, we demonstrated the development of a laminar-flow microfluidic device that was capable of enriching rare circulating tumor cells from patients' blood in a biocompatible manner with a high throughput (6 mL h^{-1}) and a high rate of recovery (92.9%). Biocompatibility study on lung and breast cancer cell lines showed that separated cancer cells had excellent short-term viability, normal proliferation and unaffected key biomarker expressions.

INDEX WORDS: Microfluidics, Ferrofluids, Label-Free, Ferrohydrodynamics, Cell Separation, Circulating Tumor Cell

MICROFLUIDIC LABEL-FREE FERROHYDRODYNAMIC CELL SEPARATION

by

WUJUN ZHAO

BE, Jilin University, China, 2013

A Dissertation Submitted to the Graduate Faculty of The University of Georgia in Partial Fulfillment of the Requirements for the Degree

DOCTOR OF PHILOSOPHY

ATHENS, GEORGIA

2018

MICROFLUIDIC LABEL-FREE FERROHYDRODYNAMIC CELL SEPARATION

by

WUJUN ZHAO

Major Professor:	Leidong Mao
	Jin Xie
Committee:	Cheryl Gomillion
	Melissa Davis

Electronic Version Approved:

Suzanne Barbour
Dean of the Graduate School
The University of Georgia
May 2018

DEDICATION

I am grateful for all the supports from my advisor, committee, collaborator, colleague, and family.

ACKNOWLEDGEMENTS

I gratefully acknowledge the financial support from the National Science Foundation (award no. ECCS-1150042), National Institutes of Health (award no. R21GM104528), and seed grant programs between The University of Georgia/Centers for Disease Control and Prevention and The University of Georgia/Augusta University.

TABLE OF CONTENTS

Page

LIST OF TABLES

Page

LIST OF FIGURES

Page

CHAPTER 1

INTRODUCTION AND LITERATURE REVIEW (LABEL-FREE MICROFLUIDIC MANIPULATION OF PARTICLES AND CELLS IN MAGNETIC LIQUIDS) [1]

1.1 Introduction

Microfluidic particle and cell manipulation has brought significant advances to disease diagnostics,[1-5] therapeutics,[6-8] environmental monitoring,[9] and single-cell studies.[10-12] Traditional technologies for particle and cell manipulation (*e.g.*, FACS – fluorescence-activated cell sorting) have been developed for cell enrichment.[13] However, they are often labor-intensive and require "labels" to identify cells of interest. In addition, high costs of such systems, along with operating and reagent costs, limit their broader adoption.[14] On the other hand, manipulation specificity of existing microfluidic techniques often exploits intrinsic physical properties of particles and cells, such as their differences in size, shape, density, deformability, electric and magnetic properties, for fast and efficient applications including separation and focusing.[14-18] These applications and their working principles are well documented in a series of recent review articles.[14, 16, 18]. Among these reviews are techniques based on interactions between external energy inputs and particles or cells, which include dielectrophoresis, optical forces, acoustophoresis and magnetophoresis. Dielectrophoresis[19] enables manipulation of cells in non-uniform electric fields. The alternating fields, however, may polarize a cell's membrane and disrupt normal metabolic function. Optical tweezers[20] employ force

[1] W. Zhao, R. Cheng, J. R. Miller and L. Mao, *Adv Funct Mater*, 2016, **26**, 3916-3932. Reprinted here with permission of John Wiley and Sons.

exerted by a laser beam to manipulate cells. This method is usually applied to a single object, and heating from the laser beam can potentially denature biological entities. Acoustophoresis[21] uses acoustic forces generated on-chip to manipulate particles and cells based on their sizes and densities. Its high cost for experimental setup may pose a challenge for the wide application of acoustophoresis.

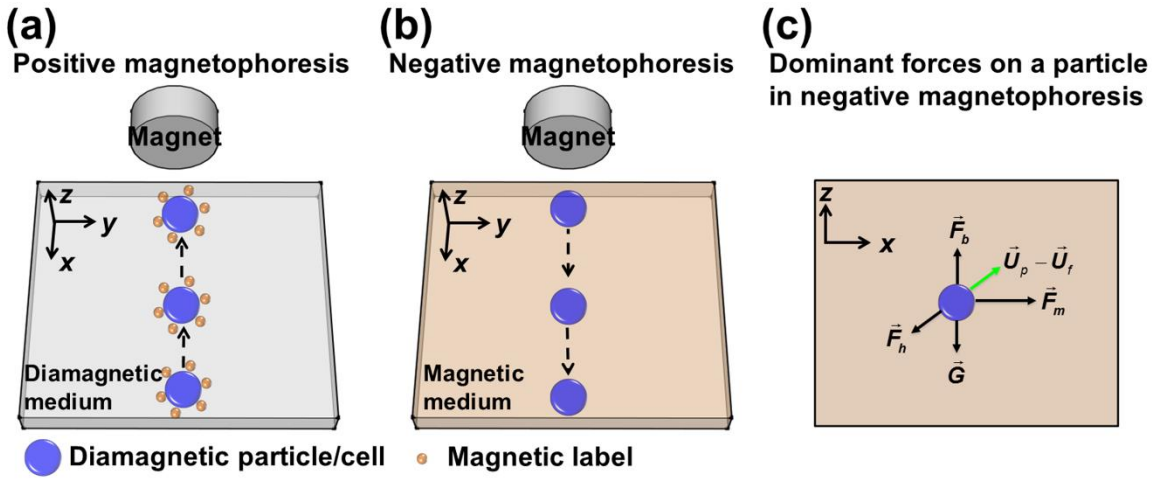

Figure 1.1: Working principles of positive and negative magnetophoresis and dominant forces. (a) Positive magnetophoresis – magnetization of diamagnetic particles/cells labeled with magnetic beads is larger than its surrounding medium; particles/cells move towards the location of field maxima when a magnetic field is applied. (b) Negative magnetophoresis –magnetization of diamagnetic particles/cells is less than its surrounding medium; particles/cells move towards the location of field minima when a magnetic field is applied. (c) Dominate forces include magnetic force $\vec{F}_m$, hydrodynamic drag force $\vec{F}_h$, gravitational force $\vec{G}$, and buoyancy force $\vec{F}_b$ on a particle in negative magnetophoresis. $\vec{U}_p$ is the velocity of the particle and $\vec{U}_f$ is the velocity of the medium flow.

Using magnetic beads for microfluidic cell manipulation, often referred to as "positive magnetophoresis" or simply "magnetophoresis" (see Figure 1.1a), is an attractive technology when compared to other competing ones, such as dielectrophoresis.[22-25] The magnetic force is an "action at a distance"; it is not directly in

contact with cells, minimizing potential hazardous effects that can reduce the viability of cells, which is typically associated with dielectrophoresis. This force depends on the magnetic moment of a particle or a cell and the gradient of external magnetic fields.[26-28] Underlying principles and applications of positive magnetophoresis have been previously reviewed.[22-25, 29] A typical application of positive magnetophoresis is the manipulation of magnetically labeled cells. It involves first labeling cells of interest with magnetic beads to render the cell-bead conjugate magnetic. Because the magnetization of beads is larger than its surrounding medium (*e.g.*, water), cell-bead conjugates are magnetized under external fields and therefore move towards the location of field maxima. As a result, cells of interest can be manipulated (*e.g.*, resulting in separation, trapping, focusing) from the rest of the sample. Microfluidic positive magnetophoresis has been developed to separate beads with different magnetic susceptibilities,[30, 31] and cells with different distributions of magnetic nanoparticles.[32, 33] However, this technology has several limitations. First, it uses magnetic beads for labeling in order to achieve specific manipulation and separation. The process of incubating cells with magnetic beads can take up to several hours, and multiple washing steps are needed,[32, 33] rendering the whole assay time-consuming and manually intensive. Second, manipulation specificity of positive magnetophoresis depends on the magnetic moment of beads or loading of magnetic nanoparticles in cells. Magnetic moments of beads can vary dramatically even in the same batch due to their manufacturing process.[28, 34-36] Third, loading of magnetic nanoparticles in cells is greatly affected by their endocytotic capacities or ligand-receptor interactions and can vary among the same type of cells.[32, 33, 37] Clearly, it is highly beneficial to retain the benefits

of positive magnetophoresis while eliminating the labeling step, in which cells and magnetic beads must be incubated together for a long period prior to manipulation.

A recent magnetic manipulative technique, termed "negative magnetophoresis" (also referred to as diamagnetophoresis) (see Figure 1.1b),[26] is label-free and can address the above-mentioned problems.[38, 39] The principle of negative magnetophoresis is exactly the opposite of positive magnetophoresis. Particles or cells to be manipulated in this case are less magnetic (diamagnetic in most cases) than that of their surrounding medium, which is typically a magnetic liquid such as a paramagnetic salt solution[40, 41] or a ferrofluid.[38, 42] Particles or cells placed inside a magnetic liquid act as "magnetic holes".[43] An externally applied magnetic field gradient attracts the liquid medium, which causes the cells to be preferentially pushed away.[27] As such, particles or cells inside these magnetic liquids can be potentially manipulated towards a weaker field direction without the time-consuming labeling step. The force acting on them is named as magnetic buoyancy force, which is a body force and is proportional to the volume of particle or cell.[27] A typical application of negative magnetophoresis is size-based cell separation, which does not need any magnetic tags for labeling. Cells of different sizes are simply injected into a continuous-flow microfluidic channel filled with magnetic liquids. Balanced by a viscous drag force, large cells experience more magnetic buoyancy force than smaller ones, resulting in a spatial separation between the two species at the end of the channel.[42, 44] The advantages of negative magnetophoresis include the following. First, it is a label-free manipulation, which can potentially reduce the time and cost associated with label-based assays. Second, a typical setup for negative magnetophoresis is very simple and low-cost, only requiring a microchannel and a permanent magnet in

most cases. Third, magnetic liquids can potentially be made biocompatible,[39, 45] which may enable live cell manipulation for certain cell types. However, it is important to note that biocompatibility of magnetic liquids is still a work in progress. Both short-term viability and long-term cellular functions (*e.g.*, proliferation, gene expression, and nanoparticle uptake) need to be carefully studied for each cell type to determine whether a specific magnetic liquid is truly biocompatible.

The goal of this chapter is to review the fundamental principles of negative magnetophoresis and its recent applications in the microfluidic manipulation of particles and cells. The remaining sections of the chapter are structured as follows. First, we introduce the commonly used specificities of manipulation in magnetic liquids, which include size, density and magnetic property of particles and cells. Second, we review and compare the media used in negative magnetophoresis, which includes paramagnetic salt solutions and ferrofluids. Third, we summarize the existing microfluidic applications of negative magnetophoresis, including separation, focusing, trapping, etc., and compare their performance. In addition, we also discuss the biocompatibility of magnetic liquids that is critical for live cell manipulation. Finally, we present an outlook for this new and exciting research field.

1.2 Dominant Forces

The types of forces in microfluidic systems, especially in positive and negative magnetophoresis, have been summarized in several review articles.[23, 24, 29] The most relevant ones among them are magnetic force, hydrodynamic viscous drag force, and gravitational/buoyant forces that are depicted in Figure 1.1c. Other forces including surface DLVO (*Derjaguin-Landau-Verwey-Overbeek*) force, Brownian motion, particle

and fluid interaction, and interparticle effects are secondary in nature; therefore, we neglect them in this chapter.[46]

1.2.1 Magnetic Force

A general expression for the magnetic force $\vec{F}_m$ on a magnetized body in a magnetic liquid under a magnetic field is shown in Equation (1.1).[27] Here $\mu_0 = 4\pi \times 10^{-7}$ H m^{-1} is the permeability of free space, V is the volume of the magnetized body, typically a spherical particle or cell with diameter of D_p, $\vec{M}_p$ is its magnetization (close to zero for most cells), $\vec{M}_f$ is magnetization of the magnetic liquid surrounding the body, and $\vec{H}$ is magnetic field strength at the center of the body.

$$\vec{F}_m = \mu_0 V\left[\left(\vec{M}_p - \vec{M}_f\right)\cdot\nabla\right]\vec{H} = \frac{\pi\mu_0 D_p^{\,3}}{6}\left[\left(\vec{M}_p - \vec{M}_f\right)\cdot\nabla\right]\vec{H} \tag{1.1}$$

For particle and cell manipulation in paramagnetic salt solutions or ferrofluids under weak magnetic fields, magnetizations of both the body $\vec{M}_p$ and the magnetic liquid $\vec{M}_f$ depend approximately linearly on the applied field, resulting in $\vec{M}_p = c_p\vec{H}$ and $\vec{M}_f = c_f\vec{H}$, where c_p and c_f are the dimensionless volume magnetic susceptibilities of the body and the magnetic liquid, respectively. Therefore, the magnetic force under a weak field approximation takes the form of Equation (1.2), which is often cited in the literature.[22-24] Here $\vec{B}$ is magnetic flux density.

$$\vec{F} = \frac{V\left(\chi_p - \chi_f\right)}{\mu_0}\left(\vec{B}\cdot\nabla\right)\vec{B} = \frac{\pi D_p^{\,3}\left(\chi_p - \chi_f\right)}{6\mu_0}\left(\vec{B}\cdot\nabla\right)\vec{B} \tag{1.2}$$

For particle and cell manipulation in ferrofluids under strong magnetic fields, Equation (1.2) is no longer valid as the magnetization of a superparamagnetic particle depends nonlinearly on the applied field, as does the magnetization of a ferrofluid. Both the superparamagnetic particle and ferrofluid can be modeled accurately by the classical Langevin theory. Langevin theory considers magnetic nanoparticles in a superparamagnetic particle and a ferrofluid as a collection of monodispersed and non-interacting magnetic dipoles.[27] This approach leads to the Langevin function of magnetization[27] in Equations (1.3) and (1.4). Here $a_p = \pi\mu_0 M_{p,b} H d_p^3 / 6k_B T$ and $a_f = \pi\mu_0 M_{f,b} H d_f^3 / 6k_B T$. f_p and f_f are volume fractions of the magnetic materials, $M_{p,b}$ and $M_{f,b}$ are saturation moments of the bulk magnetic materials, and d_p and d_f are diameters of nanoparticles in a superparamagnetic microparticle and a ferrofluid, respectively. k_B is the Boltzmann constant, T is temperature.

$$\frac{\vec{M}_p}{\phi_p \vec{M}_{p,b}} = L(\alpha_p) = \coth(\alpha_p) - \frac{1}{\alpha_p} \tag{1.3}$$

$$\frac{\vec{M}_f}{\phi_f \vec{M}_{f,b}} = L(\alpha_f) = \coth(\alpha_f) - \frac{1}{\alpha_f} \tag{1.4}$$

In the case of positive magnetophoresis, the magnetization of the superparamagnetic particle $\vec{M}_p$ is always larger than its surrounding medium $\vec{M}_f$. Under a non-uniform magnetic field, the direction of the magnetic force $\vec{F}_m$ on the particle is pointing towards field maxima. On the other hand, for negative magnetophoresis, the

magnetization of the particle or cell $\vec{M}_p$ is always less than its surrounding magnetic liquid $\vec{M}_f$, and the direction of the magnetic force $\vec{F}_m$ on the particle or cell is pointing towards field minima.

1.2.2 Hydrodynamic Viscous Drag Force

The Reynolds number in a typical microfluidic device is much less than 1, resulting in laminar flows. Hydrodynamic viscous drag force thus plays a significant role in particle and cell manipulation; its expression on a spherical particle is,

$$\vec{F}_h = -3\pi\eta D_p\left(\vec{U}_p - \vec{U}_f\right) f_D \tag{1.5}$$

Here, η is the viscosity of magnetic liquids, $\vec{U}_p$ and $\vec{U}_f$ are velocity vectors of magnetic liquids and particles, respectively, f_D is hydrodynamic drag force coefficient of a particle experiencing the effect of having a solid surface in its vicinity, which is often referred to as a "wall effect". The function f_D can be expressed in Equation (1.6) as a resistance function of the hydrodynamic interaction between the particle and the surface. Its appearance indicates the particle experiences increased fluid viscosity as it moves closer to the surface.[47-50]

$$f_D = \left[1 - \frac{9}{16}\left(\frac{D_p}{D_p + 2\Delta}\right) + \frac{1}{8}\left(\frac{D_p}{D_p + 2\Delta}\right)^3 - \frac{45}{256}\left(\frac{D_p}{D_p + 2\Delta}\right)^4 - \frac{1}{16}\left(\frac{D_p}{D_p + 2\Delta}\right)^5\right]^{-1} \tag{1.6}$$

Here, D is the shortest distance between the particle surface and solid surface.

In the case of ferrofluids as the surrounding medium, the magnetic nanoparticles tend to form a chain structure due to inter-particle interaction, leading to an increase of

the overall liquid viscosity. This phenomenon is known as the magnetoviscous effect.[51] However, such an effect becomes pronounced only in highly concentrated ferrofluids. The volume concentration of ferrofluids in particle and cell manipulation, however, is on the order of 1%, and therefore the magnetoviscous effect can be neglected for future analysis.

1.2.3 Gravitational and Buoyant Forces

The net force of gravitational and buoyant forces on a spherical body can be expressed as,

$$\vec{F}_n = \frac{\pi D_p^{\,3}}{6}\left(\rho_p - \rho_f\right)\vec{g} \tag{1.7}$$

Here, $\vec{g}$ is the direction of gravity, r_p and r_f are the densities of the particle or cell, and its surrounding magnetic liquids, respectively. Typically, particles and cells possess a density that is very close to that of magnetic liquids. As a result, the net force $\vec{F}_n$ is usually one order of magnitude lower than magnetic force $\vec{F}_m$ or hydrodynamic force $\vec{F}_h$. However, the subtle difference of this force between two species with very similar densities was recently exploited for high-resolution particle and cell separation in magnetic liquids.[52-56] We will review its working principle in Section 1.4.2.

Due to the low Reynolds number and resulting laminar flow in microfluidic systems, inertial effects can be neglected. Therefore, the dynamics of particles and cells in magnetic liquids are determined by the balance of all dominant forces,

$$\vec{F}_m + \vec{F}_h + \vec{F}_n = 0 \tag{1.8}$$

Equation (1.8) yields the relative velocity of a spherical body in magnetic liquids.

$$\vec{U}_p - \vec{U}_f = \frac{D_p^{\,2}}{18\eta}\left[\mu_0\left[\left(\vec{M}_p - \vec{M}_f\right)\cdot\nabla\right]\vec{H} + \left(\rho_p - \rho_f\right)\vec{g}\right] \quad (1.9)$$

It is clear from Equation (1.9) that the dynamics of a particle or a cell in magnetic liquids is determined by its physical properties, including size, density, as well as the contrast of magnetization between itself and the surrounding medium. These three physical properties are currently being exploited for microfluidic applications using magnetic liquids. We will discuss the origins of these manipulation specificities and their applications in Section 1.4.

1.3 Magnetic Liquids

1.3.1 Paramagnetic Salt Solutions

Representative applications of negative magnetophoresis in microfluidics include cell and particle manipulation in either a paramagnetic salt solution or a ferrofluid. Several types of paramagnetic salt solutions are available for this purpose. They are generally formed with a paramagnetic metal and an organic chelating agent or halide. Solutions containing certain transition and lanthanide metals, such as Mn^{2+} and Gd^{3+}, are paramagnetic due to their unpaired inner-shell electrons that can produce a magnetic moment. Chelating agents, such as diethylenetriaminepentaacetic acid (DTPA) and diethylenetriamine triacetic acid didecyldiacetamide (DTAD) can bind to these metal cations. Gd·DTPA is commonly used by Whitesides's and coworkers in experiments that involve proteins, since it is a cheap and a readily available paramagnetic solution used in magnetic resonance imaging (MRI), which does not denature proteins.[55, 57] Gadolinium-based contrast agents (GBCAs) were introduced in 1984 to perform MRI scans on patients using Gd(DTPA).[2, 58, 59] Gadolinium in all GBCAs is chelated to organic ligands to render the compound safe, as the free gadolinium ion is toxic to humans.[60] GBCAs are

widely viewed as being safe to administer to patients with almost no adverse health effects. GBCAs such as gadavist (gadobutrol) have been used more recently in density-based separation experiments as the paramagnetic medium of choice.[61, 62] When injected into human patients, most GBCAs are formulated in concentrations of 0.5-1 M, or administered at 0.1 mM kg^{-1}-0.3 mM kg^{-1} of body weight.[60] When used in density-based manipulation settings, it is used at concentrations between 25-250 mM.[61-63] Halide salts, such as $MnCl_2$ and $GdCl_3$ are more widely used in experiments when samples of interest do not dissolve in aqueous solutions.[54] They are also transparent so that particles or cells are visible in them. However, they have a relatively high vapor pressure, which makes storing the solutions difficult, since they slowly lose volume over time. The loss of solvent also changes the concentration of the salt solution and affects its magnetic properties. Recently developed paramagnetic ionic liquids (PILs) have a low vapor pressure and do not evaporate easily.[64] PILs are a subset of ionic liquids that contains cation-anion mixtures and melt at or below 100 ºC.[65] Typically, a combination of a sterically hindered organic cation and a metal-halide anion complex are used to create a PIL.[66] Some common metal-halide complexes include $[GdCl_6]^{3+}$, $[DyCl_6]^{3+}$, $[HoCl_6]^{3+}$, and $[MnCl_4]^{2+}$. As previously discussed, these metals are paramagnetic due to their unpaired inner-shell electrons, and as a result, the ionic liquid containing these metals is paramagnetic as well. For example, 1-butyl-3-methylimidazolium tetrachloroferrate ([BMIM][$FeCl_4$]) is a common PIL.[64, 67] PILs have increased shelf life due to their low vapor pressure, low melting points, high thermal stability, and tunable properties.[64]

Generally speaking, a paramagnetic salt solution has relatively low volume magnetic susceptibility and magnetization. For example, manganese (II) chloride

($MnCl_2$)'s solubility limit in water at room temperature is 1470 kg m^{-3},[68] corresponding to a molar concentration of 11.7 M. Its initial volume magnetic susceptibility is 9×10^{-4} at this solubility limit, while its magnetization is 1.4×10^{3} A m^{-1} and 1.4×10^{4} A m^{-1} at magnetic flux densities of 2 T and 20 T, respectively.[27] Commonly used concentrations of the paramagnetic salt solution in the published literature are in the range of 0.1-1 M, partly in order to achieve good biocompatibility for cell manipulation.[31, 40, 69-71] As a result, its typical susceptibility and magnetization are even lower than the above-mentioned values. Typical applications of a paramagnetic salt solution use either high magnetic fields generated from superconducting magnets[69, 71] or high field gradients from microfabricated ferromagnetic structures[41] to compensate for its low susceptibility and magnetization and achieved fast particle and cell manipulation.

1.3.2 Ferrofluids

Another type of magnetic liquid that has relatively high volume magnetic susceptibility and magnetization under fields generated by permanent magnets is ferrofluids. Ferrofluids are colloidal suspensions of magnetic nanoparticles, typically magnetite (Fe_3O_4) or maghemite (Fe_2O_3) with diameters of approximately 10 nm.[27] The nanoparticles are covered by either electrostatic or steric surfactants to keep them from aggregating and in suspension within a carrier medium. Ferrofluids can be prepared by simple chemical co-precipitation methods. Its synthesis usually involves co-precipitation of ferrous and ferric salts in an aqueous base solution, followed by an oxidation process.[27] Progress has also made towards developing biocompatible ferrofluids for MRI contrast agents.[72-76] For example, oleic acid-coated iron oxide nanoparticles dispersed in chitosan were synthesized for MRI contrast agent,[77] and starch polymer coated magnetic

nanoparticles were prepared for MRI tests in tumor targeting.[78, 79] Ferrofluid hydrodynamics (ferrohydrodynamics), dealing with mechanics of ferrofluid motion under external magnetic fields, has been well studied since 1960s.[27] The fundamentals and applications of ferrohydrodynamics are reviewed and summarized in several books.[27, 80, 81] In its applications to particle manipulation, an effective magnetic dipole moment within the diamagnetic object immersed in ferrofluids is induced. As a result, the object experiences a magnetic buoyancy force under a non-uniform magnetic field. This principle has been used to assemble particles.[43, 82-84]

The susceptibility and magnetization of a ferrofluid are tunable through controlling its concentration of magnetic materials. For example, the maximal volume fraction of a water-based magnetite ferrofluid is approximately 10%. Given the bulk magnetization of magnetite is 4.46×10^5 A m^{-1}, this ferrofluid's initial volume magnetic susceptibility is on the order of 1, and its saturation magnetization is on the order of 10^4 A m^{-1} under fields generated from a hand-held permanent magnet, both of which are significantly larger than the values of a paramagnetic salt solution. Better magnetic properties of the ferrofluid may enable its applications with the use of simple permanent magnets, instead of superconducting magnets or microfabricated ferromagnetic structures, for fast microfluidic manipulations.

Typical ferrofluids used in microfluidic applications are water-based. The issues of using water-based ferrofluids for particle or cell manipulation are two-fold. First, light diffraction from the high concentration of magnetic nanoparticles in ferrofluids makes it difficult to directly observe particles or cells. To solve this problem, microfluidic devices with shallow channels and ferrofluids with low solid volume fraction are needed. Second,

biocompatible ferrofluids are necessary for live cell manipulation. For mammalian cells, materials, pH value, and surfactants of ferrofluids need to be rendered biocompatible, while at the same time the overall colloidal system of ferrofluids must be maintained. To satisfy these criteria, the materials of nanoparticles within ferrofluids need to be biocompatible, such as magnetite or maghemite. The pH value of ferrofluids needs to be compatible with cell culture and maintained around 7. Salt concentration, tonicity, and surfactant must be carefully chosen close to physiological conditions to reduce cell death. Progress has been made towards synthesizing biocompatible ferrofluids, which will be reviewed in Section Biocompatibility of Ferrofluids.

1.4 Review of Applications

1.4.1 Size-Based Manipulation

Size difference among particles or cells is the most frequently used manipulation specificity in magnetic liquids. Equation (1.9) indicates that particles or cells with larger size (volume) move faster in magnetic liquids than smaller ones, provided that they share the same magnetic properties, and their velocities are perpendicular to the direction of gravity. Larger particles or cells move faster because larger particles or cells experience much more magnetic forces than smaller ones, as the magnetic forces are proportional to the volume, while the hydrodynamic viscous drag force, on the other hand, scales only with the diameter. This is the working principle for size-based manipulation in magnetic liquids. A schematic of continuous-flow size-based manipulation in magnetic liquids is also shown in Figure 1.2a. Cells mixed with magnetic liquids are introduced into a microfluidic channel and hydrodynamically focused by a sheath flow. Once entering the separation region, deflection of cells from their flow paths occurs because of the

magnetic forces on them under a non-uniform magnetic field. At the end of the channel, larger cells are deflected into a different outlet than smaller ones, as shown in Figure 1.2a. Through different magnetic field patterns, size-based manipulation was also applied to particle and cell trapping (Figure 1.2b) and focusing (Figure 1.2c). We now review its existing microfluidic applications using either paramagnetic salt solutions or ferrofluids.

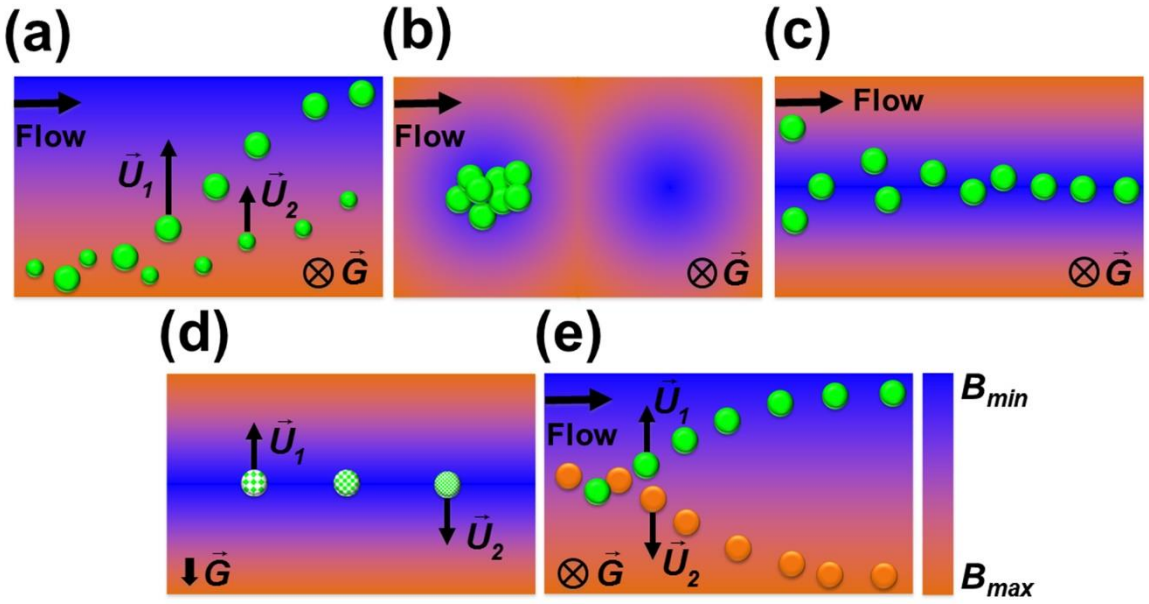

Figure 1.2: Schematic working principles of (a) size-based manipulation, (b) particle/cell trapping, (c) particle/cell focusing, and (d) density-based manipulation in magnetic liquids. The particle on the right is denser than the one on the left, while the middle particle has the same density as its surrounding medium. (e) Magnetization contrast-based manipulation. The orange particle is more magnetic than the medium, while the green particle is less magnetic than the medium. $\vec{U}_1$ and $\vec{U}_2$ represent the direction and the magnitude of the particle's or cell's velocity. Arrow and cross indicate the direction of gravity $\vec{G}$. The color map depicts distributions of magnetic field strength, from maxima B_{max} (orange) to minima B_{min} (blue).

Paramagnetic Salt Solution-Based Manipulation

Separation: Size differences between particles or cells are often used for separation in paramagnetic salt solutions. Their working mechanisms and performances

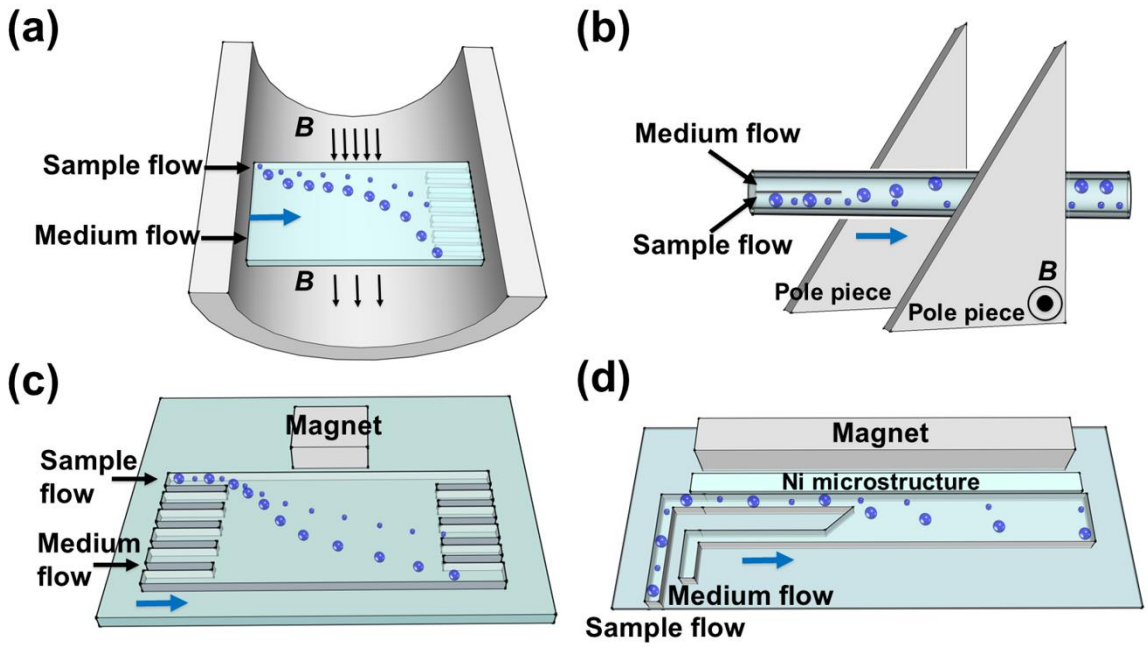

Figure 1.3: Schematic representations of size-based separation in paramagnetic salt solutions. (a) A continuous separation of diamagnetic particles in $MnCl_2$ solution in a superconducting magnet. Reproduced from ref.[69] (b) Separation of particles in $MnCl_2$ solution using triangular shaped pole pieces in a capillary. Reproduced from ref.[85] (c) Deflection of diamagnetic particles by a permanent magnet in a microfluidic system. Reproduced from ref.[40] (d) Microfluidic separation of diamagnetic particles/cells with a microfabricated nickel microstructures. Reproduced from ref.[41] Blue arrow in each figure indicates the flow direction.

are summarized in Figure 1.3 and Table 1.1. Tarn et al.[69] applied diamagnetophoresis for a continuous separation of diamagnetic particles in $MnCl_2$ solution (0.48 and 0.79 M), as shown in Figure 1.3a. They examined the separation of 5 μm and 10 μm diameter particles in different concentrations of this salt solution and concluded that better separation performance could be achieved with a higher concentration of $MnCl_2$ solution in a superconducting magnet with an external magnetic flux of 10 T. Kawano et al.[85] developed a two-dimensional capillary cell to separate particles in $MnCl_2$ solution (1 M) using triangular shaped pole pieces, as shown in Figure 1.3b. Fractionation of particles with different diameters (1, 3, and 6 μm) was achieved in a superconducting magnet.

Table 1.1: Summary of sized-based manipulation in paramagnetic salt solutions.

Magnetic liquids	Magnetic fields	Applications	Efficiency	Throughput	References
$MnCl_2$	Superconducting magnet	Particle separation	NA	~10^5 particles h^{-1}	69
$MnCl_2$	Superconducting magnet	Particle separation	100%	~10^5 particles h^{-1}	71
$MnCl_2$	Superconducting magnet	Particle/cell separation	NA	NA	85
$MnCl_2$	Permanent magnet	Particle trapping	NA	NA	86
$MnCl_2$	Permanent magnet	Particle trapping	0-100%	NA	87
$MnCl_2$	Permanent magnet and iron pieces	Particle/cell trapping	0-100%	NA	88
$MnCl_2$	Permanent magnet	Particle trapping	100%	~10^4 particles h^{-1}	70
$MnCl_2$	Permanent magnet	Particle trapping/ Particle focusing/ Particle separation	100% NA 100%	~10^3 particles h^{-1}/ ~10^4 particles h^{-1}/ ~10^4 particles h^{-1}	40
$MnCl_2$	Permanent magnet	Particle transport	NA	~10^5 particles h^{-1}	89
Gd·DTPA	Permanent magnet	Cell focusing	40%	NA	31
Gd·DTPA	Permanent magnet and Ni microstructure	Cell separation	90% purity	10^5 cells h^{-1}	41
Gd·DTPA	Permanent magnet	Particle/cell trapping	NA	NA	45

They also fractionated deoxygenated and non-deoxygenated red blood cells using a wider capillary cell. They showed that deoxygenated red blood cells had a large variation of the magnetic susceptibility. Vojtíšek et al.[71] developed two microfluidic devices, which were inserted into the bores of superconducting magnets, to separate particles of different sizes (5.33 and 10.32 μm). They concluded that diamagnetic repulsion of particles could be enhanced by increasing particle size, the concentration of paramagnetic salt solution, and magnetic field strength and gradient. They further demonstrated deflection of microbubbles suspended in $MnCl_2$ (0.48 M). Peyman et al.[40] developed a versatile microfluidic device (see Figure 1.3c) for particle separation in a $MnCl_2$ solution (0.79 M). The device was used to separate 5 μm and 10 μm particles. Shen et al.[41] developed a microfluidic system with microfabricated nickel microstructures embedded in a

microchannel, as shown in Figure 1.3d. The system generated sufficient magnetic repulsion forces for the separation of cells and particles with different sizes. They demonstrated the separation of U937 cells (human histolytic lymphoma monocytes) from red blood cells (RBCs) with over 90% purity and moderate throughput of 1×10^5 cells h^{-1} in a Gd·DTPA solution.

Focusing: Focusing particles and cells[90-92] into a narrow stream in a continuous-flow manner is critical for downstream analytical procedures in microfluidic systems. In order to achieve focusing in magnetic liquids, a local magnetic field minimum needs to be created in the microfluidic device, typically via a pair of opposing magnets. Diamagnetic particles and cells suspended in magnetic liquids, experiencing magnetic buoyancy force as they flow through the channel, can then be focused into narrower streams for further processing. Working mechanisms and performances of existing focusing schemes using paramagnetic salt solutions are summarized in Figure 1.4 and Table 1.1. Peyman et al.[40] developed a system with a capillary and a pair of magnets to focus continuously diamagnetic particles (10 μm) into a narrow stream, as shown in Figure 1.4a. They demonstrated that the diamagnetic forces were capable of focusing particles to the center of a fused silica capillary at a flow rate of 40 μL h^{-1}. Rodríguez-Villarreal et al.[31] developed a diamagnetic repulsion setup to focus particles (10 and 20 μm) and HaCaT cells (spontaneously immortalized human skin keratinocyte) in a continuous-flow fashion. They optimized focusing parameters including magnetic susceptibility of the medium, flow rate, particle size, and exposure time of particles in the magnetic field. They demonstrated that 40% of HaCaT cells could then be focused in paramagnetic media (39 mM Gd·DTPA) in their setup. Zhu et al.[89] studied the transport

of diamagnetic particles (5, 10, 15 μm) in a $MnCl_2$ solution (0.04, 0.2, 1 M). They looked into the effects of particle position, size, flow rate and concentration of salt solution on particle deflection.

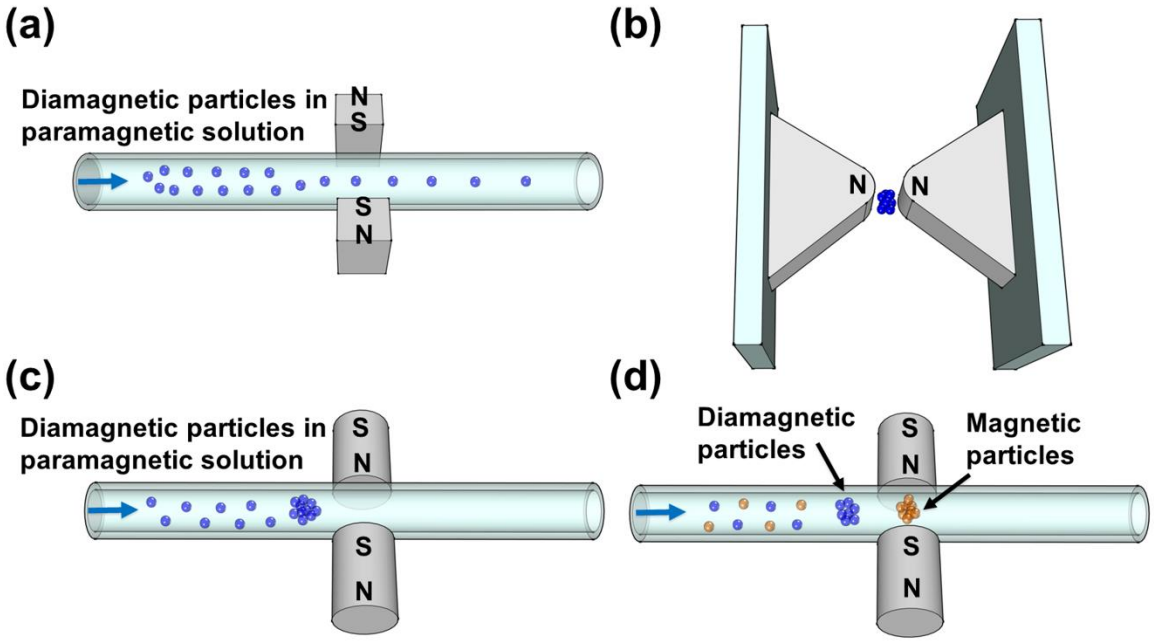

Figure 1.4: Schematic representations of size-based focusing and trapping in paramagnetic salt solutions. (a) Focusing of diamagnetic particles in a capillary with a pair of magnets. Reproduced from ref.[40] (b) Trapping of diamagnetic particles and living cells using a three-dimensional magnetic trap. Reproduced from ref.[45] (c) Trapping of diamagnetic polymer particles in a capillary. Reproduced from ref.[40] (d) Simultaneous trapping of diamagnetic and magnetic particles in a capillary. Reproduced from ref.[70] Blue arrows in figures indicate the flow direction.

Trapping and concentration: Trapping and concentrating particles or cells are conceptually similar to focusing, except in this case, the flow in microfluidic devices is static or very small so that the magnetic buoyancy force is able to retain particles or cells at the locations of magnetic field minima. Its working mechanisms and performance are summarized in Figure 1.4 and Table 1.1. Watarai et al.[86] studied the magnetophoretic

migration behavior of diamagnetic particles in a paramagnetic salt solution (0.6 M $MnCl_2$). Migration velocity and direction of various diamagnetic particles (1.5, 3, 6, and 9 μm) were investigated in a sealed capillary tube sandwiched by two permanent magnets. They concluded that particle migration was affected by magnetic buoyancy force. A device was then developed to achieve the trapping of diamagnetic polystyrene particles with different sizes (2.77, 5.87, 9.14 μm).[87] Later on, Watarai et al.[88] developed a square fused-silica capillary magnetophoretic device to trap RBCs in $MnCl_2$ solution (0.1 M). Winkleman et al.[45] demonstrated the trapping of diamagnetic particles and different types of living cells in a paramagnetic salt solution using a three-dimensional magnetic trap, as shown in Figure 1.4b. They also examined the biocompatibility of the gadolinium solution. They also showed that Gd·DTPA possessed minimal detrimental effect on the viability of both fibroblast cells (NIH 3T3) and yeast cells (*Saccharomyces cerevisiae*) at a concentration of 40 mM. Peyman et al.[40] developed a device to trap particles (10 μm) in a paramagnetic salt solution (0.79 M $MnCl_2$). Figure 1.4c shows two pairs of permanent magnets with opposite poles facing each other, which were used to generate a magnetic gradient to trap streptavidin coated diamagnetic particles in a capillary. Tarn et al.[70] developed a simple concentration method that could achieve simultaneous trapping of diamagnetic and magnetic microparticles with a 100% efficiency in a capillary with a pair of magnets, as shown in Figure 1.4d. After trapping, biochemical assays were examined on the particles to achieve multiple analyses.

Ferrofluid-Based Manipulation

Separation: Ferrofluids, which have a relatively high volume magnetic susceptibility and magnetization under fields generated by permanent magnets, are

frequently used as the carrier medium to separate particles and cells with different sizes. Their working mechanisms and performance are summarized in Figure 1.5 and Table 1.2. Zhu et al.[42] developed a label-free separation scheme using a commercial ferrofluid (EMG 408 from Ferrotec Corp., Santa Clara, CA, USA) to separate continuously binary mixtures of diamagnetic particles (1 and 9.9, 1.9 and 9.9, 3.1 and 9.9 μm) in a microfluidic device, as shown in Figure 1.5a. The magnetic field gradient created by permanent magnets in the microchannel made it low-cost and efficient to conduct size-based separation with a throughput of 10^5 particles h^{-1} and close to 100% separation efficiency. Later on, Zhu et al.[44] ferrohydrodynamically separated *Escherichia coli* from *Saccharomyces cerevisiae* cells using the same commercial ferrofluid with high throughput (~10^7 cells h^{-1}) and efficiency (~100%) in a continuous-flow manner. They

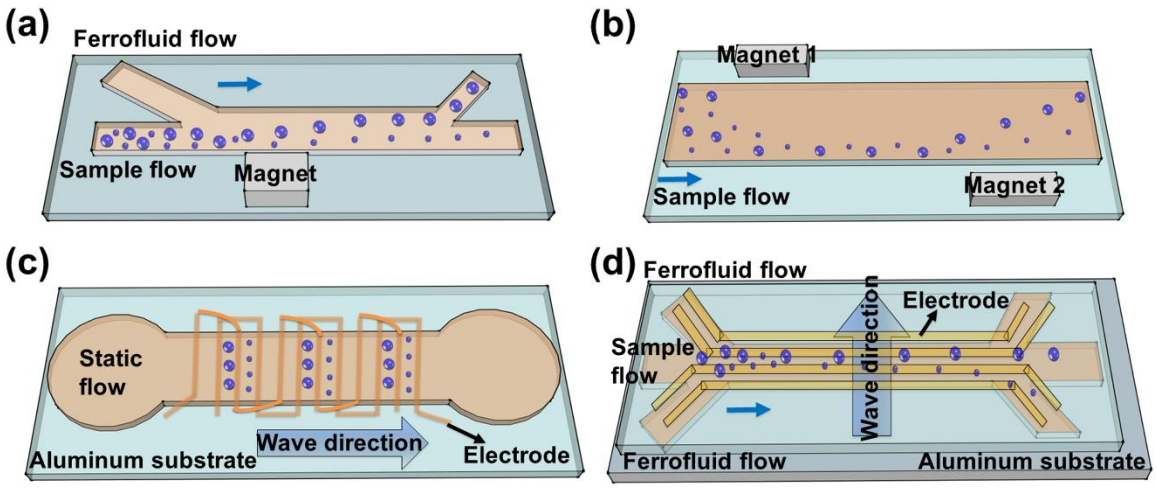

Figure 1.5: Schematic representations of size-based separation in ferrofluids. (a) Continuous separation of binary mixtures of diamagnetic particles in a microfluidic device. Reproduced from ref.[42] (b) Separation of particles and live yeast cells in a ferrofluid using two offset permanent magnets. Reproduced from ref.[93] (c) Separation of bacteria and blood cells in a biocompatible ferrofluid using traveling-wave magnetic fields. Reproduced from ref.[38] (e) Nanocytometry particle sorting device. Reproduced from ref.[94] Blue arrows in figures indicate the flow direction.

used a three-dimensional analytical model to predict cells' trajectories. The simulated cell dynamics agreed well with the experimental results. Furthermore, they showed this particular commercial ferrofluid was not detrimental to the viability of both cell types after 2 h of exposure. Recently, Zhao and Zhu et al.[95] demonstrated the separation of HeLa cells (cervical carcinoma) and blood cells in a custom-made biocompatible ferrofluid with a moderate throughput (~10^6 cells h^{-1}) and high separation efficiency (> 99%). Liang et al.[96] separated binary mixture of particles (5 and 15 μm) in EMG 408 ferrofluids. Zeng et al.[93] achieved the separation of particles and live yeast cells in EMG 408 ferrofluids using two offset permanent magnets, as shown in Figure 1.5b. One of the magnets was used to focus particle mixtures into a narrow stream, and the other was used to separate them. They examined the effects of flow rate and magnet-microchannel distance on the particle separation. The separation distance between two particle streams could be increased by decreasing the flow speed or magnet-microchannel distance. They also demonstrated the separation of live yeast cells from particles.

Separation of particles and cells in ferrofluids were also achieved using traveling-wave magnetic fields generated from microfabricated electrodes. Kose et al.[38] used a traveling-wave magnetic field for particle and cell separation, as shown in Figure 1.5c. In their setup, the spatially-traveling and timely-alternating magnetic field was generated by microfabricated electrodes embedded at the bottom of a microchannel. The electrodes were made using a single layer of copper on a printed circuit board. They were then wire bonded in a pattern that resulted in a 90-degree current phase difference between each adjacent electrode. The resulting fundamental component of the magnetic field in the channel is a travelling wave, similar to the travelling excitation over the stator surface in

Table 1.2: Summary of sized-based manipulation in ferrofluids.

Magnetic liquids	Initial magnetic susceptibilities	Saturation magnetizations [mT]	Magnetic fields	Applications	Efficiency	Throughput	References
[1]EMG 408 ferrofluid	0.5	6.6	Permanent magnet	Particle separation	100%	~10^5 particles h^{-1}	42
[1]EMG 408 ferrofluid	0.5	6.6	Permanent magnet	Particle/cell separation	100%	~10^7 particles h^{-1}	44
[1]EMG 408 ferrofluid	0.5	6.6	Permanent magnet	Particle separation	NA	NA	96
[1]EMG 408 ferrofluid	0.5	6.6	Permanent magnet	Particle/cell separation	NA	NA	93
[1]EMG 408 ferrofluid	0.5	6.6	Permanent magnet	Particle focusing	NA	NA	97-99
[1]EMG 408 ferrofluid	0.5	6.6	Permanent magnet	Particle/cell concentration	NA	NA	100
[1]EMG 408 ferrofluid	0.5	6.6	Permanent magnet	Particle concentration	NA	~10^5 particles h^{-1}	101
[1]EMG 408 ferrofluid	0.5	6.6	Permanent magnet	Particle trapping	NA	~10^5 particles h^{-1}	102
[1]EMG 408 ferrofluid	0.5	6.6	Permanent magnet	Particle/cell focusing	NA	~10^5 cells h^{-1}	103
[1]EMG 408 ferrofluid	0.5	6.6	Permanent magnet	Particle transport	NA	NA	46
[1]EMG 705 ferrofluid	4.04	22	Permanent magnet	Droplet fabrication and manipulation	NA	NA	104
[1]EMG 700 ferrofluid	12.57	32.5	Traveling-wave magnetic fields from copper electrodes	Particle separation	99%	3×10^4 particles s^{-1} mm^{-2}	94
[2]Citrate stabilized ferrofluid	NA	NA	Traveling-wave magnetic fields from microfabricated electrodes	Cell separation	75.2%	NA (static flow system)	38
[2]Graft copolymer functionalized ferrofluid	NA	NA	Permanent magnet	Cell separation	>99%	~10^6 cells h^{-1}	95
[3]MF01 ferrofluid	0.2	50	Permanent magnet	Droplet manipulation	NA	NA	105, 106

[1]Commercially available from Ferrotec Corp., [2]custom-made ferrofluids, and [3]commercially available from Sunrise Ferrofluid Technological Ltd.

an electric motor. In their microfluidic system, the flow is static, and the direction of the traveling-wave was parallel to the moving directions of particles and cells. Depending on their size, the particles or cells were either trapped or moving continuously, resulting in a spatial separation in the channel. They demonstrated the separation of bacterial and blood cells with a 95.7% efficiency, and separation of healthy red blood cells from sickle cells, with an efficiency of 75.2% in a citrate stabilized biocompatible ferrofluid. A similar principle was also applied in a microfluidic device called a nanocytometer that could separate binary (2.2 and 4.8 μm) and ternary (2.2, 4.8, 9.9 μm) mixtures of diamagnetic particles in a commercial EMG 700 ferrofluids by Kose et al.[94], as shown in Figure 1.5d. In this case, the direction of the traveling-wave was perpendicular to the moving particle. As a result, the particles could be separated in a continuous flow with higher throughput.

Focusing: Zhu et al.[97] developed a microfluidic particle focusing scheme within EMG 408 ferrofluids. Focusing of particles with different sizes (4.8, 5.8, 7.3 μm) at various flow rates was demonstrated, as shown in Figure 1.6a. An analytical model was developed in this study to simulate the distribution of a magnetic field, magnetic force and trajectories of particles within the device. A three-dimensional diamagnetic microparticle focusing scheme in EMG 408 ferrofluids was presented by Liang et al.[98] Particles were magnetically deflected both in a horizontal and vertical direction through the cross-section of the channel to form a focused stream. Ferrofluid concentration, particle size, and flow rate were demonstrated to have significant effects on particle deflection. They developed a numerical model to predict microparticle deflection in ferrofluid flows, too. Zeng et al.[103] conducted a theoretical and experimental study on the focusing of diamagnetic particles with diameters of 5 μm and yeast cells in EMG 408

ferrofluids. Two sets of opposing permanent magnets were embedded into the microchannel to achieve diamagnetic focusing. The effectiveness of focusing was studied at different flow rates and different particle sizes. Furthermore, cell viability results demonstrated that this focusing method in ferrofluid was biocompatible with yeast cells. A simpler setup with only one magnet was used by Liang et al.[99] to focus particles, as shown in Figure 1.6b.

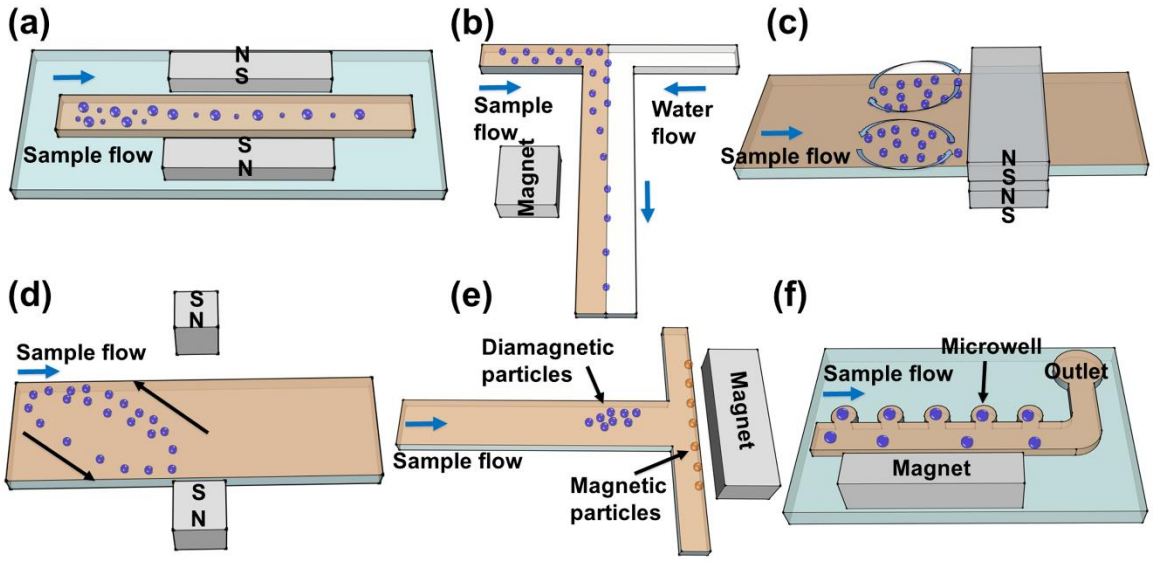

Figure 1.6: Schematic representations of size-based manipulation (focusing, trapping, concentration, droplet manipulation) in ferrofluids. (a) Microfluidic particle focusing in ferrofluids. Reproduced from ref.[97] (b) Focusing particles in a ferrofluid flow using a single permanent magnet. Reproduced from ref.[99] (c) Magnetic concentration of particles and cells using attracting magnets. Reproduced from ref.[100] (d) Diamagnetic particle concentration in ferrofluids with an asymmetric magnet configuration. Reproduced from ref.[101] (e) Simultaneous trapping and pre-concentrating of diamagnetic and magnetic particles in ferrofluids in a T-junction channel. Reproduced from ref.[102] (f) Manipulation of aqueous droplets in ferrofluids. Reproduced from ref.[105, 106] Blue arrow in each figure indicates the flow direction.

Trapping and concentration: Zeng et al.[100] presented a simple device configuration that was used for magnetic concentration of particles and live yeast cells in

EMG 408 ferrofluids flow using attracting magnets, as shown in Figure 1.6c. The magnet-magnet distance and flow rate effects on the concentration of particles were studied. The biocompatibility of this ferrofluid was also tested, indicating that it had minimum effects on the viability of yeast cells. Wilbanks et al.[101] investigated the concentration of diamagnetic particles in EMG 408 ferrofluid using an asymmetric magnet configuration, as shown in Figure 1.6d. With such a configuration, they achieved a stronger magnetic force and thus higher ferrofluid flow rate for continuous particle trapping. Zhou et al.[102] used a single permanent magnet and a T-junction microchannel to trap simultaneously and pre-concentrate diamagnetic and magnetic particles in EMG 408 ferrofluids, as shown in Figure 1.6e. Diamagnetic particles experienced negative magnetophoresis and were trapped in the main channel (T-junction region). At the same time, magnetic particles experienced positive magnetophoresis and were concentrated in the branched channel next to the magnet.

Droplet manipulation: In addition to particles and cells, droplets were also manipulated in non-mixable ferrofluids. Zhang et al.[105, 106] combined magnetic force and flow shear force to manipulate aqueous droplets-based on their sizes within a commercial engine oil-based ferrofluid in a microfluidic device, as depicted in Figure 1.6f. These droplets could be deflected, split, trapped, released, fused and exchanged for medium to achieve comprehensive manipulation. Recently, Zhu et al.[104] developed a magnetic-field-assisted method to generate and polymerize nonspherical particles in a microfluidic device. Monomer continuous flow phase formed droplets within an aqueous dispersed ferrofluid phase; they were then stretched or compressed into non-spherical shapes by magnetic fields.

Modeling efforts: Modeling is important for device design and optimization using negative magnetophoresis principle. Two types of models exist, including analytical models and numerical models. Analytical models were first developed by Furlani's group to enable accurate and fast parametric analysis of large-scale magnetophoretic systems.[107-109] Recently, Zhu et al.[46] developed a two-dimensional analytical model of microfluidic transport of diamagnetic particles and cells in ferrofluids. This model took into account important design parameters including particle size, the property of ferrofluids, magnetic field distribution, the dimension of the microchannel, and fluid flow rate. The simplicity and versatility of this analytical model made it useful for quick optimizations of future size-based separation devices. They also validated the model using a microfluidic device. Later on, a three-dimensional analytical model was developed by Cheng et al.[110] to provide a more precise estimate of dynamics of diamagnetic particles in magnetic liquids. In this model, the effects of magnetic field and force in the direction perpendicular to the moving particle, and channel depth were taken into consideration. As a result, the model could predict three-dimensional magnetic field and force, hydrodynamic drag force, flow profiles, particle deflection, particle residual time and particle velocity in simple microfluidic systems. Han et al.[111] developed a three-dimensional numerical model for the transport of diamagnetic particles in magnetic liquids. Although the numerical model required a higher demand for computing power and time, it could be applied to a broader range of microfluidic systems with complex configurations of channels and magnets.

1.4.2 Density-Based Manipulation

Paramagnetic salt solutions were often used in separating objects with different densities in static-flow systems. This type of separation is typically referred to as magnetic levitation, or "MagLev".[57, 112, 113] Negative magnetophoresis is the driving force behind magnetic levitation. Objects placed in a paramagnetic salt solution between two opposing magnets tend to migrate towards and stay at the location of magnetic field minima, which are on the centerline between the two magnets, as shown in Figure 1.2d. Depending on their relative density to surrounding medium, objects will then relocate along the direction of gravity. Based on Equation (1.9), if the objects are denser than the medium ($r_p > r_f$), a relative velocity of objects to medium ($\vec{U}_p - \vec{U}_f$) is induced so that the objects will migrate and reach an equilibrium height that is below the centerline between magnets. If the objects are less dense than the medium ($r_p < r_f$), the objects will float to a location that is above the centerline between the magnets. If the objects have exactly the same density as the medium ($r_p = r_f$), they will rest on the centerline between magnets.

Density-based manipulation was first utilized in the 1960s as a way to separate minerals, metals, and plastics from one another when placed in a ferrofluid or a paramagnetic salt solution.[54] This technology was later expanded in the 1990s to levitate various objects through the works of Beaugnon and Tournier,[114, 115] Weilert et al.,[116] and others.[117, 118] These experiments often relied on large non-uniform magnetic fields to levitate liquids, solids, and biological specimens. Using the same principles, several components in magnetic liquids can be separated from one another. Separation occurs when diamagnetic objects placed in a magnetic liquid have different buoyancy forces

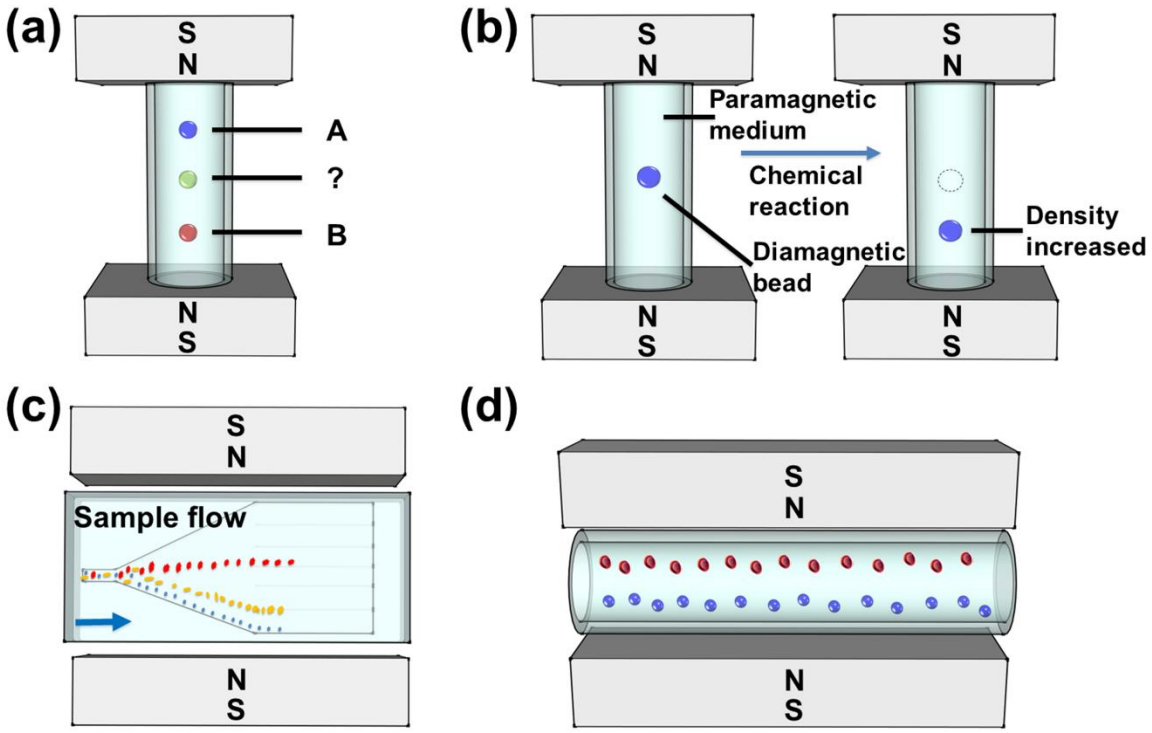

Figure 1.7: Schematic representations of density-based manipulation. (a) Magnetic levitation platform ("MagLev") for measuring densities. Reproduced from ref.[54] (b) Magnetic levitation device used for monitoring solid-supported reactions. Reproduced from ref.[53] (c) Microfluidic separation of particles with different densities. Blue arrow indicates the flow direction. Reproduced from ref.[52] (d) Magnetic levitation-based device ("MagDense") for determination of cell densities. Reproduced from ref.[56]

acting on them, due to the difference in their densities. On the other hand, magnetic forces acting upon these objects only depend on their size, magnetic field, and the contrast of susceptibilities between the objects and the paramagnetic carrier. If the size and susceptibility of these objects are kept the same, diamagnetic objects of different densities in the same magnetic liquid can be separated purely based on their density differences as shown in Figure 1.7a.[54]

Density-based manipulation has generated a wide range of applications recently. It was used for education and teaching reaction kinetics,[112] determination of differences

among chemical derivatives,[53] protein analysis,[55, 57, 119], food analysis.[113] flow-based separation in microfluidic devices,[52] and density determination of cells.[56, 61] The most popular setup of density-based separation is to create a custom fitting device that will hold strong permanent magnets in place, while a vial is placed in between them. The vial in between the magnets is filled with a paramagnetic medium so that any diamagnetic object placed in the vial will experience negative magnetophoresis. The applications of density-based manipulation were summarized in Table 1.3.

Non-Microfluidic Manipulation

Historically, many magnetic levitation experiments were performed by creating a non-uniform magnetic field. Beaugnon and Tournier demonstrated that any diamagnetic organic material could be levitated through such a method. They achieved such a field by using superconducting solenoids which could create a field gradient as high as 2000 T^2 m^{-1}.[115] Weilert et al.[116] levitated liquid drops of helium in a similar manner using solenoids. Their experiments demonstrated that drops helium were able to remain in contact with one another without coalescing. They later attested this phenomenon to the slow evaporation of the helium forming a layer of vapor between the two drops, thus producing a layer similar to that in the Leidenfrost effect.[120] Most famously, Berry and Geim used the same solenoid-based magnetic levitation to levitate a frog.[121] These experiments demonstrated how a diamagnetic object could be levitated and reach a stable equilibrium. Nowadays, magnetic levitation can be performed without superconducting solenoids and requires only a small and inexpensive set of equipment.

Many modern density-based manipulation methods follow the previously described setup, in which a vial is placed in between a custom fitting device with

Table 1.3: Summary of density-based manipulation.

Magnetic liquids	Applications	Flow-based	Analytes	Performance	References
[1]$MnCl_2$ $GdCl_3$	Density measurements	No	Foods and liquids	Density accuracy of ±0.0002 to ±0.02 g mL^{-1}	54
[1]$GdCl_3$	Teaching reaction Kinetics	No	Leucine on solid supports and amine derivatives	Experiment Performed in Approximately 1 h	112
[1]$GdCl_3$	Compound identification and reaction monitoring	No	Amine derivatives on polystyrene supports	Derivative identified in 15 min	53
[1]$MnCl_2$ $GdCl_3$ Gd·DTAD	Density measurements and food identification	No	Foods and liquids	1 pL to 1 mL sample volumes	113
[1]Gd·DTPA	Protein analysis	No	BCA on PEGA supports	Real time protein quantification in several hours	55
[1]Gd·DTPA	Protein analysis	No	BCA/sulfonamide on PEGA supports	Determination of protein diffusion coefficients	57
[1]Gd·DTPA	Fabrication of living material	No	Hydrogel and cell seeded microbeads	Contactless spatial arrangement of living material	122
[2]$MnCl_2$ $MnSO_4$	Protein analysis and immunoassays	No	Biotin and streptavidin on polystyrene supports	Improved real time protein quantification within 1 h	119
[2]Na_2S_2O	Cell monitoring	No	RBCs, WBCs, and PMNs	Real time morphological and spatial monitoring of cells	56
[2]Gd solution (gadavist)	Cell density measurements	No	RBCs, WBCs, and various cancer cell lines	Density resolution of ±0.0001 g mL^{-1}	61
[2]Gd solution (gadavist)	Microsphere density measurements	No	Polystyrene supports	Digital density measurements in under 6 min	62
[2]$GdCl_3$ Gd·DTPA	Flow-based density separation	Yes	Microsphere supports	0.10 to 0.25 µL min^{-1} flow rates	52
[2]Gd solution (gadavist)	Sickle cell anemia detection	No	RBCs	Results in 10 min	123
[2]Gd solution (gadavist)	Blood count test	No	RBCs and WBCs	Blood counts within 15 min	63

[1]Non-microfluidic manipulation and [2]microfluidic manipulation.

permanent magnets – a non-flow based method. This is often referred to as magnetic levitation, or "MagLev". Many fundamental aspects of magnetic levitation were explored by Mirica et al.[54] One important characteristic of MagLev is the dependency on size for the time of separation. Larger objects reach an equilibrium height faster than smaller objects. Mirica et al.[53] showed an application of measuring density over time with MagLev in Figure 1.7b. Microsphere solid support resins containing small molecules were placed into a 650 mM $GdCl_3$ solution. The small molecule would react with different amine derivatives, affecting the density of microspheres and their eventual height. Monitoring this change in density over time allowed for an easy way to monitor reaction progress and to discern compounds. Shortly after, the same group[113] developed a new application for MagLev involving food analysis. They demonstrated that foods with a higher fat content levitated higher than those with a lower fat content. Benz et al.[112] have used MagLev to aid in teaching reaction kinetics at the undergraduate level. In a simple MagLev experiment, they reacted leucine covered solid support resins with various amine derivatives in 590 mM $GdCl_3$. Overtime a denser product formed on the solid support, and by monitoring the levitation height over time, the reaction progress could be observed.

Another common application of non-flow MagLev is protein analysis. Because many biochemical studies rely on solid-supported chemistry,[53] MagLev proves to be a useful tool for analyzing proteins using microspheres. Shapiro et al.[55, 57] used density-based separation to quantify the amount of proteins in solution and to determine binding affinities of a protein to different small molecule targets. Tasoglu et al.[122] demonstrated the use of magnetic levitation to create small soft living material. Hydrogels and cell

seeded microbeads placed in 10, 50, or 100 mM Gd^{3+} solution would tend towards magnetic minima, and as such could be directed to construct the desired structure. By utilizing the magnetic field created by cheap NdFeB magnets, these living building blocks can be arranged in almost any desired spatial arrangement without the need for electricity or physical contact.

Microfluidic Manipulation

Microfluidic manipulation follows the same principle as non-microfluidic manipulation in that a container is placed in a custom fitting device with permanent magnets; however, microfluidic manipulation works with a much smaller container and often deals with smaller samples, such as single cells. Winkleman et al.[52] developed a flow-based microfluidic device capable of separating particles of various densities, as shown in Figure 1.7c. Using this device, they were able to separate particles with different densities. Depending on the flow rate, separation time could occur between a few min and an h. Using a non-flow method, Subramaniam et al. [119] utilized MagLev to quantify the amount of protein in solution and to perform immunoassays. They used a density amplified MagLev process that could determine the presence of neomycin in milk and the presence of several viral antibodies in vitro.

Cellular properties and cellular morphological changes can be analyzed using microfluidic-based density separation. Tasoglu et al.[56] used magnetic levitation as a method to differentiate cell types from each another and to monitor cell responses to stimuli, based on eventual equilibrium heights, as shown in Figure 1.7d. Healthy and sickle RBCs were placed into 10 mM sodium metabisulfite ($Na_2S_2O_5$) and their equilibrium heights were compared to each another. Sickle RBCs reached a final

equilibrium height that was easily distinguishable from healthy RBCs, giving an effective method to determine normal cells from sickle cells. Polymorphonuclear leukocytes (PMNs) were placed into 30 mM Gd^{3+} and activated with phorbol 12-myristate 13-acetate (PMA). Activated PMNs would reach a different equilibrium height from resting PMNs, allowing for morphological monitoring to be achieved. Cellular densities were determined by Durmus et al.[61] by placing several different mammalian cells into fetal bovine serum (FBS) with 30 mM Gd^{3+}. Each cell density was determined in a solution consisting of a single cell type. Average measured densities of 1.109 and 1.088 g mL^{-1} were found for RBCs and white blood cells (WBCs), respectively. It was also determined that this setup for cellular separation, called "MagDense," was able to determine the density of colorectal cancer cells to be 1.063 ± 0.007 g mL^{-1} and 1.084 ± 0.012 g mL^{-1}, for HCT116 (colorectal carcinoma) and HT29 (colorectal adenocarcinoma) cell lines, respectively. The authors concluded that MagDense was a possible method to discern circulating tumor cells from whole blood due to these density discrepancies because MagDense had a resolution range of 1×10^{-4} g ml^{-1} to 5.5×10^{-4} g mL^{-1}.

More recently, Knowlton et al.[62] developed a novel setup for magnetic levitation, which consisted of a smartphone, 3D-printed lens, small capillary tube, and permanent magnets. The setup used a custom smart-phone application on an Android operating system to detect different equilibrium heights of particles and estimate their densities. They found that this apparatus was able to work accurately in a density range of 0.96-1.09 g mL^{-1}, using various concentrations of gadolinium solution between 25 and 200 mM, with equilibration times of 6 min or shorter. Using a similar smartphone platform called Sickle Cell Tester, Knowlton et al.[123] tested RBCs for sickle cell anemia. In this

study, they used the same gadolinium solution varying at concentrations between 25 and 200 mM. After exposing healthy control RBCs and diseased RBCs to sodium metabisulfite, the diseased RBCs gained a noticeable amount of density due to experiencing more dehydration and deoxygenation compared to healthy RBCs. This density discrepancy, in turn, was recognized by the Sickle Cell Tester, which allows for a diagnosis to be made. Baday et al.[63] also used smartphone imaging with magnetic levitation (i-LEV) to perform blood count tests. RBCs and WBCs in a finger prick aliquot of blood placed in a microcapillary with 30 mM of gadolinium solution were separated using permanent NdFeB magnets. After 15 min of equilibration time, the custom smartphone software could analyze the width of the blood band which resulted from the separated RBCs and WBCs to perform blood counts.

1.4.3 Magnetization Contrast-Based Manipulation

Equation (1.9) also shows that the contrast of magnetization between particle/cell and its surrounding magnetic liquid plays an important role in their dynamics. As the contrast increases, the magnitude of velocity goes up. This enables exploiting magnetization contrast between fluids and particles/cells as a manipulation specificity in two different ways. For example, if there exist two types of particles/cells with magnetizations of $\vec{M}_{p1}$ and $\vec{M}_{p2}$ in a magnetic liquid with magnetization of $\vec{M}_f$, and if $\vec{M}_f$ is between $\vec{M}_{p1}$ and $\vec{M}_{p2}$, i.e., when the condition of $\vec{M}_{p1} > \vec{M}_f > \vec{M}_{p2}$ is met, magnetic force will attract Type 1 particles/cells towards field maxima while the magnetic force pushes Type 2 particles/cells towards field minima, as shown in Figure 1.2e. In this way, particles can be distinguished and separated solely based on their magnetizations in a simple microfluidic channel. It should be noted here that the volume

of particles now only affects the magnitude, but not the direction of magnetic forces. In another example, one can create a concentration gradient of magnetic liquids in a channel so that particles/cells with magnetizations of $\vec{M}_p$ will naturally migrate towards the location where $\vec{M}_p = \vec{M}_f$, in order to minimize the magnetic force. The final location of the particles/cells can be used to measure their magnetic susceptibilities.

Corresponding to the first example, ferrofluids was used to create both positive and negative magnetophoresis in one system. Liang et al.[124] used a ferrofluid to separate 2.85 μm diamagnetic particles and 10 μm magnetic particles in a T-shaped channel. The magnetization of this ferrofluid was larger than that of diamagnetic particles but lower than that of magnetic particles. As a result, 10 μm magnetic particles were attracted towards the magnet, while 2.85 μm diamagnetic particles were pushed away. Zhu et al.[125] combined both positive and negative magnetophoresis in a ferrofluid to separate magnetic and diamagnetic particles of similar sizes (7-8 μm), as shown in Figure 1.8a. Moreover, they chose a ferrofluid with its magnetization falling in between the magnetizations of two different types of magnetic particles (2.8 μm and strongly magnetic; 8.2 μm and weakly magnetic particles) and successfully separated them.

Corresponding to the second example, Kang et al.[126] developed a scheme termed as "isomagnetophoresis", where they created a gradient of a paramagnetic salt solution using Gd·DTPA in a microchannel. The gradient was created so that magnetic particles migrate towards a location where its magnetization ($\vec{M}_p$) will eventually balance the surrounding medium ($\vec{M}_f$), *e.g.*, $\vec{M}_p = \vec{M}_f$. Diamagnetic particles flowed through this gradient, as shown in Figure 1.8b, and their eventual positions were used to distinguish

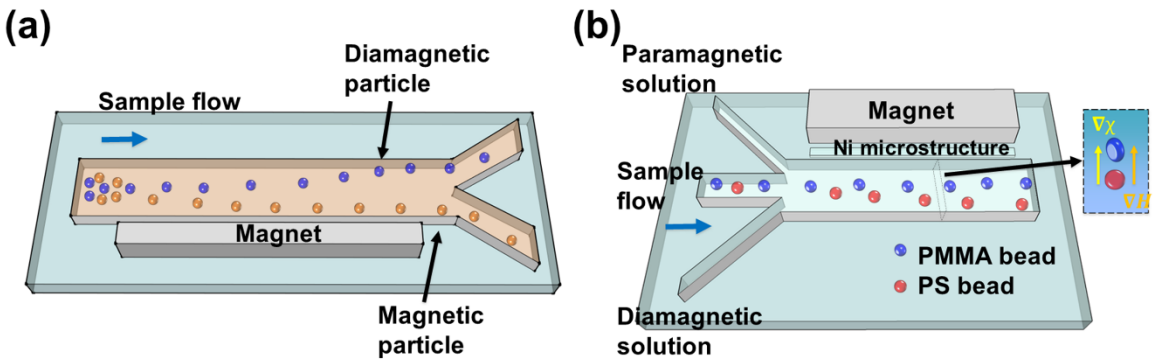

Figure 1.8: Schematic representations of magnetization contrast-based manipulation. (a) Separation of magnetic and diamagnetic particles of similar size using both positive and negative magnetophoresis. Reproduced from ref.[125] (b) Isomagnetophoretic discrimination of particles with subtle difference of magnetic susceptibility in a paramagnetic salt solution. Reproduced from ref.[126] Blue arrow in each figure indicates the flow direction.

the extremely low and close magnetic susceptibilities (~1×10^{-6}) of particles with three different materials (polystyrene, poly(methyl methacrylate), and borosilicate). Later on, Hahn et al.[127] applied this technology in an isomagnetophoretic immunoassay, where iron oxide nanoparticles were used as labels on the surface of microbeads to detect concentrations of analytes down to attomolar levels.

1.4.4 Biocompatibility of Magnetic Liquids

Both paramagnetic salt solutions and ferrofluids are not natural media for cells to live in. For cell manipulation, magnetic liquids need to be biocompatible so that cells remain alive and their functions remain intact during and after the manipulation. A number of studies were conducted on understanding and improving the biocompatibility of magnetic liquids, which are reviewed below and summarized in Table 1.4.

Biocompatibility of Paramagnetic Salt Solution

Winkleman et al.[45] examined the biocompatibility of Gd·DTPA solution on fibroblast cells (NIH 3T3) and yeast cells (*Saccharomyces cerevisiae*). At a concentration

Table 1.4: Summary of magnetic liquids biocompatibility.

Magnetic liquids	Concentrations	pH	Cell type	Short-term viability	Long-term proliferation	References
Gd·DTPA	0, 4, 40, and 200 mM	7.2	NIH 3T3 cells/ *Saccharomyces cerevisiae*	Survived and grew over 2 d at 40 mM/ Viability was similar at all concentrations	0-40 mM didn't inhibit the cell growth/ 40 and 200 mM inhibit cell division	[45]
Gd·DTPA	39, 79 and 240 mM	NA	HaCaT cells	90% at 39 mM and 87% at 79 mM after 3 h, died at 240 mM	NA	[31]
Gd·BOPTA/ Gd·DOTA/ Gd·HP·DO3A	0, 10, 25, 50, 85, and 100 mM	NA	Jurkat cells	~40% on 1st d at 100 mM/ ~75% on 1st d at 100 mM/ >90% on 1st d at all concentrations	25-100 mM inhibited the cell division/ Cells proliferated normally below 25 mM/ Cells proliferated almost normally at all concentrations	[128]
Gd solution	0, 30, 50, and 100 mM	Neutral	JH-EsoAd1 cells	~100% at all concentrations on 1st d	Maintained normal proliferation rates over 5 d	[61]
[1]BSA coated ferrofluid	0, 15, 30, and 45 mg mL^{-1}	NA	HUVECs	>95% at all concentrations up to 2 h	Maintained normal proliferation rates (to confluence)	[39]
[1]Citrate stabilized ferrofluid	0, 20, 40, 50, 60, 80, and 100 mM	7.4	Red blood cells	75%	NA	[38]
[1]Graft copolymer functionalized ferrofluid	0.30%, 0.79%, and 1.03% v/v	6.8	Red blood cells/ HeLa cells	100 % at all concentrations up to 2 h/ ~90 at all concentrations up to 2 h	NA	
[2]EMG 408 ferrofluid	1.1% v/v	~7	*Escherichia coli*/ *Saccharomyces cerevisiae*	Remained almost unchanged viability over 2 d	NA	[44]
[2]EMG 408 ferrofluid	0.3% v/v	~7	*Saccharomyces cerevisiae*	10% reduction in the number of cells over 24-48 h	NA	[93, 100, 103]

[1]Custom-made ferrofluids and [2]commercially available from Ferrotec Corporation.

of 40 mM, Gd·DTPA solution did not cause cell death within 48 h, and the growth of fibroblast cells was not inhibited. However, when its concentration was greater than 4 mM, fibroblast cells in the solution cannot attach to substrates. Furthermore, they examined the viability of yeast cells in different concentrations of Gd·DTPA solution. They showed that the cell viability was similar at all concentrations of Gd·DTPA solution; however, they found that normal cell proliferation was inhibited when the concentration was greater than 4 mM. A 6-fold cell number reduction was found at 40 mM Gd·DTPA, and 24-fold reduction, at 200 mM Gd·DTPA. Rodríguez-Villarreal et al.[31] examined the viability of HaCaT cells in an aqueous Gd·DTPA solution over several h. They concluded that Gd·DTPA in phosphate buffered saline (PBS) solution showed good biocompatibility for HaCaT cell at a concentration of 39 mM, resulting in a 90% viability after 3-h incubation. The viability was reduced to 54% after 4 h. Similarly, the HaCaT cell viability in the 79 mM solution was 87% after 3-h incubation and 44% after 4-h incubation; however, the cells died immediately when they were exposed to Dulbecco's modified eagle medium (DMEM) containing Gd·DTPA solution. Kauffmann et al.[128] studied the viability and growth curve of Jurkat cells in the presence of gadobenate dimeglumine (Gd·BOPTA), gadoterate meglumine (Gd·DOTA) and gadoteridol (Gd·HP·DO3A) contrast agents at different concentrations. Gd·BOPTA was found to be more toxic than the other two solutions. They showed that more than 50% of cells died within the first day in Gd·BOPTA solution (100 mM). 30-40% of cells died after 2 days in Gd·DOTA solution (above 85 mM). The Jurkat cells were able to continue to proliferate normally even at high concentrations of Gd·HP·DO3A solution (100 mM). More than 80% cell viability was shown consistently across different concentrations of

Gd·HP·DO3A (0, 10, 25, 50, 85, and 100 mM). Durmus et al.[61] examined the viability of JH-EsoAd1 cells (esophageal adenocarcinoma cell line) in different concentrations of a paramagnetic gadolinium solution (0, 30, 50, and 100 mM). The cells were directly exposed to DMEM culture medium containing gadolinium solution. More than 95% of cells were kept alive at all concentrations of the paramagnetic gadolinium solution examined after 5 days of culture. Their results indicated that no significant difference in cell viability was observed between a control group and gadolinium solution group. Cell proliferation profile showed that these cells maintained their normal proliferation rates even after being exposed to different concentrations of gadolinium solution.

Biocompatibility of Ferrofluids

As discussed previously, biocompatible ferrofluids are necessary for live cell manipulation, and progress has been made towards this goal. For example, Krebs et al.[39] examined the cytotoxicity of a bovine serum albumin (BSA) coated ferrofluid on HUVECs (human umbilical vein endothelial cells). A short-term viability test showed that the cells had above 95% viability after 2-h exposure in this custom-made ferrofluid. The long-term proliferation results indicated that the cells were able to maintain normal proliferation after 2-h exposure to this ferrofluid. Kose et al.[38] developed a citrate stabilized ferrofluid with a pH of 7.4. The optimum citrate concentration was determined to be 40 mM to make the ferrofluid biocompatible and stable for blood cells. They showed that 75% of blood cells remained viable after several hours' exposure. Zhu et al.[44] examined the viabilities of both *Escherichia coli* and *Saccharomyces cerevisiae* in EMG 408 ferrofluids. They concluded that this ferrofluid possessed minimal detrimental effects on the viability of both cell types after 2 h of exposure. No significant change was

found in Colony Forming Units (CFU) counts of *Escherichia coli* and *Saccharomyces cerevisiae* between ferrofluids incubation and control medium incubation. Zeng et al.[103] also tested the viability of *Saccharomyces cerevisiae* in EMG 408 ferrofluids. They observed a 10% reduction in the number of cells after focusing tests, compared to the original cell suspension in the medium. Similar viability tests of live yeast cells were also conducted in later reports.[93, 100] Recently, a water-based ferrofluid was synthesized by Zhao and Zhu et al.[95] with its maghemite nanoparticles stabilized by graft copolymer (polymethyl methacrylate-polyethylene glycol), and a pH of 6.8. Cell viability tests showed consistently 100% viability for mouse blood cells, and ~90% viability for HeLa cells across different concentrations of this ferrofluid (0.30%, 0.79% and 1.03% of volume fraction), after 2 h of exposure.

1.5 Conclusion and Outlook

Although using magnetic liquids to manipulate particles and cells in microfluidic systems is a relatively new concept, it has resulted in many exciting techniques and applications. Both paramagnetic salt solutions and ferrofluids have been used as surrounding media in this "negative magnetophoresis" concept, in order to direct the motions of particles and cells in a label-free and low-cost manner. Three physical properties of the particles and cells, including their size, density, as well as magnetization, are currently being exploited as manipulation specificities for a variety of interesting applications, including separation, focusing, trapping and concentration determination of particles and cells, determination of cells' density, and measurement of particles' magnetic susceptibilities.

Future directions of this field could involve optimization of existing techniques, continuous development of new techniques, and finding new applications for them. Two recent applications of this concept involve high-efficiency size-based sorting of cervical HeLa cells from whole blood in a biocompatible ferrofluid,[95] and measuring and separating cells of different densities in paramagnetic salt solutions,[56, 61] presenting a preview of the exciting and immediate future for its application in cell manipulation.

A long-term direction for negative magnetophoresis, which received a lot of attention in recent years, is the enrichment of circulating tumor cells (CTCs) in peripheral blood. CTCs are cancer cells that are disassociated from tumors and circulate in the bloodstream. There is great interest in circulating tumor cell (CTC) enrichment because of the use of these rare cells in "fluid biopsy". This accessible "fluid biopsy" would permit noninvasive access to tumor cells to perform the same molecular assays that were done on traditional biopsies.[129] Additionally, changes in the number of CTCs in the blood after initiation of cancer treatment may help identify whether or not the tumor is responding to the treatment or not. Separating CTCs from peripheral blood is thus an attractive first step to realize its great potential. It requires the development of highly sensitive and high-throughput separation technologies because CTCs are extremely rare in blood circulation, occurring at a concentration of 1-100 CTCs every 1 billion of red blood cells and 1 million of white blood cells.[130] Using magnetic liquids to separate CTCs from blood could be attractive because of its label-free nature and low cost. CTCs have a much larger size (~20 μm in diameter) than most of the blood components (red blood cells ~6-8 μm in diameter, while the majority of white blood cells are ~12 μm in diameter). In addition, CTCs have a different density than that of WBCs.[61] A

combination of size and density differences may potentially be exploited in either paramagnetic salt solutions or ferrofluids for CTC separation, provided that throughput and separation efficiency of negative magnetophoresis can be optimized to meet the criteria.

Despite the current progress, biocompatibility of magnetic liquids remains to be a significant challenge facing this technique before it can be reliably used to manipulate cells. The biocompatibility of magnetic liquids is critical to preserving cell integrity during the cell manipulation process. In order to investigate the impact of the process on cell integrity, one needs to examine both short-term viability and long-term cell functions following the manipulation. For example, one can examine the short-term cell viability using a live/dead cell staining method. The operating parameters will have to remain the same as those used in the realistic manipulation experiments. After processing all of the samples, target cells will need to be stained to determine their viability. It is also important to examine whether cells continue to function normally after the manipulation process. Target cells will need to be cultured, and proliferation of these cells will have to be studied through imaging their division over time. Other cellular functions, including gene expression and nanoparticle uptake, may also need to be monitored, depending on the specific application. Only after such a rigorous study for each cell type, a specific magnetic liquid can then be determined whether it is truly biocompatible.

1.6 Overview of the Dissertation

The main objective of this dissertation is to study the separation of particles and cells combining negative magnetophoresis (ferrohydrodynamics) and microfluidics, and to apply it towards rare cancer cell separation.

Chapter 2 will present a detailed study of synthesis and characterization of biocompatible ferrofluids for cell separation. Typical ferrofluids used in microfluidic applications are water-based. The issues of using water-based ferrofluids for particle or cell manipulation are two-fold. First, light diffraction from the high concentration of magnetic nanoparticles in ferrofluids makes it difficult to directly observe particles or cells. To solve this problem, microfluidic devices with shallow channels and ferrofluids with low solid volume fraction are needed. Second, biocompatible ferrofluids are necessary for live cell manipulation.

Chapter 3 will present a label-free and low-cost ferrohydrodynamic cell separation scheme using HeLa cells and mouse red blood cells. The separation was based on cell size difference and conducted in a custom-made biocompatible ferrofluid that retained the viability of cells during and after the assay for downstream analysis. The scheme offers moderate-throughput (~10^6 cells h^{-1} for a single channel device), extremely high recovery rate (>99 %) and a purity of 100% without the use of any label. Cervical cancer screening would greatly benefit from the elimination of blood, mucin, and debris. The throughput and high separation efficiency of the current ferrohydrodynamic separation systems will effectively remove contaminating blood from exfoliated cervical samples. Removing contaminating blood will also facilitate examination and testing of other exfoliated and fine needle aspirate cytology specimens. The current device design is limited by moderate throughput (~10^6 cells h^{-1}) and therefore cannot be used for high-throughput or rare cell separation.

Chapter 4 will present a biocompatible and label-free cell separation method using ferrofluids that can separate a variety of low-concentration cancer cells from cell

culture lines (~100 cancer cells mL^{-1}) from undiluted white blood cells, with a throughput of 1.2 mL h^{-1} and an average separation efficiency of 82.2%. A microfluidic device is designed and optimized specifically to shorten the exposure time of live cells in ferrofluids from hours to seconds, by eliminating time-consuming off-chip sample preparation and extraction steps and integrating them on-chip to achieve one-step process. While still at its early stage of development, this method could be a promising tool for rare cell separation because of its excellent biocompatibility, label-free operation, and performance with cultured cancer cells, along with potential for device scale-up, multiplexing, and further optimization. The current cell separation device is only tested with spiked cancer cells, isolation of tumor cells from clinical samples needs to be further validated to demonstrate the clinical utility of the current device.

Chapter 5 will present a laminar-flow microfluidic device that is capable of enriching rare CTCs from patients' blood in a biocompatible manner with a high throughput (6 mL h^{-1}) and a high recovery rate (92.9%). The developed device could become a complementary tool for CTC separation for its high recovery rate and excellent biocompatibility, as well as its potential for further optimization and integration with other separation methods.

CHAPTER 2

BIOCOMPATIBLE FERROFLUIDS

2.1 Introduction

Typical ferrofluids used in microfluidic applications are water-based. Despite recent progress, using water-based ferrofluids for cell manipulation is still a work in progress, limited by issues originated from its poor biocompatibility. For cell applications it is desirable to maintain their viability during separation for downstream analyses. In the past, it has demonstrated that both *E. coli* and *S. cerevisiae* could survive in a commercial ferrofluid for up to 2 hours.[44] However, the requirements of keeping mammalian cells alive differ significantly from those of *E. coli* and *S. cerevisiae*. For mammalian cells, materials, pH, and surfactants of ferrofluids need to be rendered biocompatible, at the same time the overall colloidal system of ferrofluids must be maintained during separation. Nanoparticles within ferrofluids for cell applications need to be biocompatible, such as magnetite or maghemite.[75] The pH value of ferrofluids needs to be compatible with cell culture and maintained around at 7. Salt concentration, tonicity, and surfactant must be carefully chosen close to physiological conditions to reduce cell death. Although these are stringent requirements, progress has been made towards synthesizing biocompatible ferrofluids, which has been reviewed in the section of Biocompatibility of Ferrofluids in Chapter 1. In this chapter, a detailed synthesis and characterization of biocompatible ferrofluids with pH 7, balanced salt concentration, and graft copolymer functionalized maghemite particles will be presented for cell separation.

2.2 Synthesis of Biocompatible Ferrofluids

A water-based ferrofluid with maghemite nanoparticle (Fe_2O_3) was synthesized by a chemical co-precipitation method and made biocompatible following a protocol previously described.[131, 132] Details of the ferrofluid synthesis and functionalization are listed here.

Ammonium hydroxide solution (28%), iron (II) chloride tetrahydrate (99%), iron (III) chloride hexahydrate (97%), nitric acid (70%), iron (III) nitrate nonahydrate (98%), and sodium hydroxide (98%) were purchased from a commercial vendor (Sigma-Aldrich, St. Louis, MO). All reagents were used as received. In a typical reaction, 50 mL of ammonium hydroxide solution was quickly added to a mixture of 100 mL of 0.4 M iron (II) chloride tetrahydrate and 0.8 M iron (III) chloride hexahydrate and was followed by stirring at room temperature for 30 minutes. The suspension was then centrifuged at 2000×*g* for 3 minutes and the precipitate was dispersed in 200 mL of 2 M nitric acid and 0.35 M iron (III) nitrate nonahydrate. The mixture was maintained at 90 ^{0}C for 1 hour. During this time, the color of the mixture changed from black (Fe_3O_4) to reddish brown (Fe_2O_3). The maghemite nanoparticle suspension was centrifuged at 3000×*g* for 3 minutes and finally dispersed in 120 mL of deionized (DI) water, yielding a stable dispersion with a pH of 1.5-2. The pH of the dispersion was adjusted to 2.9 by 1 M sodium hydroxide solution. 30 mL of Atlox 4913 (Croda, Edison, NJ), a graft copolymer solution, was added to the dispersion and stirred for 5 minutes before raising pH to 7.0. The dispersion was then vigorously stirred at room temperature for 1 hour, and the resulted ferrofluid was dialyzed with a dialysis membrane (Spectrum Labs, Rancho Dominguez, CA) against DI water for one week. DI water was refreshed every 24 hours.

After dialysis, excess water was vaporized at 72 ^{0}C. Finally, 10% (v/v) 10× Hank's balanced salt solution (HBSS; Life Technologies, Carlsbad, CA) was added into the ferrofluid to render it isotonic for cells followed by adjusting pH to 7.0. Sterile filtration of ferrofluid was performed with a 0.2 μm filter (VWR, Radnor, PA) and ferrofluids were exposed to UV light for 12 hours before experimental use.

2.3 Characterization of Biocompatible Ferrofluids

Size and morphology of maghemite nanoparticles were characterized via transmission electron microscopy (TEM; FEI, Eindhoven, the Netherlands). Magnetic properties of the ferrofluid were measured at room temperature using a vibrating sample magnetometer (VSM; MicroSense, Lowell, MA) with a 2.15 T electromagnet. The magnetic moment of ferrofluid was measured over a range of applied fields from -20 to +20 kOe. The measurements were conducted in step field mode at a stepsize of 200 Oe. Zeta potential of the ferrofluid was measured with a Zetasizer Nano ZS (Malvern Instruments, Westborough, MA). The hydrodynamic diameter of nanoparticles was measured by dynamic light scattering (DLS). The viscosity of ferrofluids was characterized with a compact rheometer (Anton Paar, Ashland, VA) at room temperature.

We measured the saturation magnetization of the as-synthesized ferrofluid to be 0.96 kA m^{-1}, as shown in Figure 2.1a. Considering the bulk magnetization of maghemite is about 370 kA m^{-1},[133] we estimated the volume fraction of the magnetic content of the ferrofluid to be 0.26%. The low volume fraction of the ferrofluid not only leaded to good biocompatibility for live cells, but also enabled us to observe cell motion in microchannel directly with bright-field microscopy, which was difficult with opaque ferrofluids of high solid volume fractions. Viscosity of ferrofluid was measured to be 2.92 mPa·s (Figure

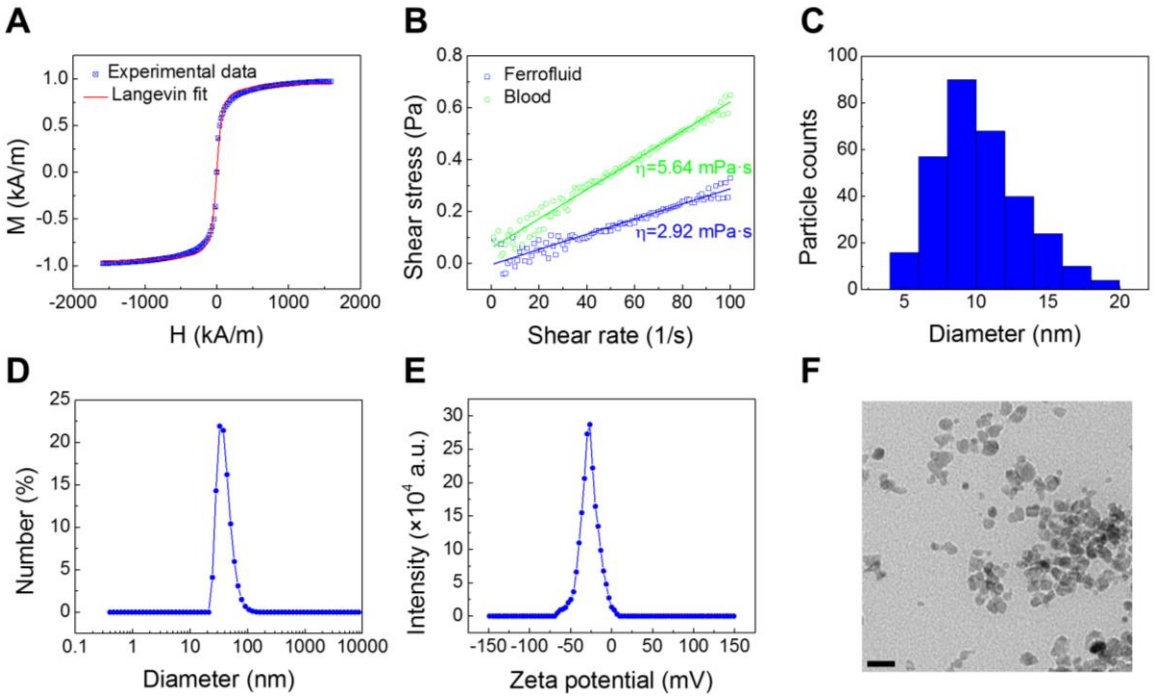

Figure 2.1: Characterization of custom-made ferrofluids. (a) The magnetization of the as-synthesized ferrofluid. Solid red lines are the fitting of the experimental data to the Langevin function. The saturation magnetization of this ferrofluid was 0.96 kA m^{-1}, corresponding to a 0.26% volume fraction or concentration. (b) Rheological plots of the ferrofluid and blood. The viscosity of ferrofluid was measured to be 2.92 mPa·s. (c) Size distribution of maghemite nanoparticles within the ferrofluid (d=10.24 ± 2.52 nm). (d) Size distribution of maghemite nanoparticles was measured by dynamic light scattering (DLS). Hydrodynamic diameter was 40.77 ± 12.71 nm. (e) Zeta potential of ferrofluid was measured to be -27.2 ± 11.4 mV, indicating a negative surface charge on the particles. (f) A transmission electron microscopy (TEM) image of the maghemite nanoparticles. Scale bar: 20 nm.

2.1b). Figures 2.1c and f show size distribution and a sample TEM image of maghemite nanoparticles of the custom-made ferrofluid. The particles had a mean diameter of 10.24 nm with a standard deviation of 2.52 nm. The hydrodynamic diameter was 40.77 ± 12.71 nm because of the polymer coating, as shown in Figure 2.1d. The surface charge of the particles was negative, measured by Zeta potential of -27.2±11.4 mV (Figure 2.1e).

The ferrofluid was made to be isotonic and its pH was adjusted to 7.0 for biocompatible cell manipulation. The short-term viability of cancer cells in ferrofluids

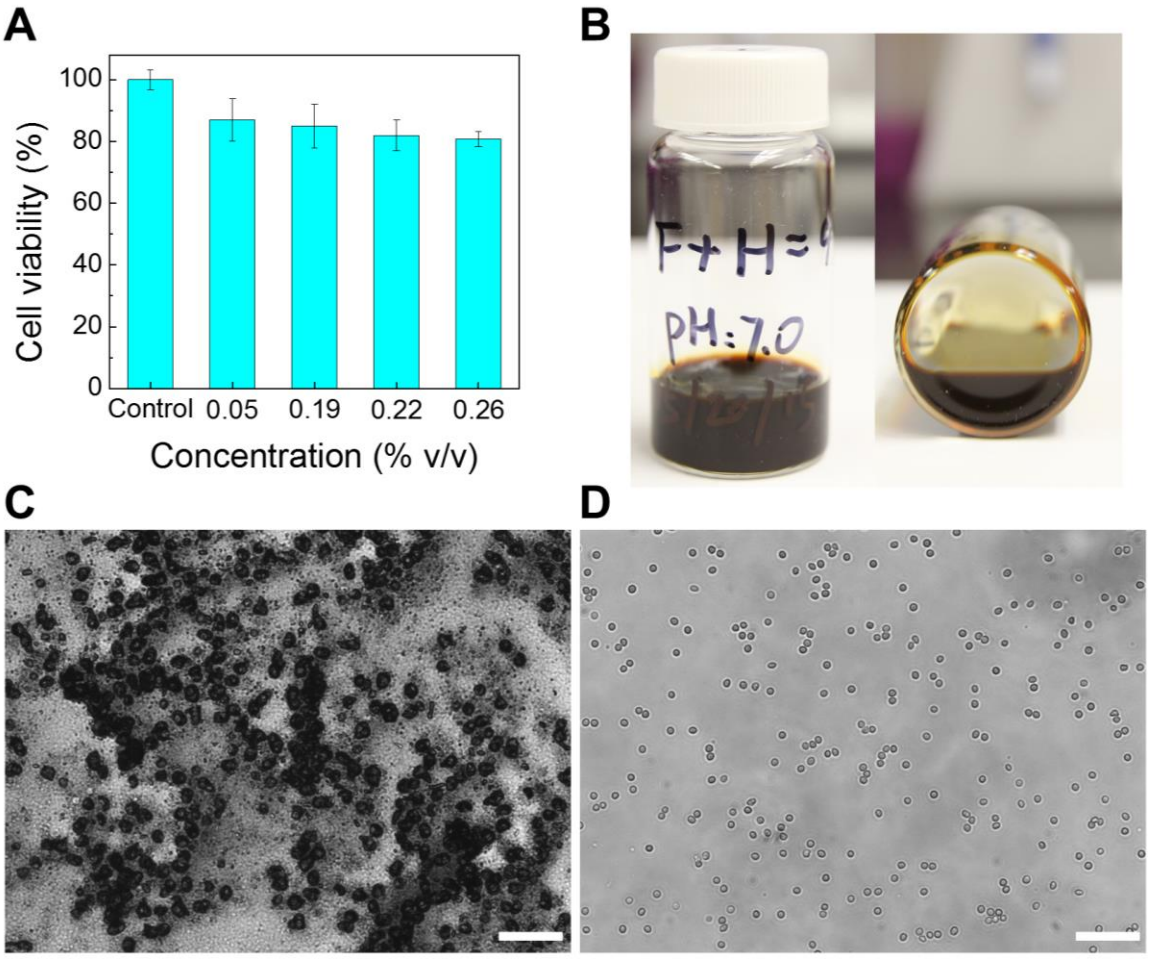

Figure 2.2: Biocompatibility and colloidal stability of ferrofluid. (a) Cell viability of H1299 lung cancer cells in different concentrations of ferrofluids was evaluated by a MTT assay. Cell viability was 80.8 ± 2.4% after 12-h incubation with a 0.26% (v/v) concentration ferrofluid. (b) Colloidal stability of biocompatible ferrofluids. The maghemite nanoparticles remained colloidally stable for at least 10 months in solution and there was no visible precipitation over time. (c) Blood cells, mixed with a commercial water-based ferrofluid, showed an irreversible flocculation. (d) No flocculation or aggregation of blood cells was found within the biocompatible ferrofluid. Scale bars: 50 µm.

was evaluated by 3-(4,5-dimethylthiazol-2-yl)-2,5-diphenyl-tetrazolium bromide (MTT) assay for 12-h incubation with different concentrations of ferrofluids. The results show that H1299 lung cancer cells had a cell viability of 80.8 ± 2.4% after 12-h incubation with 0.26% (v/v) ferrofluids as shown in Figure 2.2a. Although nanoparticles with larger

diameters were considered to be more biocompatible because they may inhibit direct diffusion across cell membrane,[134-137] we chose this diameter for the nanoparticles to preserve the colloidal stability of ferrofluids against agglomeration due to gravitational settling and magnetic dipole-dipole attraction.[27] Particles with a large diameter are prone to settling and agglomeration, and can disrupt continuous-flow separation. However, at a diameter of ~10 nm, thermal agitation at room temperature is sufficient to keep particles separated. As a result, our ferrofluids remained colloidally stable after at least 10 months' storage (Figure 2.2b). During the cell separation, blood cells mixed with biocompatible ferrofluid showed no flocculation or aggregation, but an irreversible flocculation was observed when blood cells mixed with a commercial water-based EMG 408 ferrofluid, as shown in Figures 2.2c and d.

CHAPTER 3

LABEL-FREE AND CONTINUOUS-FLOW FERROHYDRODYNAMIC SEPARATION OF HELA CELLS AND BLOOD CELLS IN BIOCOMPATIBLE FERROFLUIDS [1]

[1] W. Zhao, T. Zhu, R. Cheng, Y. Liu, J. He, H. Qiu, L. Wang, T. Nagy, T. D. Querec, E. R. Unger and L. Mao, *Adv Funct Mater*, 2016, **26**, 3990-3998.
Reprinted here with permission of John Wiley and Sons.

3.1 Abstract

In this study, we demonstrated a label-free, low-cost and fast ferrohydrodynamic cell separation scheme using HeLa cells (an epithelial cell line) and red blood cells. The separation was based on cell size difference and conducted in a custom-made biocompatible ferrofluid that retained the viability of cells during and after the assay for downstream analysis. The scheme offers moderate-throughput (~10^6 cells h^{-1} for a single channel device) and extremely high recovery rate (>99 %) without the use of any label. We envision this separation scheme will have clinical applications in settings where rapid cell enrichment and removal of contaminating blood will improve the efficiency of screening and diagnosis such as cervical cancer screening based on mixed populations in exfoliated samples.

3.2 Introduction

Microfluidic cell separation based on magnetic forces (magnetophoresis) has unique advantages over other competing techniques.[22-25, 138] Magnetic force does not interact directly with cells, minimizing potential detrimental effects on them. Systems for magnetophoresis are simple and low-cost, only requiring microchannels and permanent magnets/electromagnetic coils. As a result, magnetophoresis has been widely used to manipulate microparticles and cells with different magnetic susceptibilities.[30-33, 139-142] Despite these advantages, sample preparation in magnetophoretic assays suffers from time-consuming and labor-intensive labeling steps,[33] as it uses magnetic beads to tag cells in order to achieve specific manipulation. It is therefore highly beneficial to develop a label-free version of magnetophoresis. “Negative magnetophoresis”[26] caters to this need by eliminating the labeling steps through the incorporation of a special medium into the

assay. This medium, typically magnetic fluids such as a paramagnetic salt solution[40, 41, 54, 89] or a ferrofluid,[38, 42, 124] possesses a larger magnetization than the cells. An external magnetic field attracts the magnetic medium, which causes the cells to be preferentially pushed away.[27] Consequently, cells can be manipulated magnetically without the need for tagging them.

Both paramagnetic salt solutions and ferrofluids have been used as media in negative magnetophoresis.[31, 38-41, 69-71, 93] Among the two media, ferrofluids possess much higher susceptibility and magnetization under fields generated by permanent magnets.[27] This leads to a larger magnetic susceptibility difference between the medium and cells (with close to zero susceptibility),[29] and enables its applications in a number of areas related to fast manipulation. Examples include manipulation,[46, 98, 110, 143] separation,[38, 42, 44, 46, 93, 94, 96, 124, 125] concentration,[100, 101] focusing[97, 99] and assembly[82, 84, 144, 145] in ferrofluids. For cell manipulations, Kose et al.[38] separated live red blood cells from sickle cells and bacteria in a citrate stabilized ferrofluid using microfabricated electrodes and channels. Krebs et al.[39] formed linear cell structures in a Bovine Serum Albumin (BSA) coated ferrofluid. Zhu et al.[44] ferrohydrodynamically separated *Escherichia coli* from *Saccharomyces cerevisiae* (Baker's yeast) cells using a commercial ferrofluid with high throughput and efficiency in a continuous-flow fashion. Zeng et al.[93] sorted live yeast cells from polystyrene microparticles in ferrofluids using two offset permanent magnets.

Despite the progress, using water-based ferrofluids for cell manipulation is still a work in progress, limited by difficulties including visualizing and maintaining the viability of mammalian cells in ferrofluids. Light diffraction from the high concentration of magnetic nanoparticles in bulk ferrofluids makes it difficult to directly observe cells

when they are suspended in this media. To address this problem, we combined the use of microfluidic devices with shallow (~100 μm) channels and ferrofluids with low solid volume fraction (<1% v/v) in this study to allow direct observation of cell motion in bright-field microscopy. The second issue of biocompatibility is much more challenging. For cell applications, it is desirable to maintain their viability during separation for downstream analyses. In the past, we have demonstrated both *Escherichia coli* and *Saccharomyces cerevisiae* can survive in a commercial ferrofluid for up to 2 hours.[44] However, the requirements of keeping mammalian cells alive differ significantly from those of *Escherichia coli* and *Saccharomyces cerevisiae.* For mammalian cells, materials, pH value, and surfactants of ferrofluids need to be rendered biocompatible, at the same time the overall colloidal system of ferrofluids must be maintained. Nanoparticles within ferrofluids for cell applications need to be biocompatible, such as magnetite or maghemite.[75] The pH value of ferrofluids needs to be compatible with cell culture and maintained around 7. Salt concentration, tonicity, and surfactant must be carefully chosen close to physiological conditions to reduce cell death. Although these are stringent requirements, progress has been made towards synthesizing biocompatible ferrofluids.[38, 39] In this study, a customized water-based ferrofluid with pH 6.8, balanced salt concentration, and graft copolymer functionalized maghemite particles were used to maintain the viability of HeLa cells and mouse blood cells.

In the remaining of the paper, we describe the materials and methods for separation using a customized ferrofluid, along with cell viability experiments and calibration of the device with polystyrene microparticles. The method is then used to separate defined mixtures of HeLa and blood cells. The cell yield and morphology from

each channel outlet are summarized, indicating extremely high recovery rate and purity. In the end, we discuss potential applications for this technology.

3.3 Results and Discussion

3.3.1 Working Mechanism

The working mechanism of the device is shown in Figure 3.1, which consists of a microchannel and a permanent magnet. Cell mixtures and ferrofluids are injected into the

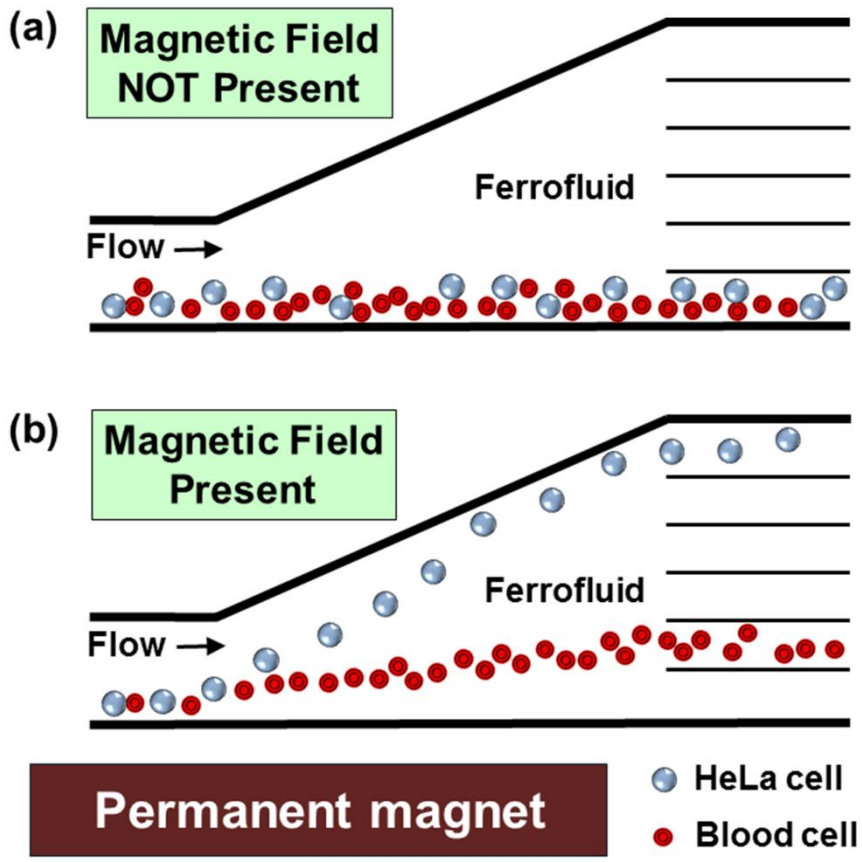

Figure 3.1: Schematic representation of continuous-flow and label-free separation of mammalian cells in biocompatible ferrofluids. (a) Cell mixtures enter and exit the channel together when magnetic fields are not present. (b) When magnetic fields are applied, larger HeLa cells are deflected from their laminar flow paths towards upper outlets by magnetic buoyancy forces. Meanwhile, forces on smaller blood cells lead to a smaller vertical deflection, resulting in a spatial separation of cell mixtures at the end of the channel.

channel by a pressure-driven flow. When the magnet is not present near the channel, both HeLa cells and blood cells enter and exit the channel together, resulting in no separation, as shown in Figure 3.1a. When the magnet is placed close to the channel, deflections of cells from their laminar flow paths occur because of the magnetic buoyancy force. The force acting on cells inside ferrofluids is a body force and is proportional to the volume of cells,[27, 46, 110] which leads to spatial separation of cells of different sizes at the end of the microchannel, as shown in Figure 3.1b. As a result, larger HeLa cells and smaller blood cells exit through different outlets. The device illustrations are shown in Figures 3.2a and b. Dimensions of the microfluidic channel are listed in Figures 3.2c and d.

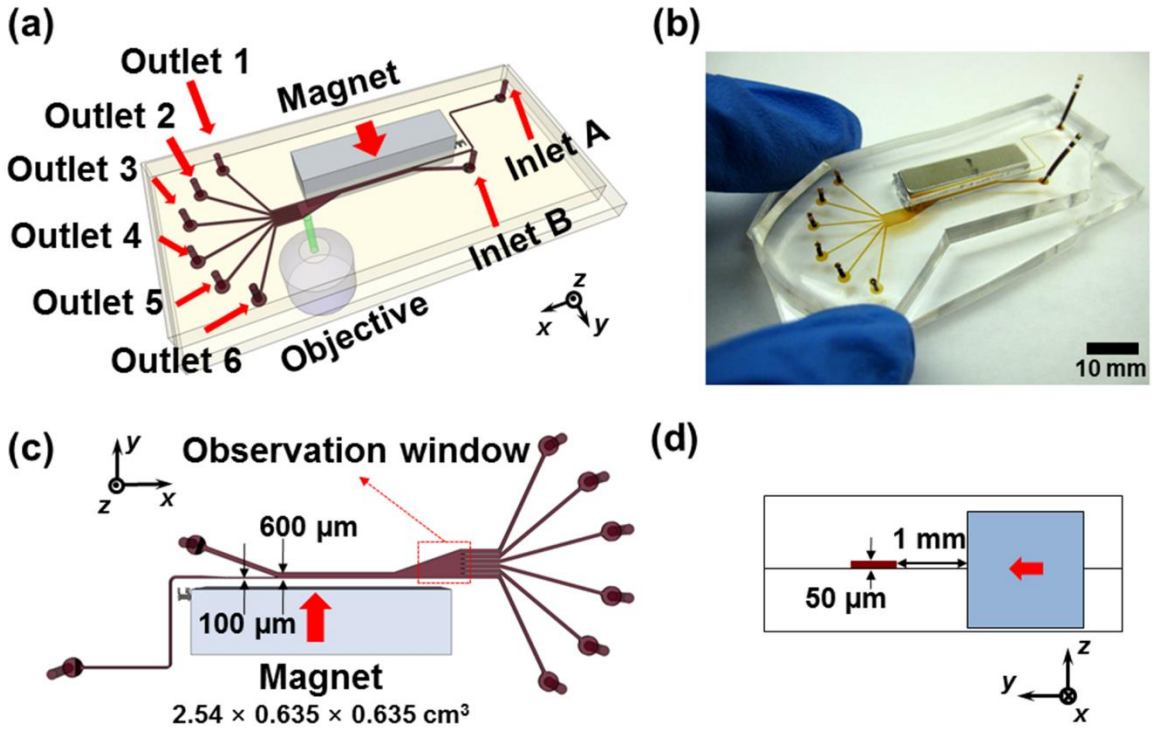

Figure 3.2: Device illustrations. (a) Schematic drawing of the separation device with a permanent magnet and a microfluidic channel. (b) An image of a prototype device. (c) Top-view of the device and relevant dimensions. The red arrow indicates the direction of magnet's magnetization. Red dashed box indicates the location of the observation window in Figures 4-6. (d) Cross-section of the device. The red arrow indicates the direction of magnet's magnetization.

3.3.2 Ferrofluid Properties

Figures 3.3a and b show the Transmission Electron Microscopy (TEM) images and size distribution of maghemite nanoparticles in the ferrofluid. The nanoparticles had an average diameter of 10.25 nm with a standard deviation of 2.96 nm. The small

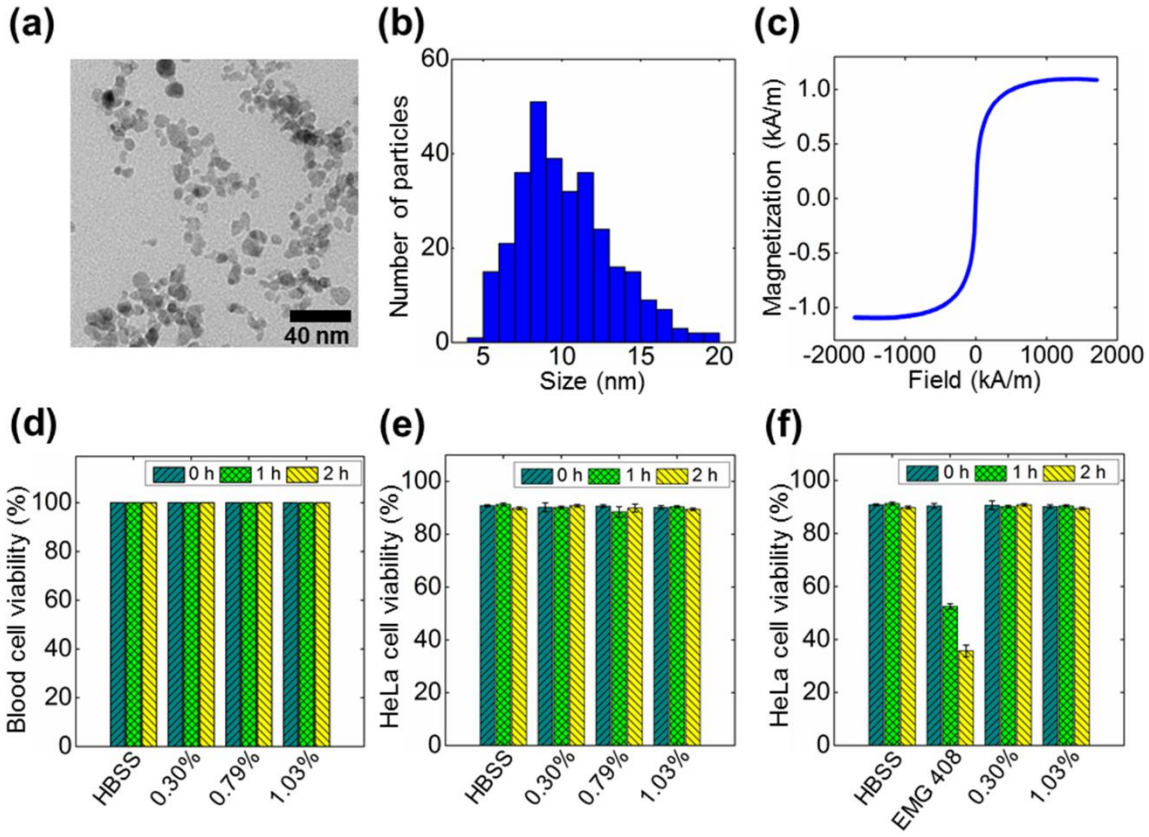

Figure 3.3: Ferrofluid characterization and cell viability test. (a) A TEM image of maghemite nanoparticles. (b) Size distribution of the maghemite nanoparticles within ferrofluid (mean = 10.25 nm and standard deviation =2.96 nm). (c) Magnetization versus applied field curve of the ferrofluid. Saturation magnetization of this sample ferrofluid was 1.10 $kA \cdot m^{-1}$, corresponding to a 0.30% volume fraction. (d) and (e) Cell viability test of mouse blood and HeLa cells in four media: Hank's Balanced Salt solution (HBSS), 0.30%, 0.79% and 1.03% v/v of customized ferrofluids. After 0, 1 and 2 hours' incubation, cell viability was determined with Trypan blue exclusion. Viability of blood in ferrofluids up to 2 hours was consistently 100%, while viability of HeLa cells was 90%. (f) Comparison of viability of HeLa cells in HBSS, EMG 408 and customized ferrofluid (0.30% and 1.03% v/v) as a function of time. EMG 408 shows poor biocompatibility for HeLa cells, resulting in 36% viability after 2 hours. Error bars are from 3 repeats of viability test.

diameter of nanoparticles ensured colloidal stability of the ferrofluid under magnetic fields used in experiments. The coated maghemite nanoparticles remain stable for at least two months. Saturation magnetization of the ferrofluid was measured to be 1.10 kA m^{-1} (Figure 3.3c). Considering bulk magnetization of maghemite particles is 370 kA m^{-1},[133] volume fraction of magnetic materials content within this sample ferrofluid is estimated to be 0.30%. We adjusted the concentration of this ferrofluid in cell viability test and separation experiments via evaporation. In all of experiments, this ferrofluid maintained its excellent colloidal stability and didn't show any sign of particle agglomeration under magnetic fields.

3.3.3 Cell Viability

Figure 3.3d compares the viability of mouse whole blood cells in Hank's Balanced Salt Solution (HBSS; Life Technologies, Carlsbad, CA, USA)), 0.30%, 0.79% and 1.03% volume fraction of maghemite ferrofluids after 0-hour, 1-hour and 2-hour of incubation. The data show consistently 100% cell viability across different concentrations of ferrofluids for at least 2 hours. Figure 3.3e shows a similar test for HeLa cells with close to 90% viability. We conclude from these data that the customized ferrofluids possess minimal detrimental effect to the viability of both mouse whole blood and HeLa cells within 2 hours of exposure. This permits sufficient time to carry out the separation assay as well as potential downstream analyses (*e.g.*, isotope labeling and analysis of gene function, etc.). To illustrate the benefit of using this customized ferrofluids, Figure 3.3f compares the biocompatibility of a commercial water-based magnetite ferrofluid (EMG 408; Ferrotec, Corp., Santa Clara, CA, USA) to the customized ferrofluid. Although the commercial ferrofluid was demonstrated to be biocompatible for

Escherichia coli and *Saccharomyces cerevisiae* cells in our previous study,[44] it showed poor biocompatibility for mammalian HeLa cells, resulting in only 52% cell viability after just 1 hour of incubation, and further reduction to 36% viability after 2 hours.

3.3.4 Device Calibration

In order to optimize the flow rates and magnetic fields for cell separation, we first calibrated the device using spherical polystyrene microparticles with diameters of 15.8 μm (volume of 2065 μm^3) and 5.8 μm (volume of 102 μm^3), which have similar total volume to HeLa cells (3700±1500 μm^3)[146] and mouse red blood cells (66.0±8.3 μm^3).[147] Ideally, we would like to optimize the device for highest cell throughput and best separation efficiency. However, there is always a tradeoff between throughput and separation efficiency. As the throughput increases, the separation efficiency goes down, and vice versa.[14] In this study, we focus on the demonstration of successful separation of HeLa cells and blood. Therefore, flow rates and magnetic fields were optimized in order to maximize the separation distance. Based on the calibrations, we decided to use a flow rate of 8 μL min^{-1} and magnetic field of 340 mT for subsequent cell experiments.

Figure 3.4 summarizes the device performance for microparticle separation. The observation window was located right before channel outlets, as indicated in Figure 3.2c. When magnetic field was not present, microparticles were observed in bright-field mode flowing together near the sidewall of the channel and exiting through Outlets 1 and 2, as shown in the composite micrograph of Figure 3.4a. When magnetic field was present, magnetic buoyancy forces deflected microparticles from their laminar flow paths towards top outlets, as shown in Figures 3.4b-d. Magnetic forces on 5.8 μm microparticles (11 pN according to Equation (3.1)) were in one order of magnitude lower than those on 15.8 μm

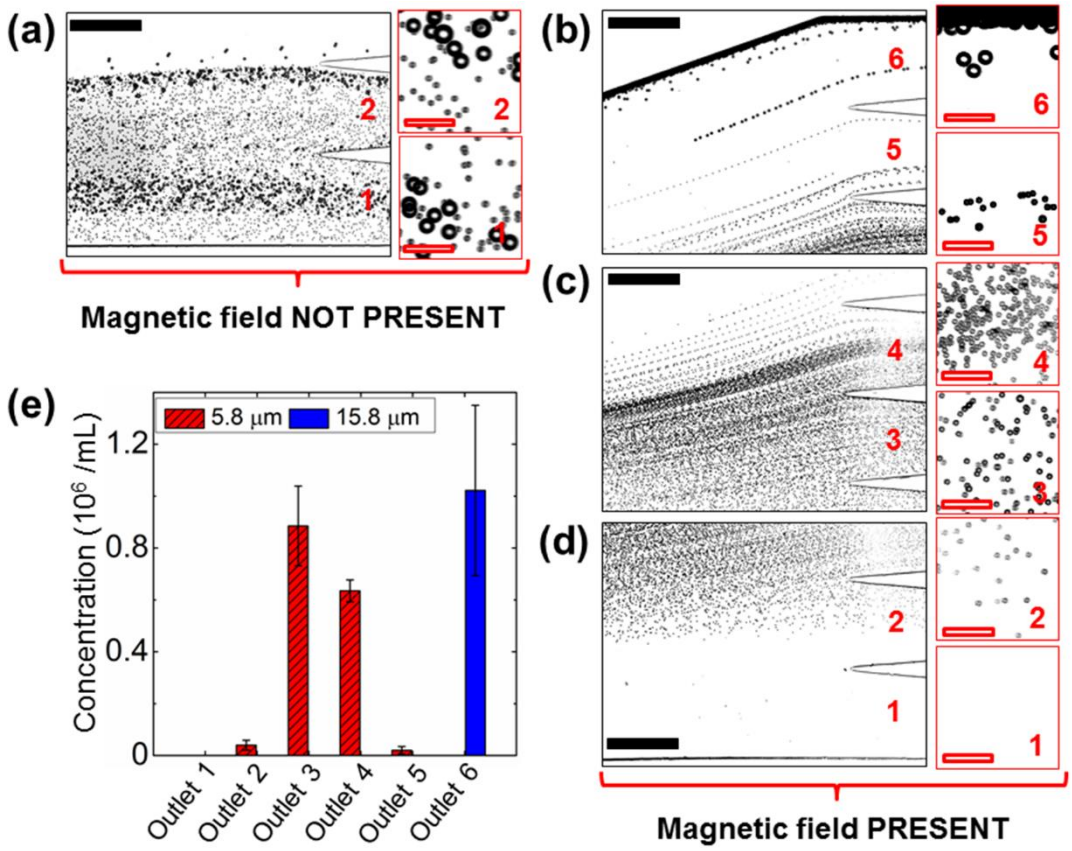

Figure 3.4: Device performance of microparticle calibration. (a) In absence of a magnetic field, microparticle mixtures exited the channel through Outlets 1 and 2. Insets are zoom-in views of the outlets. (b)-(d) When magnetic fields were applied, 15.8 μm microparticles exited through Outlet 6, while 5.8 μm microparticles exited through Outlets 2-5 (labeled in red color number). (e) Type distribution of microparticles at each outlet. 15.8 μm microparticles were exclusively enriched into Outlet 6, while 5.8 μm microparticles were separated into Outlets 2-5. Error bars are from 4 repeats of experiments. Black solid scale bars represent 400 μm, red hollow scale bars represent 50 μm.

microparticles (220 pN according to Equation (3.1)). This resulted in a spatial separation of microparticle mixtures at the end of channel. As shown in Figures 3.4b-d, 5.8 μm microparticles exited the channel through Outlets 2-5, and 15.8 μm microparticles exited the channel through Outlet 6 only. We were able to separate ~10^6 microparticles per hour with 8 μL min^{-1} flow rate. After separation, microparticles collected from each outlet were counted using hemocytometer for distribution analysis, as shown in Figure 3.4e.

The results confirmed that all the 15.8 μm microparticles were enriched into Outlet 6 while only 5.8 μm microparticles were present in Outlets 2-5.

3.3.5 Cell Separation

We tested the device again using a mixture of HeLa cells and 5.8 μm microparticles. The results are summarized in Figure 3.5. Because of the low concentration of maghemite nanoparticles in the ferrofluid, we were able to clearly observe the HeLa cells and record the separation processes using only bright-field microscopy. Figure 3.5a shows the composite micrograph of HeLa cell and 5.8 μm microparticle mixtures, both of which exited the channel through Outlets 1 and 2, when magnetic field was not present. Separation of this mixture was achieved as soon as magnetic field was present, as depicted in Figures 3.5b-d. From the distribution analysis of 4 replicate experiments with different passages of HeLa cells on the same device, as shown in Figure 3.5e, on average 87% of HeLa cells were deflected into Outlet 6, and the 13% HeLa cells were deflected into Outlet 5. 89% of 5.8 μm microparticles exited through Outlets 2, 3, and 4; 11% of 5.8 μm microparticles were present along with HeLa cells in Outlet 5. The recovery rate of HeLa cells was calculated to be 100%. However, a concern here is that some 5.8 μm microparticles were present in Outlet 5, leading to a 86% purity. This is due to the fact that a 5.8 μm microparticle possesses a volume of 102 μm^3, which is almost twice the volume of a mouse red blood cell (66.0±8.3 μm^3).[147] Larger volume of non-magnetic objects leads to greater magnetic buoyancy force and vertical deflection in ferrofluids. When the 5.8 μm microparticles are replaced with mouse red blood cells, we expect the vertical deflection of blood cells to decrease and the separation purity to increase as a result.

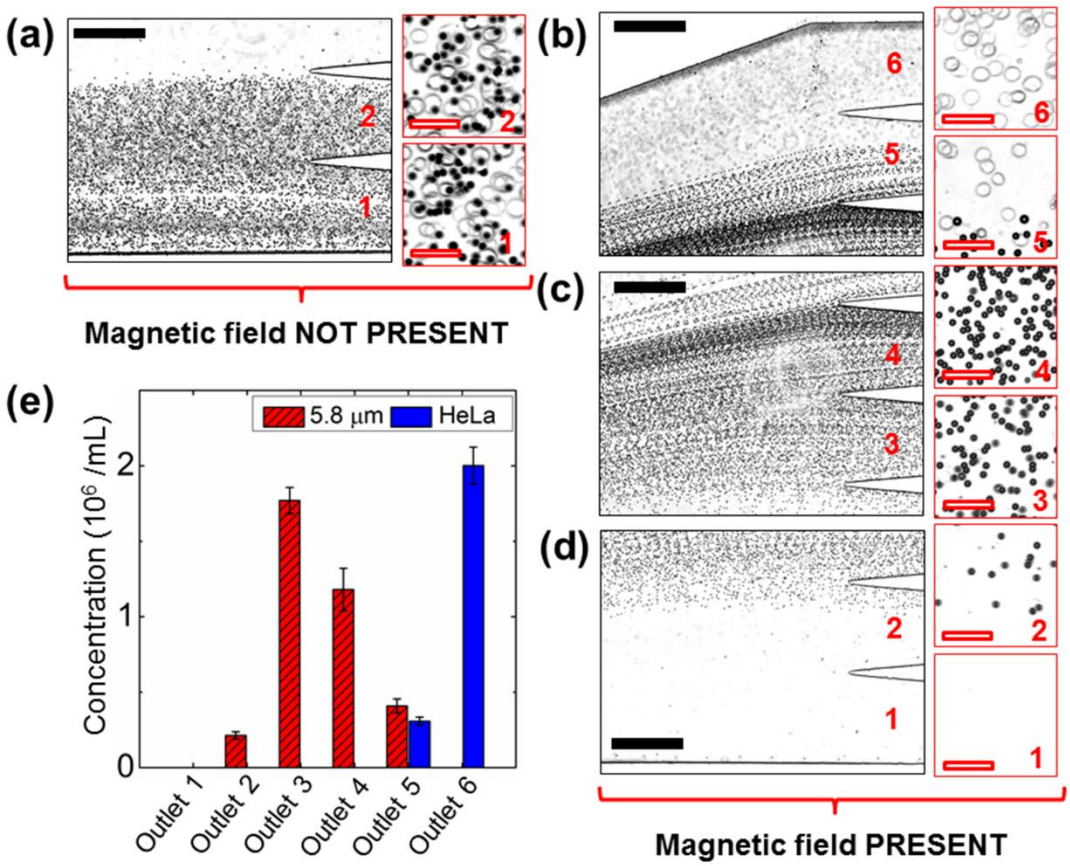

Figure 3.5: Device performance of cell separation. (a) In absence of a magnetic field, cell/microparticle mixtures exited the channel through Outlets 1 and 2. Insets are zoom-in views of the outlets. (b)-(d) When magnetic fields were applied, HeLa cells exited through Outlets 5 and 6, while 5.8 μm microparticles exited through Outlets 2-5 (labeled in red color number). (e) Type distribution of cells/microparticles at each outlet. 87% HeLa cells were separated into Outlet 6, while 5.8 μm microparticles were separated into Outlets 2-5. Error bars are from 4 repeats of experiments. Black solid scale bars represent 400 μm, red hollow scale bars represent 50 μm.

Finally, we separated the HeLa cells and mouse blood cells using above-mentioned flow rates and magnetic fields. The results are summarized in Figure 3.6. In this trial, HeLa cells and mouse red blood cells have the same initial concentrations of 2×10^6 cells mL^{-1}. When magnetic field was not present, both cell types were flowing near the sidewall of the channel and exiting through Outlets 1 and 2, as shown in Figure 3.6a. When magnetic field was present, magnetic buoyancy forces deflected larger HeLa cells

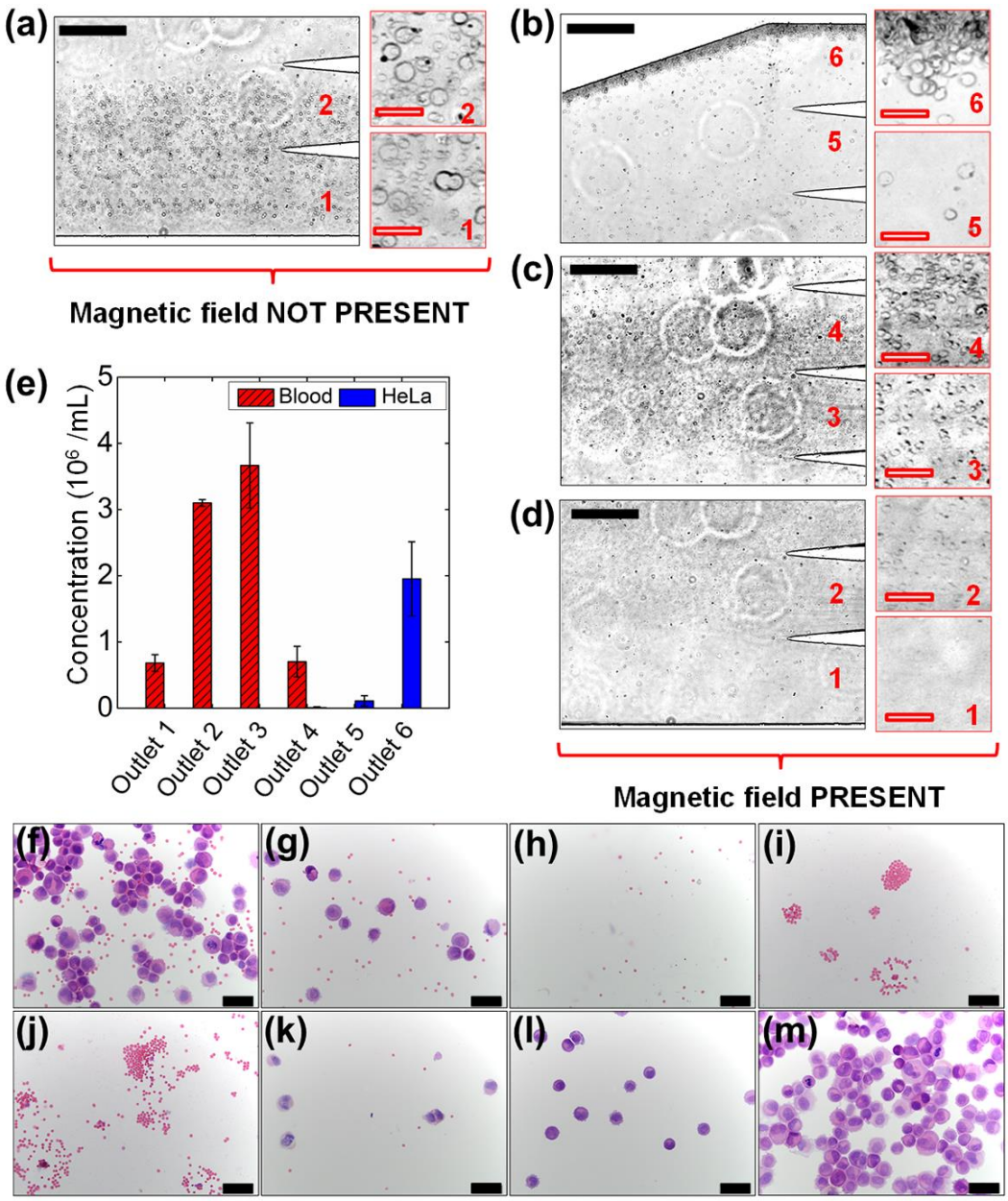

Figure 3.6: Device performance of cell separation and cell morphologies of samples collected from the microchannel outlets. Cells were stained with Hematoxylin and Eosin (H&E) after cytospins. (a) In absence of a magnetic field, cell mixtures exited the channel through Outlets 1 and 2. Insets are zoom-in views of the outlets. (b)-(d) When magnetic fields were applied, HeLa cells exited through Outlets 4, 5 and 6, while mouse blood cells exited through Outlets 1-4 (labeled in red color number). (e) Type distribution of cells at each outlet. More than 99% HeLa cells were enriched into Outlets 5 and 6, while blood cells were separated into Outlets 1-4. (f) and (g) Cells collected from Outlets 1 and 2 when magnetic field was not present. (h)-(m) Cells collected from Outlets 1-6 when magnetic field was present. Error bars are from 3 repeats of experiments. Black solid scale bars in (a)-(d) represent 400 μm, red hollow scale bars in (a)-(d) represent 50 μm, scale bars in (f)-(m) represent 50 μm.

from their laminar flow paths towards Outlets 4, 5 and 6, as shown in Figure 3.6b. Meanwhile, magnetic forces on mouse blood cells were insufficient to deflect them above Outlet 4, as shown in Figures 3.6c and d, resulting in a spatial separation of the initial cell mixtures at the end of channel. From the distribution analysis of 3 replicate experiments on the same device, as shown in Figure 3.6e, on average 94% of HeLa cells ended up in Outlet 6, while the remaining 1% of HeLa cells ended up in Outlet 4 and 5% in Outlet 5. On average 8%, 38%, 45% and 9% of mouse red blood cells were present in Outlets 1, 2, 3 and 4, respectively. The recovery rate of HeLa cells was calculated to be more than 99% and purity was 100%. Cells from each outlet were also inspected for their morphologies using cytospins and Hematoxylin and Eosin (H&E) stain, as shown in Figures 3.6f-m. Figures 3.6f and g show the cell morphologies of the samples collected from Outlets 1 and 2 when magnetic field was not present. Both HeLa cells (large, purple color) and mouse red blood cells (small, pink color) are visible. Figures 3.6h-m show the morphologies of cells from Outlets 1-6 when magnetic field was present. HeLa cells can be observed in Outlets 4-6, while red blood cells can be observed in Outlets 1-4.

One of the immediate applications of this technology we envision is to enrich the cervical specimens for abnormal cells in order to reduce screening time and allow simultaneous detection of diagnostic markers in multiple extracts.[14, 16, 17] Biomarkers based on molecular changes in response to human papillomavirus (HPV) infection and neoplastic progression identified in biopsies are difficult to apply in exfoliated samples because of its heterogeneous nature. Abnormal cells comprise less than 10% of the total cells, and the contribution of local inflammatory cells can be hidden by bleeding during sample collection. For this reason, we tested efficiency of the separation device for spike

samples with 1:10 ratio (HeLa: blood, 2×10^5 cells mL^{-1}: 2×10^6 cells mL^{-1}) and 1:100 ratio (HeLa: blood, 2×10^4 cells mL^{-1}: 2×10^6 cells mL^{-1}). From the distribution analysis of 3 replicate experiments in Figure 3.7, the results show that for 1:10 ratio, on average 87% of HeLa cells were collected from Outlet 6, and 13% of HeLa cells were collected from Outlet 5. For 1: 100 ratio, on average 90% of HeLa cells were collected from Outlet 6, and 10% of HeLa cells were collected from Outlet 5. In both cases, mouse red blood cells were completely separated into Outlets 1-4, while HeLa cells were completely enriched into Outlets 5 and 6. The corresponding recovery rates and purities of HeLa cells were both 100%. The data of recovery rates and purities of HeLa cells were summarized in Table 3.1.

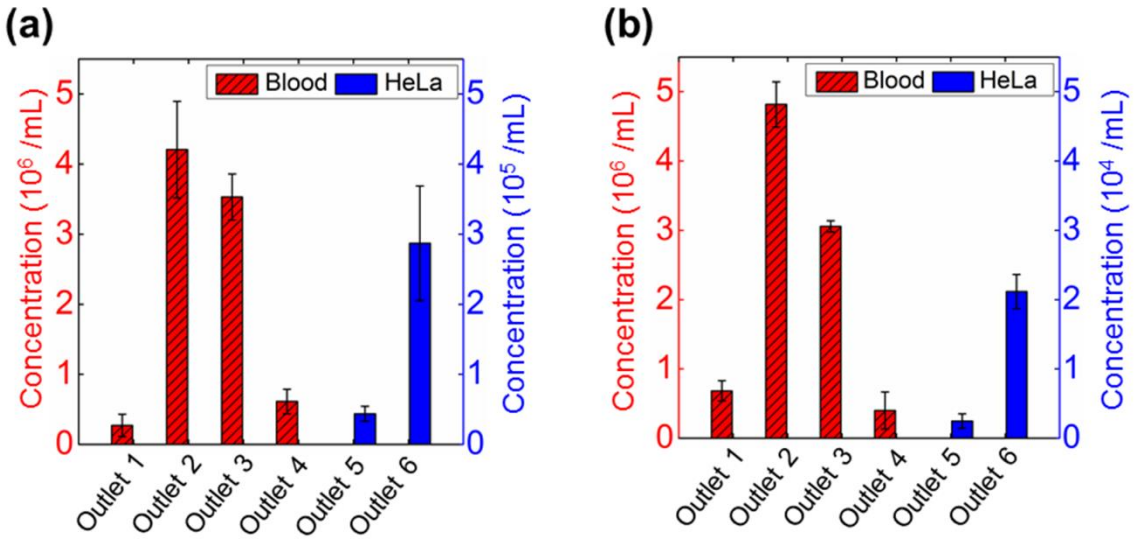

Figure 3.7: Type distribution of cells collected from each outlet at ratios of 1:10 (HeLa: blood, 2×10^5 cells mL^{-1}: 2×10^6 cells mL^{-1}) and 1:100 (HeLa: blood, 2×10^4 cells mL^{-1}: 2×10^6 cells mL^{-1}). (a) 87% HeLa cells were collected in 1: 10 ratio from Outlet 6. (b) 90% HeLa cells were collected in 1: 100 ratio from Outlet 6. Error bars are from 3 repeats of experiments.

Table 3.1: Recovery rate and purity of HeLa cells in device calibration (HeLa: 5.8 μm microparticles, 2×10^6 cells mL^{-1}: 2×10^6 particles mL^{-1}), 1: 1 (HeLa: blood, 2×10^6 cells mL^{-1}: 2×10^6 cells mL^{-1}), 1:10 (HeLa: blood, 2×10^5 cells mL^{-1}: 2×10^6 cells mL^{-1}) and 1:100 (HeLa: blood, 2×10^4 cells mL^{-1}: 2×10^6 cells mL^{-1}) ratios. Data were expressed as mean ± standard deviation, n=3.

	Device calibration	1:1 ratio	1:10 ratio	1:100 ratio
Recovery rate [%]	100.0±0.0	99.6±0.8	100.0±0.0	100.0±0.0
Purity [%]	85.6±2.1	100.0±0.0	100.0±0.0	100.0±0.0

3.4 Conclusions and Outlook

In this study, we developed a water-based biocompatible ferrofluid that not only maintains its colloidal stability under strong magnetic fields, but also keeps HeLa cells and mouse blood cells alive for up to two hours. This ferrofluid, due to its low magnetic nanoparticle concentration, also allows direction observation of cells under microscope. We showed that ferrohydrodynamic cell separation in this biocompatible ferrofluids offered moderate-throughput (~10^6 cells h^{-1} in this study) and extremely high separation efficiency (>99 %) for HeLa and blood cells without the use of labels. We envision an immediate application of this separation technology is to enrich the cervical specimens for abnormal cells. Frequent causes of unsatisfactory liquid-based cervical cytology (LBC) slides include obscuration by erythrocytes, leukocytes, and mucin.[148] Cervical cancer screening would greatly benefit from elimination of blood, mucin, and debris. The throughput and high separation efficiency of the current ferrohydrodynamic separation systems will effectively remove contaminating blood from exfoliated cervical samples. Removing contaminating blood will also facilitate examination and testing of other exfoliated and fine needle aspirate cytology specimens. Fractionation of epithelial cell populations into normal and abnormal fractions will be more challenging due to the range

in size of cells from differentiating squamous epithelium and the potential for exfoliated samples to contain cell clusters. Further refinement of this approach could be envisioned to at least enrich the content of abnormal cells in the separated fractions. Because of the excellent biocompatibility of the custom-made ferrofluids, enriched abnormal cells are kept alive to allow simultaneous staining of diagnostic markers. This in turn will lower the false-negative rates when abnormal cervical cells are a majority proportion of total cells.[149-151] The associated microfluidic system is low-cost and easy-to-operate, only requiring a microchannel, syringe pump and a hand-held permanent magnet. This will minimize cost of expensive infrastructure and training, easing the transition of the system from a research lab to clinical settings.

3.5 Experimental Section

3.5.1 Device Fabrication

The prototype device was fabricated through a standard soft-lithography approach[152] and attached to a flat surface of another piece of polydimethylsiloxane (PDMS). A mask of the device pattern was created using AutoCAD 2013 (Autodesk Inc., San Rafael, CA, USA) and printed by a commercial photo-plotting company (CAD/Art Services Inc, Bandon, OR, USA). Thickness of the device was measured to be 50 μm by a profilometer (Dektak 150, Veeco Instruments Inc., Chadds Ford, PA, USA). Before attachment, PDMS surfaces were treated with plasma (PDC-32G plasma cleaner, Harrick Plasma, Ithaca, NY, USA) with 18 W power for 30 seconds at 11.2 Pa O_2 partial pressure. A NdFeB permanent magnet (Grade N52, K&J Magnetics, Inc., Pipersville, PA, USA) was embedded into PDMS channel with their magnetization direction vertical to the channel during curing stage. The magnet is 2.54 cm in length, 0.635 cm in both width

and thickness. It was placed 1 mm away from the channel. Flux density at the center of magnet's surface was measured to be 450 mT by a Gauss meter (Model 5080, Sypris, Orlando, FL, USA) and an axial probe with 0.381 mm diameter of circular active area. Before liquid injection, the device was treated again with plasma for 10 minutes to render PDMS surfaces hydrophilic. This step ensured both cells and microparticles would not attach onto PDMS surfaces during separation.

3.5.2 Synthesis of Biocompatible Ferrofluids

Maghemite nanoparticles used in the custom-made ferrofluids were synthesized by a chemical co-precipitation method.[131] In a typical protocol, magnetite nanoparticles were precipitated out of aqueous ammonia solution (36 mL, 28% w/w; Sigma-Aldrich, St. Louis, MO, USA) by adding a mixture of 50 mL 0.4 M iron (II) chloride tetrahydrate (Sigma-Aldrich, St. Louis, MO, USA) and 0.8 M iron (III) chloride hexahydrate (Sigma-Aldrich, St. Louis, MO, USA). Nanoparticle suspension was centrifuged at 2500 rpm for 2 minutes; the supernatant was removed, and the precipitate was re-suspended in a solution of 2 M nitric acid and 0.35 M iron (III) nitrate (Sigma-Aldrich, St. Louis, MO, USA). The mixture was then stirred at 90 °C for 25 minutes, as the color of the suspension changed from black (Fe_3O_4) to reddish brown (Fe_2O_3). It was centrifuged again at 2500 rpm for 2 minutes, with its precipitate re-dispersed in de-ionized (DI) water, yielding a stable dispersion. The pH of the dispersion was adjusted to 3.5 by adding 1 M sodium hydroxide solution (Sigma-Aldrich, St. Louis, MO, USA). Afterwards, Atlox 4913 (20 mL, 2.04% w/w; Croda Inc., Edison, NJ), a polymethyl methacrylate-polyethylene glycol (PMMA-PEG) graft copolymer solution, was added to the dispersion and stirred for 5 minutes before raising the pH to 6.8. The mixture was

again stirred for another 1 hour at room temperature, and the resulting ferrofluid was dialyzed against DI water for one week. DI water was refreshed on a daily basis. After dialysis, excess water was vaporized in a convection oven at 90 °C. HBSS (10×, without calcium and magnesium) was added into the ferrofluid (in a volume mixture of 1:9, HBSS: ferrofluid) to render the liquid isotonic for mammalian cells.

3.5.3 Ferrofluid Characterization

Size distribution and morphology of the maghemite nanoparticles were investigated via TEM (FEI Tecnai 20, FEI Co., Eindhoven, Netherlands). Magnetic properties of the ferrofluid were measured at room temperature using a Vibrating Sample Magnetometer (VSM, Model EZ7; MicroSense, LLC, Lowell, MA, USA) with a 2.15 T electromagnet. The magnetic moment of ferrofluid was measured over a range of applied fields from -21.5 to +21.5 kOe. The measurements were conducted in step field mode at a stepsize of 250 Oe s^{-1}.

3.5.4 Cell Handling and Viability Test

Two types of cells were used in experiments, the human HeLa cell line (CCL-2, originally obtained from American Type Culture Collection (ATCC), Manassas, VA, USA) and mouse whole blood cell (C57BL/6, male). HeLa cells, epithelial cells originally derived from a cervical carcinoma, were cultured in flasks containing 12 mL of Dulbecco's Modified Eagle’s Medium (DMEM; Life Technologies, Carlsbad, CA, USA) with 10% v/v Fetal Bovine Serum (FBS; HyClone Laboratories, Inc., Logan, UT, USA), 1% v/v Penicillin-Streptomycin solution (Mediatech, Inc., Manassas, VA, USA) and 1% v/v Antibiotic-Antimycotic (Life Technologies, Carlsbad, CA, USA). They were then incubated (5% CO_2, 90% humidity) in an incubator (Innova Co-170; New Brunswick

Scientific, Enfield, CT, USA) at 37 °C prior to use. HeLa cells were sub-cultured at a ratio of 1:10 every 3 days to maintain them in the exponential growth phase. They were detached from the flask with the treatment of 0.25% (w/v) trypsin–EDTA solution (Life Technologies, Carlsbad, CA, USA) for 5 minutes before harvest. The collected cells were then suspended in the HBSS (without calcium and magnesium; Sigma-Aldrich, St. Louis, MO, USA) at the concentration of 2×10^6 cells mL^{-1} before experiments. Mouse whole blood was obtained from the heart at time of euthanasia into BD Microtainer tubes coated with K_2EDTA (Becton, Dickinson and Company, Franklin Lakes, NJ, USA) according to a protocol approved by the Institutional Animal Care and Use Committee (IACUC) of University of Georgia and stored at 4 °C until use (< 6 h). They were then suspended in the HBSS at the concentration of 2×10^6 cells mL^{-1} before experiments.

The viability of HeLa cells and mouse whole blood cells in HBSS and ferrofluids was determined using Trypan blue exclusion assay. Nominally 2×10^6 cells were centrifuged twice (1200 rpm, 5 minutes for HeLa and 2800 rpm, 10 minutes for blood) at 4°C, washed in HBSS and suspended in either ferrofluids (1 mL) or HBSS (1 mL) as a control. After 2 hours of incubation at room temperature in each fluid, Trypan blue (0.4%; Sigma-Aldrich, St. Louis, MO, USA) was added to cell suspension (10 μL: 10 μL, Trypan blue: cell suspension) and total cells as well as blue staining cells were counted with a hemocytometer. Viability was calculated as percentage of total cells that were not blue. The viability test was repeated three times for each cell type.

3.5.5 Separation Experimental Setup

Ferrofluid and microparticle/cell mixtures injected into microchannel were maintained at tunable flow rates using a syringe pump (NanoJet, Chemyx Inc., Stafford,

TX, USA). Experiments were conducted on the stage of an inverted microscope (Zeiss Axio Observer, Carl Zeiss Inc., Germany). Micrographs of cells and microparticles (Polysciences, Inc., Warrington, PA, USA) were recorded with a high-resolution CCD camera (AxioCam HR, Carl Zeiss Inc., Germany). Phase contrast mode was used to improve the visibility of HeLa and blood cells in the flow during separation. After separation, cell and microparticle samples collected from channel outlets were pipetted onto a hemocytometer and analyzed for cell type distributions in order to quantitatively evaluate efficiency of this approach. ImageJ® software was used to count the number of cells and microparticles. Additionally, cytospins and H&E staining procedure were used to visualize the cell morphologies. Cytospins were made of cell suspensions collected from each outlet using a Cytospin™ 4 Cytocentrifuge (Thermo Scientific, Waltham, MA, USA). Cytospins were then stained with H&E stain using Basofix™ Hematology Reagent System (Wescor, Inc., Logan, UT, USA) in an Aerospray® Hematology Slide Stainer (Wescor, Inc., Logan, UT, USA). Stained cytospins were then examined using a light microscope (Olympus America, Pittsburgh, PA, USA) to compare morphology of cells collected from each outlet.

3.5.6 Data Acquisition

After the microparticles passed through the long separation channel, which allowed sufficient time for magnetic focusing, they experienced a magnetic buoyancy force which leaded to vertical separation. The vertical separation distance, measured at the 3-mm wide section of the channel, is defined as the closest distance between two microparticle streams at the end of the main channel. The magnetic buoyancy force, $\vec{F}_m$,

acting on a non-magnetic microparticle or cell inside ferrofluids, is given by Equation (2.1):

$$\vec{F}_m = -\mu_0 V(\vec{M}_f \cdot \nabla)\vec{H} \tag{2.1}$$

Where V is the volume of the microparticle or cell and μ_0 is the permeability of free space, $\vec{M}_f$ is the effective magnetization of the ferrofluid and $\vec{H}$ is the magnetic field strength. The presence of the minus sign indicates the microparticle or cell is actually pushed away from the region of field maxima. We define recovery rate as the ratio of the number of HeLa cells exiting from Outlets 5 and 6 over the number of HeLa cells in the original sample after magnetic field application, expressed by Equation (2.2):

$$\text{Recovery rate} = \frac{\text{HeLa cells}_{\text{output}}}{\text{HeLa cells}_{\text{input}}} \tag{2.2}$$

The purity is defined as the ratio of separated HeLa cells with respect to the total number of cells exiting Outlets 5 and 6 (Equation (2.3)).

$$\text{Purity} = \frac{\text{HeLa cells}_{\text{output}}}{\text{Total cells}_{\text{output}}} \tag{2.3}$$

Error bars in all figures were expressed as mean±standard deviation.

CHAPTER 4

BIOCOMPATIBLE AND LABEL-FREE SEPARATION OF CANCER CELLS FROM CELL CULTURE LINES FROM WHITE BLOOD CELLS IN FERROFLUIDS [1]

[1] W. Zhao, R. Cheng, S. H. Lim, J. R. Miller, W. Zhang, W. Tang, J. Xie and L. Mao, *Lab Chip*, 2017, **17**, 2243-2255.
Reprinted here with permission of The Royal Society of Chemistry.

4.1 Abstract

This paper reports a biocompatible and label-free cell separation method using ferrofluids that can separate a variety of low-concentration cancer cells from cell culture lines (~100 cancer cells mL^{-1}) from undiluted white blood cells, with a throughput of 1.2 mL h^{-1} and an average separation efficiency of 82.2%. The separation is based on size difference from cancer cells and white blood cells and is conducted in a custom-made biocompatible ferrofluid that retains not only excellent short-term viabilities, but also normal proliferations of 7 commonly used cancer cell lines. A microfluidic device is designed and optimized specifically to shorten the exposure time of live cells in ferrofluids from hours to seconds, by eliminating time-consuming off-chip sample preparation and extraction steps and integrating them on-chip to achieve one-step process. As a proof-of-concept demonstration, a ferrofluid with 0.26% volume fraction was used in this microfluidic device to separate spiked cancer cells from cell lines at a concentration of ~100 cells mL^{-1} from white blood cells with a 1.2 mL h^{-1} throughput. The separation efficiencies were 80±3%, 81±5%, 82±5%, 82±4%, and 86±6% for A549 lung cancer, H1299 lung cancer, MCF-7 breast cancer, MDA-MB-231 breast cancer, and PC-3 prostate cancer cell lines, respectively. Separated cancer cells purity was between 25.3% and 28.8%. In addition, separated cancer cells from this strategy showed an average short-term viability of 94.4±1.3% and separated cells were cultured and demonstrated normal proliferation to the confluence even after the separation process. Owning to its excellent biocompatibility and label-free operation, and its ability to recover low concentration of cancer cells from white blood cells, this method could lead to a promising tool for rare cell separation.

4.2 Introduction

Microfluidic manipulation of cells in magnetic liquids,[153] i.e., negative magnetophoresis, led to a number of recent applications in cell separation,[38, 41, 93, 153] trapping and focusing,[31, 45, 100, 128] and density measurements.[56, 61, 62, 123, 154] Its working principle is as follows: cells without any labels placed inside a uniformly magnetic media – magnetic liquids, act as "magnetic holes".[43] A magnetic field gradient attracts the magnetic media, which causes the "magnetic holes" – cells, to be preferentially pushed away. This way, cells can be continuously manipulated in a label-free fashion. Magnetic force acting on the cells is proportional to their sizes,[27, 153] very similar to buoyancy force, which allows for a size-based manipulation. Typical devices for conducting "negative magnetophoresis" assays are simple and low-cost, involving only channels and permanent magnets. Their operation does not necessitate accessories such as power supplies or function generators. Because of its label-free, low-cost and simple-to-use nature, "negative magnetophoresis" has been used recently for cell manipulation. For example, Demirci group developed a static-flow system with a form of magnetic liquids – paramagnetic salt solutions – to precisely measure subtle density differences among cell groups.[56, 61] Salt solutions containing transition and lanthanide metals, such as Mn^{2+} or Gd^{3+}, are weakly magnetic due to their unpaired inner-shell electrons that produce a magnetic moment. Our group demonstrated a continuous-flow ferrohydrodynamic separation of HeLa cells from whole blood in another form of magnetic liquids – ferrofluids.[95] Ferrofluids are colloidal suspensions of magnetic nanoparticles with diameters of approximately 10 nm. Although both paramagnetic salt solution and ferrofluid have served as the medium in "negative magnetophoresis" assays, ferrofluids

were considered to be better suited for applications such as high-throughput separation that requires a continuous flow, because of their stronger magnetic properties, while paramagnetic salt solutions exceled in static-flow applications such as density measurement.

Cell separation based on "negative magnetophoresis" in ferrofluids is facing its own challenges, especially in rare cell separation where cell integrity needs to be maintained for further analysis, while typically less than 1000 cells in one milliliter of sample are available and need to be enriched in a high-throughput and high-efficiency manner.[155] The challenges associated with cell separation in ferrofluids are three-fold. First of all, ferrofluids are not natural media for cells; they need to be rendered biocompatible so that cells remain alive and their normal functions are kept intact during and after the separation for post-separation analysis. This is not trivial, although progresses were made recently through preserving viability and normal proliferation of cells in custom-made ferrofluids,[38, 39] biocompatibility of ferrofluids remains to be a significant challenge for cell separation applications. For examples, although Yellen's group developed a bovine serum albumin (BSA) coated ferrofluid in which human umbilical vein endothelia cells (HUVEC) had more than 95% viability after 2 hours of exposure and were able to maintain normal proliferation afterwards,[39] this ferrofluid was only used in static-flow conditions for relatively slow cell manipulation, its colloidal stability could be an issue in high-throughput and continuous-flow cell separation applications, because of the thick BSA surfactant layer used for particle functionalization. Although Koser's group reported a citrate-stabilized ferrofluid and demonstrated a 75% viability of blood cells in them after several hours' exposure,[38] long-term cell

proliferation study in this ferrofluid was not conducted. In summary, only a very limited number of cells were studied in these custom-made ferrofluids in operation conditions that were not always compatible for continuous-flow cell separation, and data didn't often provide both short-term and long-term impacts on them after separation. As a result, there is an urgent need for a new ferrofluid that can minimize its negative effects on mammalian cells, at the same time is colloidally stable for high-throughput and continuous-flow operation under strong magnetic fields. The second challenge comes from device design for cell separation in ferrofluids. Even with a biocompatible ferrofluid, it is still necessary to reduce the exposure time of cells in them down to an absolute minimum, because prolonged exposure time will inevitably lead to particle endocytosis and/or diffusion and affect cell viability and normal functions.[156] For example, we observed in this study that long exposure time of A549 lung cancer cells in ferrofluids resulted in a higher cellular uptake of nanoparticles and slower cell growth. In previous publications, the majority of cell exposure time to ferrofluids came from sample preparation and sample extraction that could last up to hours.[38, 44, 95] As a result, a new one-step device design that integrates sample preparation and extraction on chip could significantly reduce exposure time and improve overall biocompatibility of the assay. The third challenge is associated with the low concentration of target cells in rare cell separation. In order to capture a meaningful number of target cells, throughput of at least 1 mL h^{-1} and separation efficiency of at least 80% in low concentration (<1000 cell mL^{-1}) conditions are necessary.[157] Although cell separation in ferrofluids was demonstrated before, they mostly focused on the separation of bacteria and yeast cells,[44, 93] bacteria and red blood cells,[38] and HeLa cells and mouse blood.[95] The throughputs of these studies

were relatively low, and the target cells were at a much higher concentration (*e.g.*, 10^5-10^6 cells mL^{-1}) than the definition of rare cells. It is therefore necessary to systematically optimize the device and ferrofluid design so that the throughput and efficiency of separation are comparable to those needed for rare cell separation.

In this study, we addressed the above-mentioned three challenges associated with rare cell separation in ferrofluids, by demonstrating a label-free separation of low-concentration cancer cells from cell culture lines at a concentration of ~100 cancer cells mL^{-1} from undiluted white blood cells at a concentration of ~10^6 cells mL^{-1} in a newly developed biocompatible ferrofluids, with an optimized device design that achieved a throughput of 1.2 mL h^{-1} and a separation efficiency of greater than 80%. Cells were only exposed to ferrofluids for seconds in this process. We first developed a new water-based ferrofluid in which 7 commonly used cancer cell lines showed excellent short-term viability and normal proliferation to confluence after extended exposures. The ferrofluid possessed ideal properties including its pH value, tonicity, materials and surfactants of nanoparticles, as a biocompatible medium for mammalian cells, while at the same time the overall colloidal stability of this ferrofluid was well maintained to allow for high-throughput and continuous-flow separation under strong magnetic fields. We further developed a new device design that significantly reduces the exposure time of cells in ferrofluids, from hours to seconds, by taking advantage of the laminar flow nature of liquids in microchannels.[158, 159] The design is explained in detail in Figure 4.1. Briefly, in a frequently used setup of ferrohydrodynamic cell separation,[38, 44, 93, 95] the majority of ferrofluid exposure time came from sample preparation (*e.g.*, off-chip pre-mixing between ferrofluids and cells) and sample extraction (*e.g.*, off-chip washing of cells after

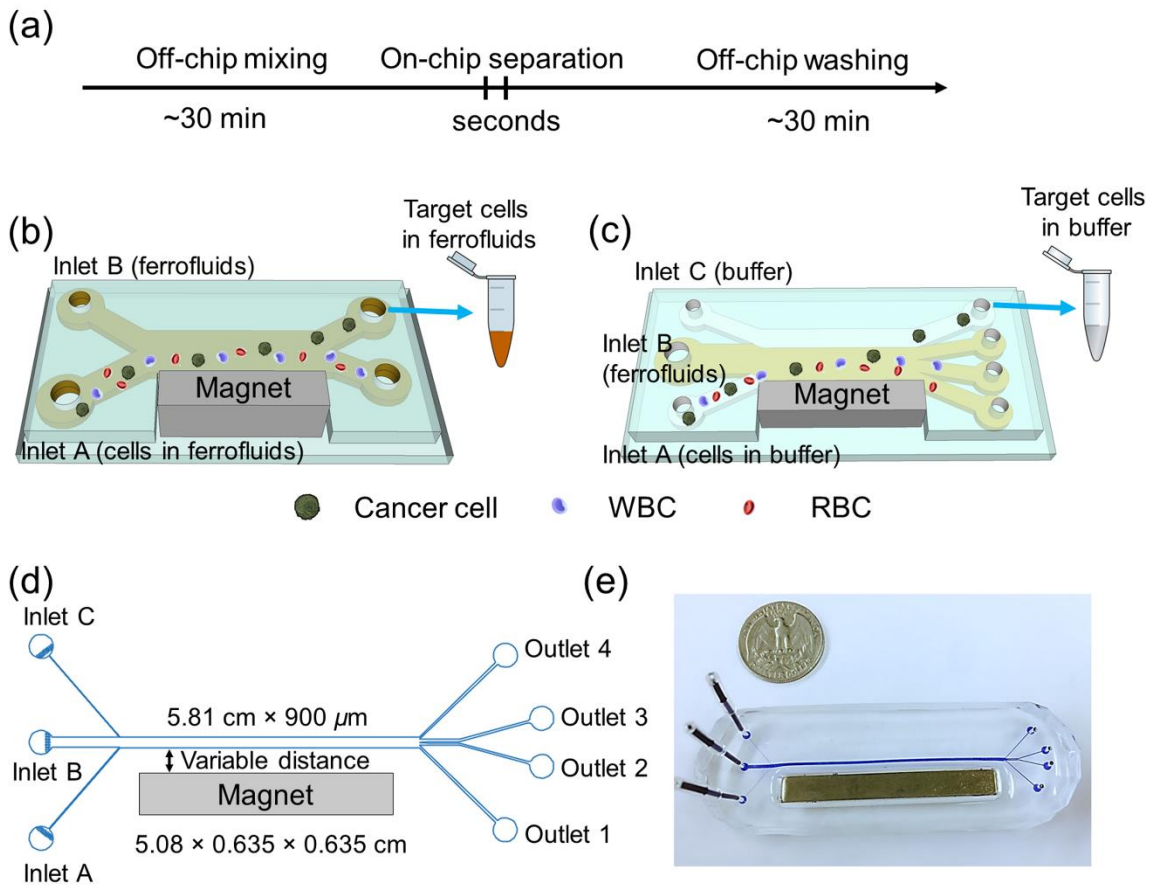

Figure 4.1: Device illustrations. (a) Processing time of existing cell separation in ferrofluids involves time-consuming pre-mixing of cells with ferrofluids (~30 minutes) and off-chip washing steps (~30 minutes), while separation takes place within seconds. Total exposure time of cells in ferrofluids is estimated to be 1-2 hours. (b) Schematic illustration of an existing cell separation device. Cell mixtures are mixed with ferrofluids before separation and target cells are still in contact with ferrofluids after separation. (c) Schematic illustration of the proposed biocompatible cell separation in ferrofluids. Cell sample, ferrofluid, and buffer are injected into the device without pre-mixing. Cells are only in contact with ferrofluids when they are separated from each other. After separation, larger cancer cells are extracted into the buffer stream, eliminating the washing step. Total exposure time of cells to ferrofluids is estimated to be seconds. (d) Top-view of the proposed device, which consists of a microchannel and a permanent magnet, their relevant dimensions, and labeling of inlets and outlets. (e) A photo of the prototype device with a U.S. quarter for size comparison. Blue dye is used to visualize the channel.

separation), as shown in Figures 4.1a and b. However, the only time that cells needed to be exposed to ferrofluids was when they were actually being separated from each other.

As a result, a device design that incorporates both on-chip sample preparation and extraction could significantly reduce exposure time and improve overall biocompatibility of the assay. In this device design, cell samples, ferrofluids, and a buffer were injected into a main channel through individual inlets, as shown in Figure 4.1c. When they combined in the main channel, cell samples are mixed with the ferrofluid almost instantaneously because of strong magnetic convection,[160, 161] and then separated based on their size difference. Large cells moved across the ferrofluid layer with a faster velocity than smaller ones. Towards the end of the channel, larger cells reached the ferrofluid/buffer boundary and were extracted into the buffer stream containing extremely low concentration of nanoparticles diffused from the ferrofluid stream. This way, cells were only exposed to ferrofluids when necessary (i.e., separation) and the exposure time was determined by the flow rate and channel length, which in this design was on the order of seconds. Finally, we performed a systematic parametric study of key factors influencing the performance of this separation method and determined parameters for high-throughput and high efficiency low-concentration cancer cell separation of cell culture lines from undiluted white blood cells.

4.3 Experimental Section

4.3.1 Synthesis and Characterization of Biocompatible Ferrofluids

Ammonium hydroxide solution (NH_4OH, 28% w/w), iron (II) chloride tetrahydrate ($FeCl_2 \cdot 4H_2O$), iron (III) chloride hexahydrate ($FeCl_3 \cdot 6H_2O$), nitric acid (HNO_3), iron (III) nitrate nonahydrate ($Fe(NO_3)_3 \cdot 9H_2O$), and sodium hydroxide (NaOH) were purchased from a commercial vendor (Sigma-Aldrich, St. Louis, MO). All reagents were used as received. Maghemite nanoparticles were synthesized by a chemical co-

precipitation method.[95, 131] In a typical reaction, 50 mL of ammonium hydroxide solution was quickly added to a mixture of 100 mL of 0.4 M iron (II) chloride tetrahydrate and 0.8 M iron (III) chloride hexahydrate and was followed by stirring at room temperature for 30 minutes. The suspension was then centrifuged at 2000×g for 3 minutes and the precipitate was dispersed in 200 mL of 2 M nitric acid and 0.35 M iron (III) nitrate nonahydrate. The mixture was maintained at 90 °C for 1 hour. During this time, the color of the mixture changed from black (Fe_3O_4) to reddish brown (Fe_2O_3). The maghemite nanoparticle suspension was centrifuged at 3000×g for 3 minutes and finally dispersed in 120 mL of deionized (DI) water, yielding a stable dispersion with a pH of 1.5-2. The pH of the dispersion was adjusted to 2.9 by 1 M sodium hydroxide solution. 40 mL of Atlox 4913 (Croda, Inc., Edison, NJ), a graft copolymer solution, was added to the dispersion and stirred for 5 minutes before raising pH to 7.0. The dispersion was then vigorously stirred at room temperature for 1 hour, and the resulted ferrofluid was dialyzed with a dialysis membrane (Spectrum Labs Inc., Rancho Dominguez, CA) against DI water for one week. DI water was refreshed every 24 hours. After dialysis, excess water was vaporized at 72 °C. Finally, 10% (v/v) 10× Hank's balanced salt solution (HBSS; Life Technologies, Carlsbad, CA) was added into the ferrofluid to render it isotonic for cells followed by adjusting pH to 7.0. Sterile filtration of ferrofluid was performed with a 0.2 μm filter (VWR, Radnor, PA) and the ferrofluid was exposed to UV light for 12 hours before experimental use.

Size and morphology of maghemite nanoparticles were characterized via transmission electron microscopy (TEM; FEI Corp., Eindhoven, the Netherlands). Magnetic properties of the ferrofluid were measured at room temperature using a

vibrating sample magnetometer (VSM; MicroSense, LLC, Lowell, MA) with a 2.15 T electromagnet. The magnetic moment of ferrofluid was measured over a range of applied fields from -21.5 to +21.5 kOe. The measurements were conducted in step field mode at a stepsize of 250 Oe s^{-1}. Zeta potential of the ferrofluid was measured with a Zetasizer Nano ZS (Malvern Instruments Inc., Westborough, MA).

4.3.2 Cell Cultures and Sample Preparation

7 cancer cell lines (ATCC, Manassas, VA) including two lung cancer cell lines (A549 and H1299), three breast cancer cell lines (HCC1806, MDA-MD-231 and MCF-7), one cervical cancer cell line (HeLa), and one prostate cancer cell line (PC-3) were used to characterize biocompatibility of the ferrofluid. A549, H1299, HCC1806, and PC-3 cells were cultured in RPMI-1640 medium (Mediatech, Inc., Manassas, VA) supplemented with 10% (v/v) fetal bovine serum (FBS; Life Technologies, Carlsbad, CA) and 1% (v/v) penicillin/streptomycin solution (Mediatech, Inc., Manassas, VA) at 37 °C under a humidified atmosphere of 5% CO_2. HeLa cells were cultured in Dulbecco's modified eagle medium (DMEM; Life Technologies, Carlsbad, CA) supplemented with 10% (v/v) FBS and 1% (v/v) penicillin/streptomycin solution at 37 °C under a humidified atmosphere of 5% CO_2. MDA-MB-231 and MCF-7 cells were cultured in DMEM supplemented with 10% (v/v) FBS, 1% (v/v) penicillin/streptomycin solution and 0.1 mm non-essential amino acid (NEAA; Life Technologies, Carlsbad, CA). All cell lines were released through incubation with 0.05% Trypsin-EDTA solution (Life Technologies, Carlsbad, CA) at 37 °C for 5-10 minutes.

A549, H1299, MCF-7, MDA-MB-231, and PC-3 cells were not only used in ferrofluid's biocompatibility characterization but also used in cell separation experiments.

Therefore, these five cell lines were stained with 2 μM CellTracker Green (Life Technologies, Carlsbad, CA) at 37 °C for 30 minutes before separation. The resulting cell suspensions were then centrifuged at 200 ×*g* for 5 minutes and suspended in phosphate buffered saline (PBS; Life Technologies, Carlsbad, CA) with 2% (v/v) FBS before use. For a validation experiment of the simulation on cancer cells from cell culture lines and red blood cells (RBCs) separation, human whole blood (Streck, Omaha, NE) was diluted 1000 times by PBS to achieve the concentration of 2×10^6 cells mL^{-1}. For low-concentration cancer cells of cell culture lines separation from undiluted white blood cells (WBCs), WBCs were obtained from undiluted human whole blood (Zen-Bio, Research Triangle Park, NC) with its RBCs lysed by RBC lysis buffer (eBioscience, San Diego, CA). The concentration of WBCs was on the order of 10^6 cells mL^{-1}. 100 CellTracker Green pre-stained cancer cells were spiked into 1 mL of either diluted whole blood or undiluted WBCs. Cancer cells were first counted with a hemacytometer (Hausser Scientific, Horsham, PA) and serially diluted in culture medium to achieve a solution with approximately 1×10^4 cells mL^{-1}. Cells were then counted with a Nageotte counting chamber (Hausser Scientific, Horsham, PA) to determine the number of cells per μL. 100 cells (~10 μL) were spiked into 1 mL of WBCs. The number of cells spiked was determined by the average of two counts, with less than 5% difference between the counts.

4.3.3 Characterizations of Cell Biocompatibility After Exposures to Ferrofluids

Cell viability was evaluated by 3-(4,5-dimethylthiazol-2-yl)-2,5-diphenyl-tetrazolium bromide (MTT) assay. A549 cells were first incubated in each well of a 96-well plate (Corning Inc., Corning, NY) for a total of 24 hours. Ferrofluids of varying

concentrations (0.05%, 0.19%, 0.22%, and 0.26% v/v) were added to the plate. After incubation for 12 hours, ferrofluid and medium were removed, and cells were washed three times with PBS. MTT (ATCC, Manassas, MA) assay was then performed to determine the cell viability following the manufacture's recommended protocol. Cell viability of the other 6 cell lines was investigated by the same MTT assay with a 0.26% (v/v) ferrofluid after 2 hours' incubation.

Cell proliferation rate was assessed by MTT assay, too. A549 cells were first incubated with ferrofluids (0.26% v/v) for 1 minute and 2 hours, respectively at 37 ºC under a humidified atmosphere of 5% CO_2. Cells were then washed three times with PBS and released through incubation with 0.05% Trypsin-EDTA solution. 4000 cells were seeded in each well of a 96-well plate. MTT assay was performed every 24 hours to determine the growth rate following the manufacture's recommended protocol. The medium was changed on the third day. The proliferation of other 6 cancer cell lines was investigated by attempting to culture cells to confluence after exposing them to ferrofluids for 2 hours.

4.3.4 Characterizations of Cell Biocompatibility After Cell Separation Experiments

Short-term viability after separation was examined using a Live/Dead assay (Life Technologies, Carlsbad, CA). 1×10^6 A549 cells were injected through inlet A at a flow rate of 20 μL/min. After separation, cells from outlet 4 were collected and incubated with a working solution (2 μm calcein-AM and 4 μm propidium iodide (PI)) for 30 minutes at room temperature. After the solution was removed and washed with PBS, the labeled cells were observed under a fluorescence microscope (Carl Zeiss, Inc., Germany) for counting. For long-term proliferation, the separated A549 cells were collected into a

centrifuge tube and spun down to remove the buffer, and then the cells were suspended in complete culture medium and seeded into a 24-well plate (Corning Inc., Corning, NY). Cells were then cultured at 37 °C under a humidified atmosphere of 5% CO_2, the medium was refreshed every 24 h during the first 3 days. Cellular morphology was inspected every 24 hours.

4.3.5 Cellular Nanoparticle Uptake

Nanoparticle uptake study was conducted with A549 lung cancer cells. 1×10^5 A549 cells were seeded in each well of a 4-well chamber slide (Thermo Fisher Scientific, Waltham, MA). After 24-hour incubation, ferrofluids were added and incubated with cells at 37 °C for 1 minute and 2 hours, respectively. The ferrofluids were then removed and cells were washed three times with PBS. Next, cells were fixed with ice-cold 95% ethanol (Thermo Fisher Scientific, Waltham, MA) for 15 minutes. Subsequently, cells were incubated with Prussian blue staining solution (a mixture of equal volume of 1.2 mM hydrochloric acid and 4% w/v potassium ferrocyanide solution; Sigma-Aldrich, St. Louis, MO) for 15 minutes at room temperature. Cells were then rinsed with DI water and counterstained with pararosaniline solution (Sigma-Aldrich, St. Louis, MO) for 10 minutes. After consecutive dehydrations with 70%, 90%, and 100% ethanol, the chamber was removed, and the slide was mounted. The slide was then examined using a light microscope (Carl Zeiss, Inc., Germany).

4.3.6 Device Fabrication and Experimental Setup

Microfluidic devices were made of polydimethylsiloxane (PDMS) using standard soft lithography techniques.[95, 162] The thickness of the microfluidic channel was measured to be 52 μm by a profilometer (Veeco Instruments, Inc., Chadds Ford, PA). A NdFeB

permanent magnet (K&J Magnetics, Inc., Pipersville, PA) was embedded into the PDMS channel with their magnetization direction vertical to the channel during the curing stage. The magnet is 5.08 cm in length, 0.635 cm in both width and thickness. Device and magnet dimensions are depicted in Figure 4.1d, and a photo of the system is shown in Figure 4.1e. Flux density at the center of magnet's surface was measured to be 390 mT by a Gauss meter (Sypris, Orlando, FL) and an axial probe with 0.381 mm diameter of circular active area. The fabricated devices were flushed by 70% ethanol (Decon Labs, Inc., King of Prussia, PA) for 10 minutes before use. During a typical experiment, a microfluidic device was placed on the stage of an inverted microscope (Carl Zeiss, Inc., Germany) for observation and recording. Three fluids were controlled by individual syringe pumps (Chemyx, Inc., Stafford, TX) with tunable flow rates. Cell samples, ferrofluids, and PBS containing 2% (v/v) FBS were injected into the device through different inlets. Images and videos of microparticles and cells were recorded with a high-resolution CCD camera (Carl Zeiss, Inc., Germany).

Polystyrene microparticles (Polysciences, Inc., Warminster, PA) with diameters of 15.7 μm and 5.8 μm were prepared in PBS at the concentration of 2×10^6 particles mL^{-1} for device calibration. Microparticle mixtures were injected into inlet A with a flow rate of 0.5-8 μL min^{-1}. The flow rate of inlet B was fixed at 5 μL min^{-1} for all experiments, and flow rate of inlet C (3.5-7 μL min^{-1}) was adjusted accordingly to make the ferrofluid/buffer boundary just right below the outlet 4, to allow for particle and cell extraction. The magnet was placed 1, 4 and 7 mm away from the channel, which corresponded to magnetic field strengths 300, 134, 72 mT, and magnetic field gradients

83.4, 32.2, 12.9 T m^{-1} (Figure 4.2). Ferrofluid concentrations of 0.13, 0.26 and 0.39% (v/v) were used.

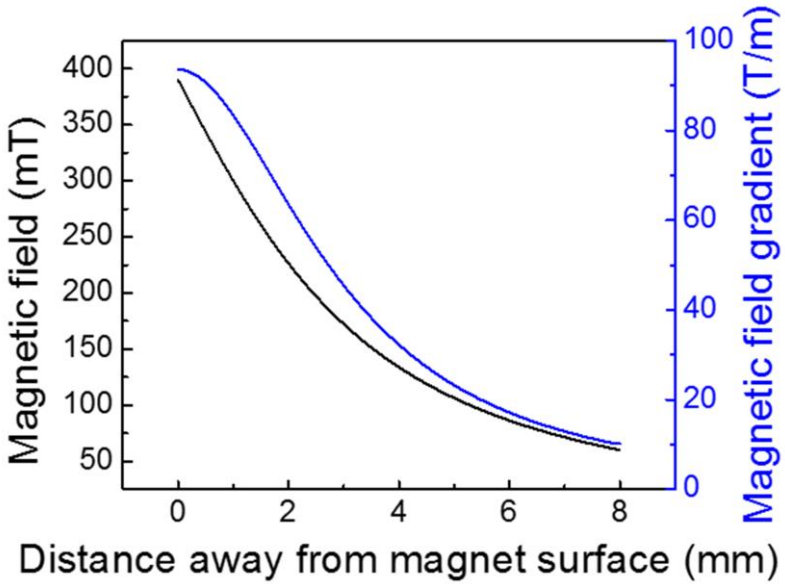

Figure 4.2: Measured magnetic field and its gradient of the center of magnet's surface vs. distance away from the surface.

For cancer cells of cell lines/RBCs and cancer cells of cell lines/WBCs separation experiments, cell mixtures were injected into inlet A at the flow rate of 20 μL min^{-1}. The magnet was placed 4 mm away from the channel and ferrofluids with a concentration of 0.26% (v/v) was used. After separation, cells from outlet 4 were collected into a 96-well plate for counting under a fluorescence microscope.

4.3.7 Simulation

Cell trajectories were simulated in three-dimensional (3D) manner by modifying previously developed models with a concentration profile of ferrofluids across the width of the microchannel.[46, 110] Briefly, we used an analytical model that could predict the 3D transport of diamagnetic cells in ferrofluids inside a microfluidic channel coupled with

permanent magnets. The magnets produced a spatially non-uniform magnetic field that led to a magnetic buoyancy force on the cells. Resulting trajectories of the cells were obtained by (1) calculating the 3D magnetic buoyancy force via an experimentally verified and analytical distribution of magnetic fields as well as their gradients, together with a nonlinear magnetization model of the ferrofluid, (2) deriving the hydrodynamic viscous drag force with an analytical velocity profile in the channel including "wall effect", (3) solving governing equations of motion using analytical expressions of magnetic buoyancy force and hydrodynamic viscous drag force. The parameters of simulation (device dimension and geometry, fluid and cell properties, and magnetic fields) reflected exact experimental conditions.

4.4 Results and Discussion

4.4.1 Ferrofluid Properties

Figure 4.3a shows size distribution and a sample TEM image of maghemite nanoparticles of the custom-made ferrofluid. The particles had a mean diameter of 11.24 nm with a standard deviation of 2.52 nm. Although nanoparticles with larger diameters were considered to be more biocompatible because they may inhibit direct diffusion across cell membrane,[134-137] we chose this diameter for the nanoparticles to preserve the colloidal stability of ferrofluids against agglomeration due to gravitational settling and magnetic dipole-dipole attraction.[27] Particles with a large diameter are prone to settling and agglomeration, and can disrupt continuous-flow separation. However, at a diameter of ~10 nm, thermal agitation at room temperature is sufficient to keep particles separated. As a result, our ferrofluids remained colloidally stable after at least 10 months' storage. The nanoparticles were also functionalized with a graft copolymer as surfactants to

prevent them from coming too close to one another when there was a magnetic field. In all of the cell manipulation experiments conducted here, our ferrofluids did not show any sign of nanoparticle agglomeration under magnetic fields. We measured the saturation magnetization of the as-synthesized ferrofluid to be 0.96 kA m^{-1}, as shown in Figure 4.3b. Considering the bulk magnetization of maghemite is about 370 kA m^{-1},[133] we estimated the volume fraction of the magnetic content of the ferrofluid to be 0.26%. The low volume fraction of the ferrofluid not only led to good biocompatibility for live cells, but also enabled us to observe cell motion in microchannel directly with bright-field microscopy, which was difficult with opaque ferrofluids of high solid volume fractions. The surface charge of the particles was negative, measured by zeta potential of -27.2±11.4 mV. The ferrofluid was made to be isotonic and its pH was adjusted to 7.0 for biocompatible cell manipulation.

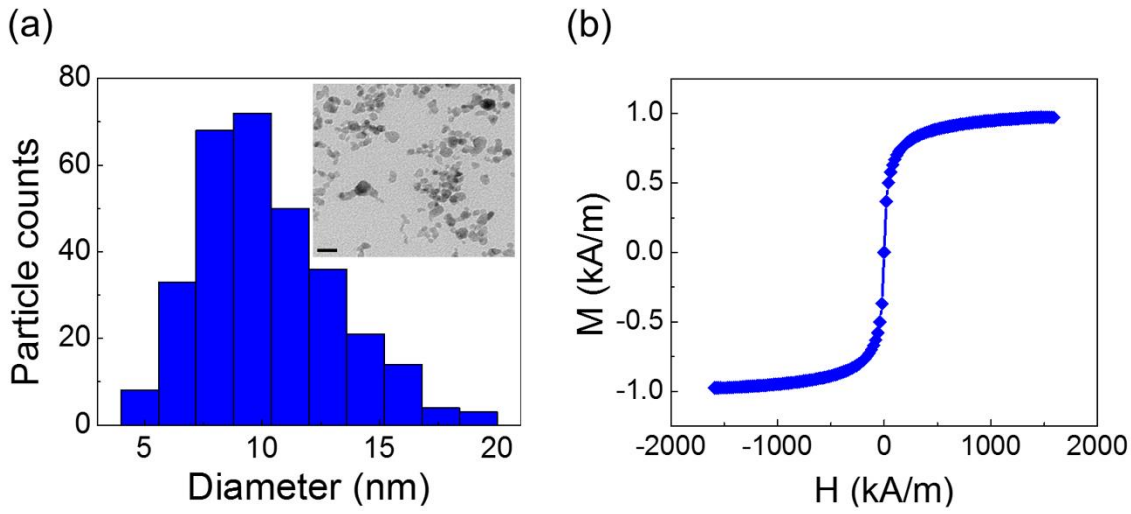

Figure 4.3: Ferrofluid characterizations. (a) Size distribution of the maghemite nanoparticles within the ferrofluid (11.24±2.52 nm). Inset: a TEM image of the maghemite nanoparticles in the ferrofluid. Scale bar: 20 nm. (b) Magnetization curve of the ferrofluid. The saturation magnetization of this ferrofluid is 0.96 kA m^{-1}, corresponding to a 0.26% volume fraction of magnetic materials.

4.4.2 Ferrofluid Biocompatibility

We investigated the biocompatibility of this ferrofluid by exposing a total of 7 cancer cell lines to it, and studying their short-term viability, long-term cell proliferation, and cellular nanoparticle uptake after the exposure. These cell lines included two lung cancer cell lines (A549 and H1299), three breast cancer cell lines (HCC1806, MDA-MB-231 and MCF-7), one prostate cancer cell line (PC3), and one cervical cancer cell line (HeLa). We chose these cell lines because they were frequently used to validate new microfluidic separation technologies for cancer cells.

Short-term cell viability was examined using MTT assay. Here we use the A549 lung cancer cell line as an example to describe the results. Figure 4.4a compares A549 cell viabilities after 12-hour exposures to control medium and 4 different concentrations (0.05%, 0.19%, 0.22%, and 0.26% v/v) of custom-made ferrofluids. A549 cells showed 100±3% viability in the control medium, and gradually decreasing viabilities in ferrofluids (91±3% viability for 0.05% ferrofluid, 86±4% viability for 0.19% ferrofluid, 83±4% viability for 0.22% ferrofluid, and 83±3% viability for 0.26% ferrofluid). This is expected as the nanoparticle concentration does affect the short-term cell viability, due to either particle diffusion across cellular membrane or endocytosis of particles by cells. Still, A549 cells retained 83±3% viability in a 0.26% concentration ferrofluid after a 12-hour period of exposure, which was at least 6 times longer than current cell viability studies in custom-made ferrofluids.[38, 39, 95] Such a long period of exposure is typically not necessary for high-throughput cell separation; and a more reasonable estimated time of ferrofluid exposure for current cell separation schemes is 1-2 hours. Within such a time frame, Table 4.1 summarizes the results of all 7 cell lines, which showed consistently

over 90% viability after 2-hour exposure in a 0.26% ferrofluid. They confirmed that this ferrofluid possessed minimal detrimental effect on 7 cancer cell lines in the short term.

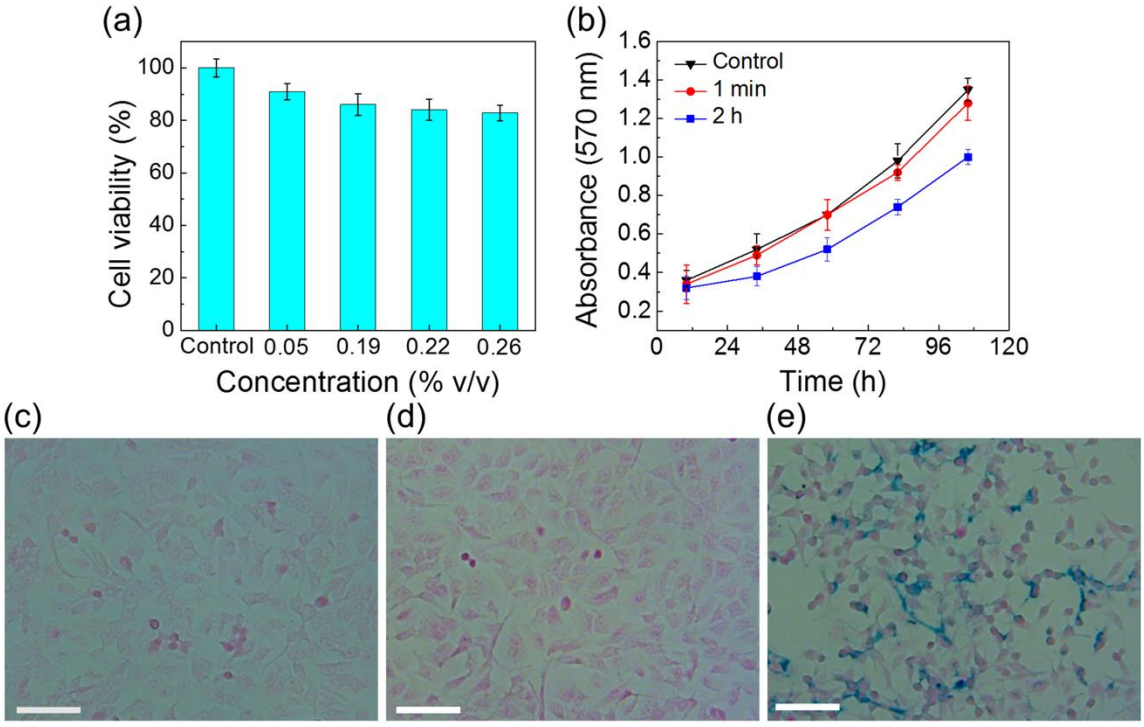

Figure 4.4: Cell viability and proliferation study. (a) Cell viability of A549 cells was evaluated by MTT assay. Different concentrations of ferrofluids (0.05%, 0.19%, 0.22%, and 0.26% v/v) were added in the incubation medium. Average cell viabilities were 100% in the control, 91% in 0.05% ferrofluid, 86% in 0.19% ferrofluid, 84% in 0.22% ferrofluid, and 83% in 0.26% ferrofluid, after a 12-hour incubation with ferrofluids. (b) Growth curves of A549 cells with different exposure times to ferrofluids were determined by MTT assay. Cells incubated with ferrofluids for 2 h grew more slowly than the control group. No significant difference was found between cells incubated with ferrofluid for 1 min and the control group. (c-e) Cellular nanoparticle uptake of A549 cells. The cells were incubated with ferrofluid for 0, 1 min, and 2 h and then subjected to Prussian blue staining. Positive staining was visible in the majority of the cells that were incubated with ferrofluid for 2 h (e). 1 min incubation with ferrofluid showed little cellular uptake of nanoparticles (d). (c) Control. Scale bars: 50 μm.

In addition to short-term viability, we also examined whether all cell lines were able to proliferate normally after ferrofluid exposures. As shown in Table 4.1, all 7 cell

lines were capable of normal proliferation to confluence after 2-hour incubation in the ferrofluid. This is the first time that long-term effects of a colloidally stable ferrofluid were studied on several cancer cell lines. To the best of our knowledge, Yellen's group conducted the only proliferation study using HUVEC after exposures to a bovine serum albumin coated ferrofluid.[39]

Table 4.1: Short-term viability and long-term proliferation of 7 cancer cell lines after exposures to the custom-made biocompatible ferrofluid. Short-term viability was determined by a Live/Dead assay after 2-hour exposure to the ferrofluid with a 0.26% volume fraction ferrofluid. Long-term proliferation was determined by culturing cells after the same exposure to the ferrofluid.

Cell line	A549 (Lung cancer)	H1299 (Lung cancer)	HeLa (Cervical cancer)	MDA-MB-231 (Breast cancer)	HCC1806 (Breast cancer)	MCF-7 (Breast cancer)	PC3 (Prostate cancer)
Viability after 2-hour exposure to ferrofluids	94%	95%	92%	95%	94%	95%	96%
Proliferation to confluence after 2-hour exposure to ferrofluids	Yes	Yes	Yes	Yes	Yes	Yes	Yes

Our ferrofluids showed excellent short-term and long-term biocompatibility for 7 types of cancer cells. As discussed earlier, even with such a ferrofluid, it is still better to minimize cells' exposure time to it, as prolonged exposure time will inevitably lead to particle endocytosis and/or diffusion, which may affect cells' normal functions. To investigate the effect of exposure time on cell proliferation, we examined A549 cells again using both MTT assay for proliferation and Prussian blue assay for nanoparticle uptake. This time, A549 cells were either seeded directly into a 96-well plate as a control or incubated in ferrofluids for 1-minute and 2-hour. Their proliferation measurements (absorbance at 570 nm of MTT assay) was evaluated and recorded every 24-hour, and

their nanoparticle uptake (iron distribution) were imaged after incubation with ferrofluids using Prussian blue assay. Figure 4.4b compares cell proliferations between control, 1-minute exposure, and 2-hour exposure to ferrofluids. No significant change was found between the control and 1-minute exposure; cells incubated in ferrofluids for 1-minute were able to proliferate normally and resulted in nearly the same growth rate as the control. This was also confirmed by nanoparticle uptake comparison in Figures 4.4c and d, which showed almost identical and little iron presence. On the other hand, 2-hour exposure to ferrofluids did affect A549 cell proliferation in a noticeable and negative way, evidenced by a lower growth rate in Figure 4.4b, and a significant iron presence in Figure 4.4e. The longer exposure time of A549 cells in ferrofluids led to the higher cellular uptake of nanoparticles and slower cell growth. It is therefore beneficial to minimize the exposure time of cells to ferrofluids.

4.4.3 Device Optimization and Calibration

We described previously the general idea behind the device design to significantly decrease the exposure time of cells to ferrofluids. Briefly, we aimed to eliminate unnecessary exposure time including sample preparation and sample extraction and allow cells to be in contact with ferrofluids when it was absolutely necessary (*e.g.*, separation). The flow rate and channel length determined the exposure time in a typical cell separation protocol, which was estimated to be on the order of seconds in our devices. Here we described the results of device optimization and calibration using analytical models and microparticles. This optimization was also verified by a separation experiment of cancer cells of cell culture lines and red blood cells.

We used the 3D analytical model to optimize our device (Figure 4.1d) for a potential cell separation application. In this case, we allowed two groups of cells with different sizes to enter the channel and simulated their trajectories. Sample simulated trajectories of two types of cells (cancer cells with a presumed 15.7 μm diameter, and red blood cells with a presumed 5.8 μm diameter) are shown in Figure 4.5a. Location of the simulation window is depicted in Figure 4.5b. We chose these two cells' sizes for simulation because microparticles with exact sizes were available for calibration purposes. From these trajectories, we calculated two outputs – a deflection in the *y*-direction for the larger cancer cells, denoted as Y_2, and a separation distance between two types of cells, denoted as ΔY. Both outputs were optimized using parameters including channel length (4-8 cm), magnetic fields and gradients (field: 72-300 mT; gradient: 12.9-83.4 T m^{-1}), flow rates of cell inlet (inlet A in Figure 4.1c, 0.5-20 μL min^{-1}), and ferrofluid concentrations (0.13-0.39% v/v). The goal was to achieve separation of larger cancer cells from smaller blood cells, which translated to maximizing both Y_2 and ΔY simultaneously. Calibration of the device used two types of microparticles with diameters of 5.8 μm and 15.7 μm. Experimental conditions for the calibration including magnetic fields, flow rates, and ferrofluid concentrations were the same as in simulation. A sample image of the microparticles' trajectories at the outlets is shown in Figure 4.5c. We extracted both outputs (Y_2 and ΔY) from the images and used them to compare simulation and calibration results. Location of the experimental observation window is depicted in Figure 4.5b. In this device design, cell samples from inlet A were quickly mixed with ferrofluids from inlet B because of a strong magnetic convection resulted from interactions between the ferrofluids and permanent magnet.[160, 161, 163] With typical

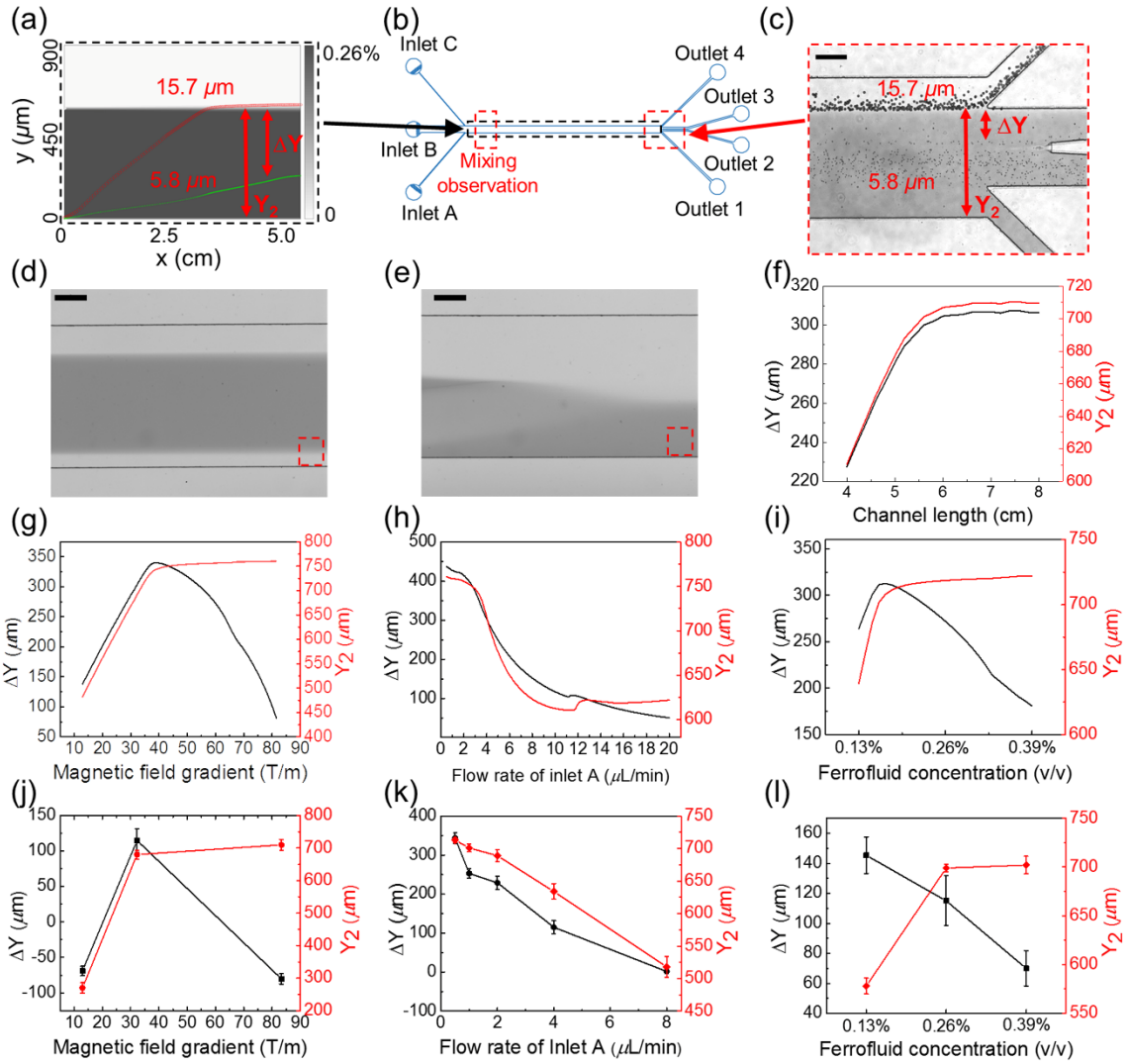

Figure 4.5: Device optimization via simulations and calibrations. (a) Simulated concentration profile of ferrofluids and the cells' trajectories across ferrofluids and the buffer stream. The ferrofluid concentration is represented by gray scale. The trajectories of a cancer cell with 15.7 μm diameter are indicated by red circles, and trajectories of a red blood cell with 5.8 μm diameter are indicated by green circles. (b) Schematic of the microchannel with various simulation and observation windows. (c) A representative image of microparticle separation observed in the window from (b). Representative images of magnetic convective mixing (without microparticles) from the observation window in (b) without the magnet (d) and with the magnet (e). The observation window is 6.7 mm away from the entrance of the main channel. The flow rate of inlet A is fixed at 4 μL min^{-1}, ferrofluid concentration is fixed at 0.26%, and magnetic field gradient is fixed at 32.2 T m^{-1} for (a)-(f). Numerical simulation of separation distance ΔY and deflection distance Y_2 at the end of the channel with parameters including: (f) channel length, (g) magnetic field gradient, (h) flow rate of inlet A, and (i) ferrofluid concentration. Experimental calibration of these parameters for separation distance ΔY and deflection distance Y_2 using microparticles: (j) ΔY and Y_2 as a function of magnetic field gradient,

(k) ΔY and Y_2 as a function of flow rate of inlet A, (l) ΔY and Y_2 as a function of ferrofluid concentration. The flow rate of inlet A is fixed at 4 μL min^{-1} and ferrofluid concentration is fixed at 0.26% (v/v) for (g) and (j). Magnetic field gradient is fixed at 32.2 T m^{-1} and ferrofluid concentration is fixed as 0.26% (v/v) for (h) and (k). Magnetic gradient is fixed at 32.2 T m^{-1} and the flow rate of inlet A is fixed at 4 μL min^{-1} for (i) and (l). Scale bars: 200 μm.

device and flow parameters used in cell separation, we estimated that a homogeneous mixing could be achieved at a channel length of a few millimeters away from the inlets (Figure 4.6), which was confirmed by experimental observations in Figures 4.5d and e. Given that the total channel length was ~5 cm, we considered the effects from mixing on cell separation to be minimal and neglected them in the following optimization.

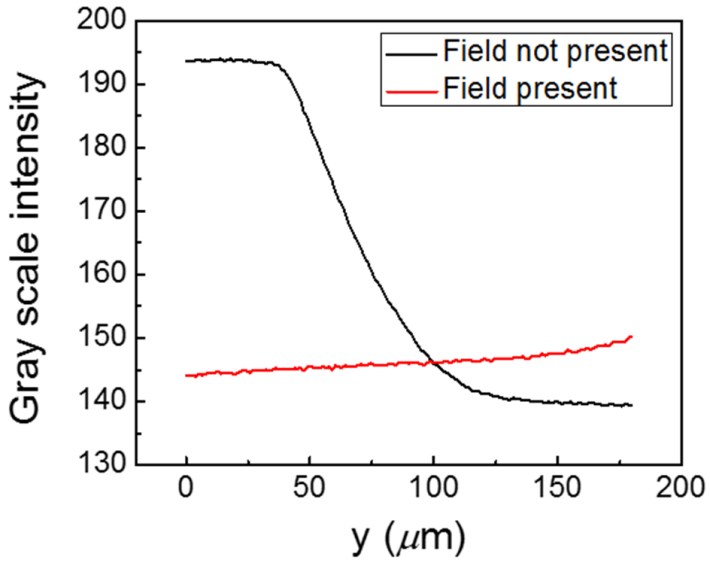

Figure 4.6: The mean gray scale intensity in the red boxes of Figures 4.5d and e as a function of channel width.

We first optmized the channel length, as the dimensions of the permanent magnet used in the separation remained constant. Figure 4.5f shows under typical device and flow parameters, both ΔY and Y_2 increased with the channel length, and reached

saturation when the length was around 5.8 cm. It should be noted that the optimized channel length could be affected by parameters including flow rates, magnet properties, ferrofluid properties, and cell types. The second set of parameters we optimized for the device were the magnetic field strength and its gradient, both of which changed their values as we adjusted the distance between the magnet and channel (Figure 4.2). Figures 4.5g and j show in both simulation and calibration, when the magnetic field gradient increased, the overall deflection of 15.7 μm microparticle Y_2 increased, too. This was because the driving force – magnetic buoyancy force on the microparticles, was determined in part by the gradient. The larger the gradient, the larger the magnetic force and resulted deflection of microparticles. Interestingly, the simulated separation distance between two microparticles, ΔY had a peak at a medium gradient (38.2 T m^{-1}), which was confirmed by the calibration experiments. This was due to the fact that both microparticles reached their maximum deflections very quickly under a strong gradient (83.4 T m^{-1}) in the device, resulting in a mixing rather than separation of the two types of microparticles. On the other hand, separation distance also decreased when the gradient was too weak (12.9 T m^{-1}) to deflect microparticles and distinguish them. As a result, we chose to use the medium field and gradient (134 mT and 32.2 T m^{-1}) for subsequent cell separation.

A third parameter to optimize was the flow rate of cell inlet (inlet A in Figure 4.1c). Both simulation (Figure 4.5h) and calibration (Figure 4.5k) results show a monotonically decreasing trend for Y_2 and ΔY, as the magnitude of the flow rate increased. This was consistent with the findings from existing cell separation

technologies,[14] where a tradeoff existed between throughput (flow rate in this case) and separation efficiency (separation distance ΔY in this case).

The last parameter we chose to optimize was the ferrofluid concentration. Generally speaking, a higher concentration of ferrofluid resulted in a higher magnitude of magnetic force on the microparticles, leading to a larger deflection, which was observed in both simulation and calibration (Figures 4.5i and l) of Y_2. However, a high ferrofluid concentration was not necessarily beneficial for achieving a larger separation distance ΔY. Figure 4.5i shows there was an optimal ferrofluid concentration close to 0.17% (v/v) for both ΔY and Y_2. Concentrations higher than 0.17% (v/v) resulted in larger Y_2 but smaller ΔY. This was because both microparticles achieved sufficient deflections in a strongly magnetized ferrofluid, resulting in mixing rather than separation of the two. Microparticle calibration experiments in Figure 4.5l did not capture this optimal concentration, as there were only three concentrations of ferrofluids used.

While the simulation and calibration results matched each other quite well qualitatively, we noticed quantitate differences between the two for the separation distance ΔY. The simulation results consistently yielded larger ΔY than the calibration. This might be due to the fact that the simulation did not take into account the widening of cell streams, which effectively reduced the separation distance, as shown in Figure 4.5c.

Because of the device design and the diffusion between ferrofluids and buffer stream, cell separation efficiency and the amount of ferrofluids in collection outlet could affect each other. In this study, our goal was to not only achieve biocompatible and label-free cell separation with best possible separation efficiency, but also maintain cell integrity. As a result, we optimized the flow rates of ferrofluids and buffer stream so that

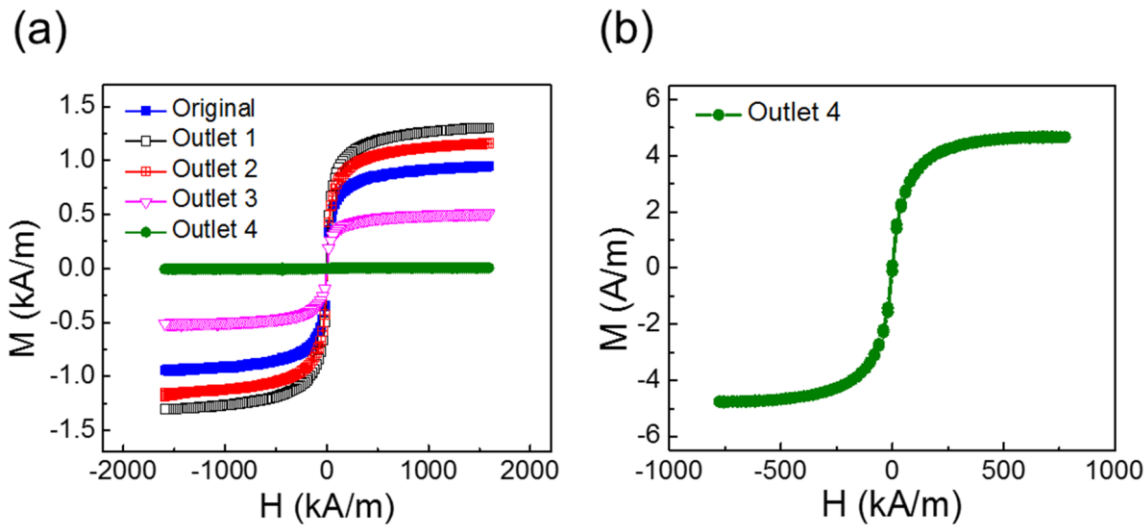

Figure 4.7: (a) Magnetizations of the original ferrofluid (blue) and ferrofluids collected from each outlet. Ferrofluids collected from outlets 1 and 2 (black and red) had higher concentrations of magnetic nanoparticles, possibly due to the attraction of the permanent magnet. Ferrofluids collected from outlet 3 (purple) had approximately half concentration of the nanoparticles in the original ferrofluid. Ferrofluids collected from outlet 4 had significantly less nanoparticles than the original ferrofluid. (b) Magnetization of ferrofluids collected from outlet 4. Saturation magnetization was measured to be 4.75 A/m, corresponding to a 0.00128% volume fraction of magnetic materials. For comparison, the original ferrofluid had a 0.26% volume fraction of magnetic materials.

their diffusion boundary was at exactly the boundary of outlets 3 and outlet 4 (collection outlet). This way, the majority of spiked cancer cells could be extracted, while the amount of ferrofluids was minimized in collection outlet. We estimated the concentration of magnetic nanoparticles that diffused into the collection outlet to be ~0.002% (v/v) via a simulation using typical flow rate parameters. A magnetization measurement from one experiment revealed a 0.00128% (v/v) concentration of the liquid collected from the same outlet (Figure 4.7), which was on the same order of magnitude as the simulation. This measured concentration of nanoparticles in the collection outlet was 203-fold more dilute than the original ferrofluid, and unlikely produced detrimental effects to cells. We

also estimated via a simulation the overall exposure time of cells in ferrofluids to be 4-53 seconds depending on the cell input flow rates (0.5-20 μL min^{-1}) in current devices.

Finally, we verified these optimized and calibrated parameters (magnetic field and gradient: 134 mT, 32.2 T m^{-1}, ferrofluid concentration: 0.26% v/v, channel length: 5.8 cm) with a separation of spiked cancer cells (A549 lung cancer and MCF-7 breast cancer, 100 cells mL^{-1}) from diluted human whole blood (RBC concentration: 2×10^6 cells mL^{-1}) at 0.9 mL h^{-1} throughput. Detailed results are summarized in Figure 4.8 and Table 4.2. Briefly, separation efficiency (defined as the ratio of captured cancer cells to spiked cancer cells) for A549 cell line was 77±6%, and the purity of cancer cells recovered (defined as the ratio of cancer cells to all cell types in collection outlet) was 62.1±0.9%. Separation efficiency for MCF-7 cell line was 84±4%, and its purity was 59.2±0.8%. We concluded that these optimized parameters could be used to enable a high-throughput and high efficiency low-concentration cell separation in ferrofluids.

Table 4.2: Summary of cancer cell separation performance with diluted whole blood.

Cell line	No. of cells spiked	No. of cells captured	Efficiency	No. of WBCs	Purity
A549	100	77±6	77±6%	47±11	62.1±0.9%
MCF-7	100	84±4	84±4%	58±18	59.2±0.8%

100 CellTracker Green stained cancer cells were spiked into 1 mL of diluted whole blood (1000-time dilution, mostly RBCs). Data are expressed as Mean±S.D., n=3.

4.4.4 Cell Separation

We chose to validate the biocompatible cell separation strategy using spiked cancer cells from cell culture lines in undiluted white blood cells (WBCs). Separating spiked cancer cells from WBCs is potentially the first step to render ferrofluid-based

"negative magnetophoresis" useful in rare cell separation applications such as enriching circulating tumor cells (CTCs) from peripheral blood.[153] Since CTCs occur at an extremely low concentration of 1-10 cells every 1 billion RBCs and 1 million of WBCs,[130, 164, 165] its enrichment requires the development of a highly efficient and high-throughput separation.[157] For that purpose, we scaled up the device by increasing the depth of the device from 52 µm to 150 µm in Figure 4.1d to accommodate high cell flow rates (20 µL min^{-1}, i.e., 1.2 mL h^{-1}, see Figure 4.8 for device calibration), and chose the optimized magnetic field and gradient (134 mT, 32.2 T m^{-1}), ferrofluid concentration (0.26% v/v), and channel length of 5.8 cm based on previous optimization and calibration results. Mean diameters of all cells used here were measured to be: 15.5 µm for A549, 16.9 µm for H1299, 18.7 µm for MCF-7, 18.1 µm for MDA-MB-231, 18.9 µm for PC-3, and 11.1 µm for WBCs.

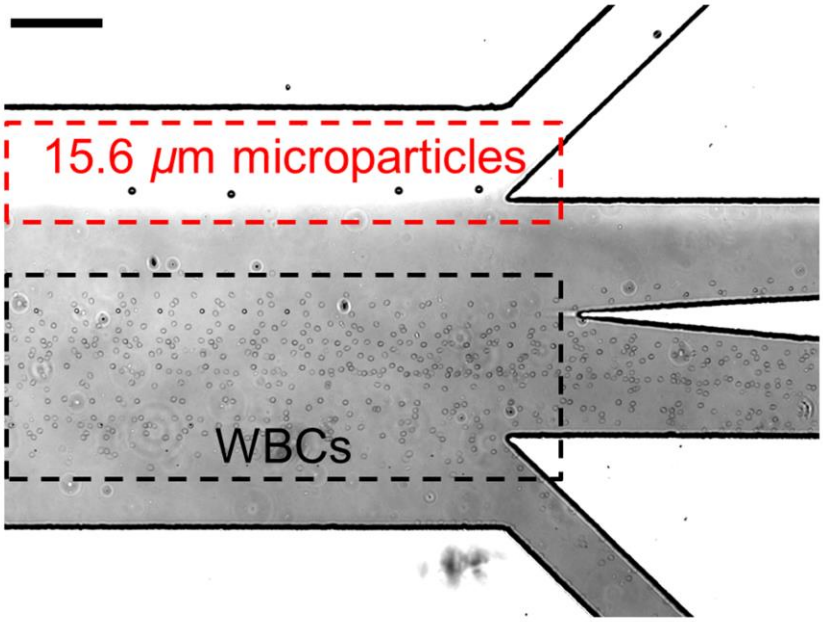

Figure 4.8: Calibration of 15.6 µm microparticles and white blood cells (WBCs). Scale bar: 200 µm.

We validated the separation of spiked cancer cells from undiluted human blood with only WBCs. This is more challenging than separating cancer cells and RBCs, as the size differences between cancer cells and WBCs are much subtler. We used A549, H1299, MCF-7, MDA-MB-231, and PC-3 cell lines, with a spike ratio of ~100 cells in 1 mL of undiluted WBCs. Cell flow rate was 1.2 mL h^{-1}. Experimental results are summarized in Figures 4.9a-c and Table 4.3. Figure 4.9a shows A549 cancer cells and WBCs were flowing near the bottom of the channel and exiting through the outlet 1, resulting in no separation of the two when there was no magnetic field. Figure 4.9b shows larger A549 cancer cells deflected from the ferrofluid stream into the PBS buffer stream toward outlet 4 when there was a magnetic field. WBCs remained in the ferrofluid stream and exited through outlets 2 and 3. Fluorescence image of A549 cells confirmed such separation in Figure 4.9c. From Table 4.3, the separation efficiency for A549 cells was 80±3%. The purity of cancer cells was 25.3±0.1% from outlet 4. Similar experiments

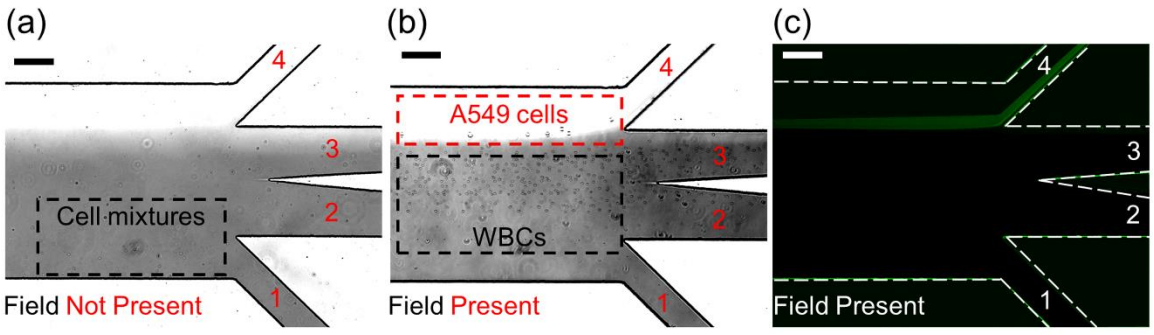

Figure 4.9: Micrographs of spiked cancer cells of cell culture lines and white blood cells (WBCs) separation processes. (a) In absence of magnetic fields, cell mixtures exited the channel through outlet 1. (b) When magnetic fields were present, larger A549 cancer cells were deflected and reached the ferrofluid/buffer boundary, exited through outlet 4 (collection outlet), while smaller WBCs exited through other outlets. (c) Fluorescence images of A549 cancer cells during cell separation. A549 cells were stained with CellTracker Green. Dashed white lines depict the microchannel boundaries. Scale bars: 200 μm.

were carried out to separate multiple cancer cell lines from WBCs. The separation efficiencies were 81±5%, 82±5%, 82±4%, and 86±6% for H1299, MCF-7, MDA-MB-231, and PC-3 cells. Even with the subtle size difference between cancer cells and WBCs, we were able to achieve high separation efficiency (80-86%) using this strategy. The purity of cancer cells was on the order of 20% for all cases. This size-based separation strategy performed well in separating cancer cells from WBCs. As the diameter of cancer cells increased from 15.5 μm (A549) to 18.9 μm (PC-3), we observed a slight increase in separation efficiency, which is expected as the separation is based on size difference of cell types.

Table 4.3: Summary of cancer cell separation performance.

Cell line	No. of cells spiked	No. of cells captured	Efficiency	No. of WBCs	Purity
A549	100	80±3	80±3%	236±22	25.3±0.1%
H1299	100	81±5	81±5%	218±15	27.1±0.1%
MCF-7	100	82±5	82±5%	208±29	28.3±0.1%
MDA-MB-231	100	82±4	82±4%	233±48	26.0±0.2%
PC-3	100	86±6	86±6%	212±32	28.8±0.1%

100 CellTracker Green stained cancer cells were spiked into 1 mL of WBCs. Data are expressed as Mean±S.D., n=3.

We investigated the short-term viability and the long-term proliferation of separated A549 cancer cells collected from the device. After running the cell mixture through the device for separation, A549 cells were collected from the outlet 4 and studied for their viability using a Live/Dead assay. Figure 4.10a shows the viability of A549 cells before and after separation were 95.2±2.0% and 93.8±1.5%, respectively. Figure 4.10b shows representative fluorescence images of A549 cells before and after separation using

a Live/Dead stain. They indicate no significant impact on cell viability from the ferrofluid exposure and cell processing. We also examined the long-term proliferation of A549 cancer cells after separation. Figure 4.10c shows the images of A549 cells over a 4-day period and Live/Dead staining of the cultured cells on day 4. We concluded that A549 cells were able to proliferate to confluence.

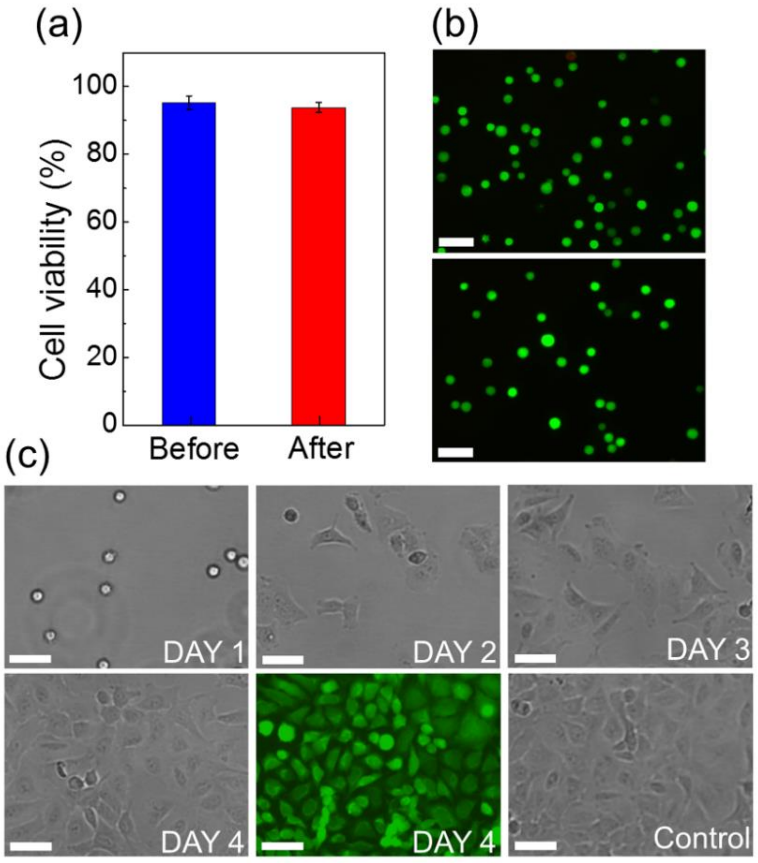

Figure 4.10: Short-term and long-term cell viability comparison. (a) Short-term cell viability comparison between before vs. after separation groups. No significant difference was found between the two. (b) Representative images of Live/Dead staining of the before (top) and after separation (bottom) groups. Calcein-AM (green) and PI (red) channels were merged in these images. Scale bars: 100 μm. (c) Bright field images of cultured A549 cells collected after separation from day 1 to day 4. A Live/Dead staining of the cultured cells on day 4 showed excellent viability. A control group of cell culture was used for comparison. No significant difference was found in cell proliferation between cells in the control group and cells collected after device separation. Scale bars: 50 μm.

In summary, we developed a biocompatible and label-free cell separation method using ferrofluids, to differentiate between low-concentration cancer cells of cell culture lines and WBCs with subtle size differences in a high-throughput and high-efficiency manner. Separated cancer cells showed excellent average viability (94.4±1.3%) and normal proliferation. This could be useful in preserving cell integrity for further analysis after enrichment. We achieved on average 82.2% separation efficiency in separating a variety of cancer cells from cell culture lines from WBCs at an extremely low concentration of ~100 cells per mL with a throughput of 1.2 mL h^{-1}. The efficiency obtained here is comparable the average reported efficiency of 82% from recent label-free microfluidic separation of cultured cancer cells in blood.[157] For examples, the separation efficiency reported here is close to the efficiencies of methods based on standing surface acoustic wave,[166] dielectrophoresis,[167-169] slanted spiral channel,[170] and is higher than the efficiency of vortex technology.[171-173] The purity of recovered cancer cells from this method was between 25.3% and 28.8% depending on specific cell lines. It is also comparable to the reported purity values from existing label-free methods when they were used to separate spiked cancer cells from blood. These reported purities varied dramatically from 0.1% to 90%,[166-173] as most of the label-free methods focused on improving separation efficiency of low-concentration cells, rather than their purity. For examples, the recovered cancer cell purity of this method is higher than purities reported from the standing surface acoustic wave method (0.1%, calculated from ~90% WBC removal rate after separation),[166] and a few dielectrophoretic methods (10%[168] and 16.24%[169]), but lower than purities from the slanted spiral channel method (50%),[170] and the vortex technology (57-94%).[171-173]

Although the throughput of current devices (1.2 mL h^{-1}) is comparable to the throughput from methods based on standing surface acoustic wave[166] and dielectrophoresis,[167-169] it needs improvement in order to handle the clinically relevant amount of human blood (*e.g.*, 7.5 mL h^{-1} for CTCs enrichment), which was demonstrated by methods such as slanted spiral channel[170] and vortex technology.[171-173]. Further scale-up of a single device and/or potential multiplexing of several devices together could improve the throughput. As a proof-of-concept demonstration, this method was used to separate low-concentration spiked cancer cells from WBCs, with RBCs removed beforehand by a RBC lysis buffer. In the future, it is beneficial and necessary to design a two-step separation device, which can first remove the bulk of RBCs, and then further enrich cancer cells from mostly WBCs to automate whole blood processing on-chip. While other methods have been demonstrated to be able to handle clinical samples such as whole blood,[166, 169-173] this method was still at its early stage of development and was limited to cultured cancer cell. Future studies using whole blood needs to be conducted to further evaluate the potential of this method in rare cell separation.

4.5 Conclusions

In this study, we reported a biocompatible and label-free separation method of low-concentration cancer cells of cell culture lines from undiluted white blood cells based on their size difference, by using a custom-made ferrofluid and integrating on-chip sample preparation, separation and extraction into a microfluidic device. The ferrofluid possessed not only ideal biocompatible properties for live cell manipulation, including its low magnetic content concentration (*e.g.*, 0.26% volume fraction), neutral pH, isotonicity, maghemite nanoparticles and their surfactant but also excellent colloidal

stability that enables high-throughput and high-efficiency continuous separation. A biocompatibility study of 7 commonly used cancer cell lines showed consistently over 90% of short-term viabilities and abilities to proliferate to confluence for all cells, even after extended exposure to this ferrofluid. Additionally, an optimized device design eliminated time-consuming off-chip sample preparation and extraction steps, which reduced overall exposure time of cells to ferrofluids from hours to seconds. To demonstrate the potential of this method in rare cell separation, a variety of cancer cells from cell culture lines in white blood cells were separated with an average efficiency of 82.2%, at a throughput of 1.2 mL h^{-1} with an extremely low concentration of ~100 cancer cells mL^{-1}. Separated cancer cells showed excellent viability and normal proliferation. This method addressed the challenges associated with cell separation in ferrofluids, including excellent biocompatibility of not only the custom-made ferrofluid, but also the assay itself, as well as device design and optimization specifically for the low concentration of target cells. While still at its early stage of development, this method could be a promising tool for rare cell separations because of its excellent biocompatibility, label-free operation, performances with culture cancer cells, along with potentials for device scale-up, multiplexing, and further optimization.

CHAPTER 5

LABEL-FREE FERROHYDRODYNAMIC CELL SEPARATION OF CIRCULATING TUMOR CELLS [1]

[1] W. Zhao, R. Cheng, B. D. Jenkins, T. Zhu, N. E. Okonkwo, C. E. Jones, M. B. Davis, S. K. Kavuri, Z. Hao, C. Schroeder and L. Mao, *Lab Chip*, 2017, **17**, 3097-3111. Reprinted here with permission of The Royal Society of Chemistry.

5.1 Abstract

Circulating tumor cells (CTCs) have significant implications in both basic cancer research and clinical applications. To address the limited availability of viable CTCs for fundamental and clinical investigations, effective separation of extremely rare CTCs from blood is critical. Ferrohydrodynamic cell separation (FCS), a label-free method that conducted cell sorting based on cell size difference in biocompatible ferrofluids, has thus far not been able to enrich low-concentration CTCs from cancer patients' blood because of technical challenges associated with processing clinical samples. In this study, we demonstrated the development of a laminar-flow microfluidic FCS device that was capable of enriching rare CTCs from patients' blood in a biocompatible manner with a high throughput (6 mL h^{-1}) and a high rate of recovery (92.9%). Systematic optimization of the FCS devices through a validated analytical model was performed to determine optimal magnetic field and its gradient, ferrofluid properties, and cell throughput that could process clinically relevant amount of blood. We first validated the capability of the FCS devices by successfully separating low-concentration (~100 cells mL^{-1}) cancer cells using six cultured cell lines from undiluted white blood cells (WBCs), with an average 92.9% cancer cell recovery rate and an average 11.7% purity of separated cancer cells, at a throughput of 6 mL per hour. Specifically, at ~100 cancer cells mL^{-1} spike ratio, the recovery rates of cancer cells were 92.3±3.6% (H1299 lung cancer), 88.3±5.5% (A549 lung cancer), 93.7±5.5% (H3122 lung cancer), 95.3±6.0% (PC-3 prostate cancer), 94.7±4.0% (MCF-7 breast cancer), and 93.0±5.3% (HCC1806 breast cancer), and the corresponding purities of separated cancer cells were 11.1%±1.2% (H1299 lung cancer), 10.1±1.7% (A549 lung cancer), 12.1±2.1% (H3122 lung cancer), 12.8±1.6% (PC-3

prostate cancer), 11.9±1.8% (MCF-7 breast cancer), and 12.2±1.6% (HCC1806 breast cancer). Biocompatibility study on H1299 cell line and HCC1806 cell line showed that separated cancer cells had excellent short-term viability, normal proliferation and unaffected key biomarker expressions. We then demonstrated the enrichment of CTCs in blood samples obtained from two patients with newly diagnosed advanced non-small cell lung cancer (NSCLC). While still at its early stage of development, FCS could become a complementary tool for CTC separation for its high recovery rate and excellent biocompatibility, as well as its potential for further optimization and integration with other separation methods.

5.2 Introduction

Circulating tumor cells (CTCs) are cancer cells that are detached from primary solid tumors and carried through the vasculature to potentially seed distant site metastases in vital organs – the main cause of death by cancer.[174, 175] Molecular assessments of CTCs not only could benefit basic cancer research, but also might eventually lead to a more effective cancer treatment.[164, 176, 177] However, one major limitation of CTCs in cancer research and its clinical applications has been the limited availability of viable CTCs for investigations, due in part to the small patient blood volumes that are allowable for research, which usually yielded less than 100 CTCs from 1 mL of whole blood.[130, 164, 165] As a result, technologies are needed in order to separate these rare cells from blood, and important performance criteria for these technologies include the ability to process a significant amount of blood quickly (*e.g.*, throughput ~7.5 mL h^{-1}), a high recovery rate of CTCs, a reasonable purity of isolated cancer cells, and cell integrity for further characterization.[157]

CTCs represent the composition of the primary tumor, including the heterogeneity of tumors.[164, 178] While CTCs initially express same biological or physical markers as the primary tumor epithelial cells, once in circulation they may undergo morphological and gene expression changes, which could determine what distant site will become the new niche for a metastatic tumor. Enriching the whole CTC population, instead of just the ones responding to specific biological or physical markers, can allow basic investigations such as CTC heterogeneity, and may lead to a more precise prognosis of undetected metastasis and recurrence risk for cancer patients.[179] Label-based CTC separation technologies were developed to selectively enrich a subset of CTCs from blood, primarily through the use of specific biological markers including epithelial cell adhesion molecule (EpCAM).[3, 180, 181] These antigen-based labels were a rate-limiting factor in effective CTC separation, as the inherent heterogeneity of CTCs might render these technologies ineffective for general use. The vast array of various biomarkers that might or might not be expressed, and which could not be predicted to remain expressed in CTCs undergoing Epithelial-to-Mesenchymal Transitions (EMT) would be cumbersome and confounding in these label-based methods. Furthermore, most label-based technologies did not conveniently enable comprehensive molecular analysis of separated CTCs because they were either dead or immobilized to a surface.[182] On the other hand, a variety of label-free methods including those based on filtration,[183] acoustophoresis,[166] dielectrophoresis,[167-169] dean flow,[170, 184, 185] and vortex technology[171-173] were developed recently to exploit specific physical markers in order to deplete non-CTCs in blood therefore enrich cancer cells. They were not affected by the heterogeneity of biological marker expressions and could permit enrichment of nearly all CTCs that were above a predetermined threshold of

a physical marker, for example, the size of CTCs. Most CTCs of epithelial origin have a size range between 15 μm and 25 μm, and are larger than red blood cells (RBCs, 6-9 μm), and the majority of white blood cells (WBCs, 8-14 μm).[157] However, CTCs of smaller sizes were found in blood circulation.[186, 187] The existence of large WBCs such as monocytes that may have overlapping sizes with CTCs could further complicate label-free separation methods.[130, 182, 188] Both label-based and label-free methods had their limitations; more sophisticated strategies including novel sorting methods such as acoustophoresis[166] and vortex technology[171-173], or a combination of two or more methods to enrich rare cells based on multiple biological or physical markers could potentially improve the overall performance of CTC separation.[189-193] One successful device is the CTC-iChip that integrated both label-based and label-free separation methods. This device first used deterministic lateral displacement to deplete smaller RBCs from patient blood based on their size, then applied inertial force to focus remaining cells into a narrow stream, and eventually separated WBCs that were coated with anti-CD45 and anti-CD66b magnetic beads from CTCs for a high-throughput and high-recovery separation.[189, 190] While each of these three methods alone might have its own limitation in rare cell separation, their integration were critical to the overall success of CTC-iChip. There is a need to develop new and high-performance CTC separation method that not only performs well on its own, but also can be easily integrated with other methods to achieve high-throughput, high-recovery, high-purity separation of intact CTCs. A frequently used method in CTC or rare cell separation was functionalizing magnetic particles to target and pull cells of interest through magnetic force or “magnetophoresis” towards a magnetic field maxima, as illustrated in Figure 5.1a. Magnetophoresis, when

used for CTC separation, has achieved high-throughput and high-specificity isolation of cancer cells from blood.[7, 181, 194-200] On the other hand, it is a label-based method and requires time-consuming and laborious sample preparation.

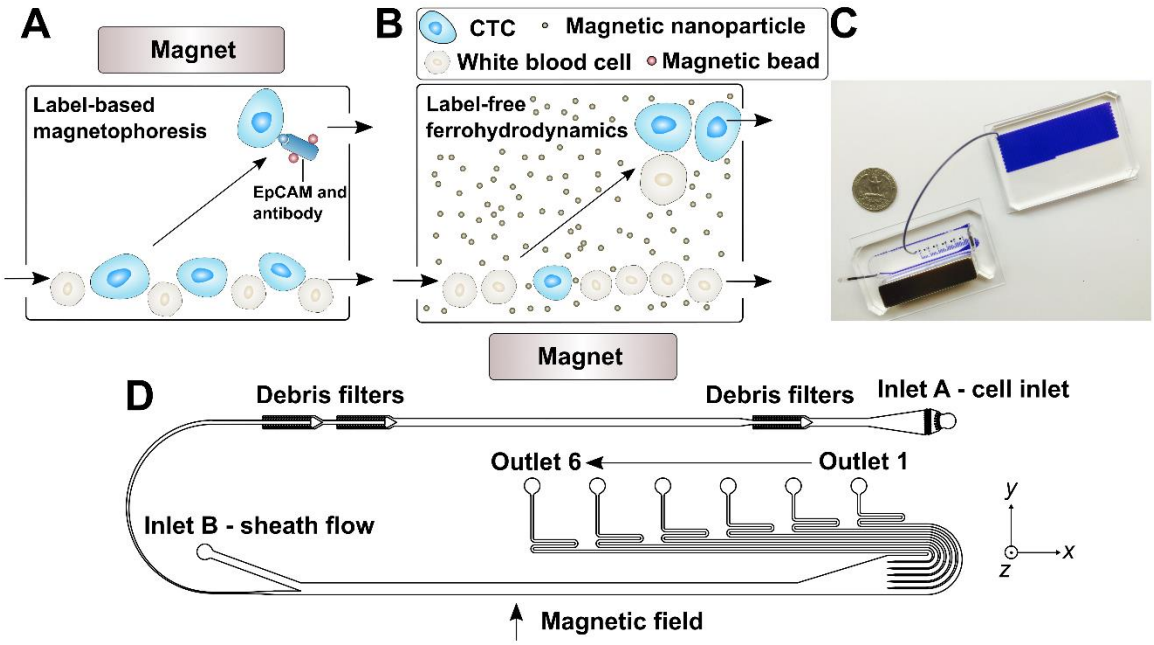

Figure 5.1: (a) Schematic illustration of traditional and frequently used label-based magnetophoresis for CTC separation, in which rare cells were targeted via specific biomarkers such as epithelial cell adhesion molecule (EpCAM) through functionalized magnetic particles in order to pull these cells through magnetic force towards magnetic field maxima in a continuous-flow manner. (b) Schematic illustration of a label-free ferrohydrodynamic cell separation (FCS) for CTCs. In FCS, RBC-lysed blood and biocompatible ferrofluids (colloidal suspensions of magnetic nanoparticles) were processed in continuous flow within a FCS device, such as the one shown in (c) and (d). Cells in blood were first filtered to remove debris, then focused by a ferrofluid sheath flow from inlet B. After entering the channel region that was on top of a permanent magnet, large cells including CTCs and some WBCs experienced more size-dependent magnetic buoyance force than smaller WBCs, resulting in a spatial separation between them at the outlets of the FCS device. (c) A photo of a prototype FCS device (left) consisted of a PDMS microchannel and a permanent magnet. The FCS device was connected to a serpentine PDMS collection chamber (right) that was used to accurately count cancer cells or WBCs during FCS calibration experiments using cultured cancer cells. A U.S. quarter was shown for size comparison. Blue dye was used to visualize the channel. (d) Top-view of the FCS device with labels of inlets, debris filters and outlets. A total of 6 outlets were fabricated in order to account for the broad size distributions of cells. The arrow indicates the direction of magnetic field during device operation.

In this paper, we reported a new ferrohydrodynamic cell separation (FCS) method that still used magnetic buoyance force for size-based CTC separation, but was label-free, biocompatible and enriched rare CTCs from patient blood with a high throughput and a high rate of recovery. We demonstrated that FCS could separate a variety of low-concentration cancer cells of cell culture lines from RBC-lysed blood at a throughput of 6 mL h^{-1}, with an average cancer cell recovery rate of 92.9% and an average cancer cell purity of 11.7% after separation. CTCs were successfully enriched from blood samples of two non-small cell lung cancer (NSCLC) patients using FCS devices. We envision that FCS could offer the potential to serve as a complementary tool in CTC separation because of its excellent biocompatibility and label-free operation. FCS could also be integrated with other separation methods such as magnetophoresis for a more comprehensive isolation of rare cells. The working principle of ferrohydrodynamic cell separation is "negative magnetophoresis" in biocompatible ferrofluids, as illustrated in Figure 5.1b.[153] Cells including CTCs and WBCs immersed inside an uniformly magnetic media (ferrofluids) can be considered as "magnetic holes".[43] A non-uniform magnetic field gradient induces an imaginary dipole moment in these "magnetic holes", and generates a size-dependent magnetic body force, also referred to as magnetic buoyancy force that pushes the cells away to a magnetic field minima.[27] Forces on the cells can therefore sort them based on their size difference in a continuous ferrofluid flow. In practice, a mixture of RBC-lysed blood and ferrofluids was injected into the inlet A of a FCS device such as the one shown in Figure 5.1c. Cells in blood were filtered then focused by a sheath flow from inlet B. After entering the channel region that was on top of a permanent magnet, large cells including CTCs and some WBCs experienced more

size-dependent magnetic buoyance force than smaller WBCs, resulting in a spatial separation between them at the outlets of the device. Although ferrohydrodynamic cell separation was demonstrated before,[38, 44, 93, 95, 201] its application in CTCs was challenging in the past for the following reasons. First, rarity of CTC necessitates a blood-processing throughput of close to 7.5 mL h^{-1} and recovery rate of at least 80% in low concentration (<100 cells mL^{-1}) conditions.[157] Previous applications of ferrohydrodynamic cell separation mostly focused on sorting of bacteria and yeast cells,[44, 93] bacteria and red blood cells,[38] and cancer cells of cultured cell lines from blood.[95, 201] The throughputs of these studies were lower than what was required of CTC separation, and the target cells were mostly spiked at a much higher concentration (*e.g.*, 10^5-10^6 cells mL^{-1}) than CTCs.[38, 44, 93, 95] Second, ferrofluids, as a colloidal suspension of magnetic nanoparticles with diameters of approximately 10 nm, need to be rendered biocompatible for CTC separation. Cancer cells should remain alive and their normal functions should be kept intact during and after the separation for post-separation characterization. It is therefore critical to systematically optimize FCS and ferrofluid design so that the throughput and recovery rate of separation are comparable to those needed for CTC separation, and the separated cells are viable, and their normal functions are intact.

We overcame these challenges associated with ferrohydrodynamic cell sorting of CTCs and demonstrated a 92.9% recovery rate and an 11.7% purity of low-concentration (~100 cells mL^{-1}) cancer cells with a blood-processing throughput of 6 mL of blood per hour, and validated the technology using blood from NSCLC patients. We performed systematic parametric studies of key factors influencing the performance of FCS and determined parameters for high-throughput, high recovery rate and biocompatible CTC

separation. We then tested and validated the performance of the method with cancer cells from 6 cultured cancer cell lines and 3 different types of cancer. The mean recovery rate of cancer cells from RBC-lysed blood using this technology is 92.9%, a value much better than currently reported an average of 82%.[157] Separated cancer cells had excellent short-term viability, unaffected biological marker expressions, and intact capability to proliferate to confluence. Finally, we applied the FCS method to successfully enrich CTCs from blood samples of two stage IVB NSCLC patients and discussed the advantages and limitations of this method and potential ways to improve.

5.3 Experimental Section

5.3.1 Modeling of FCS and Its Calibration

The model used in this study to simulate cell trajectories in three-dimensional (3D) manner was previously described.[46, 110] We modified the analytical model for this study, which could predict the 3D transport of diamagnetic cancer cells and WBCs in ferrofluids inside a microfluidic channel coupled with permanent magnets. Details are listed below. The magnets produced a spatially non-uniform magnetic field that led to a magnetic buoyancy force on the cells. Trajectories of the cells in the device were obtained by (1) calculating the 3D magnetic buoyancy force via an experimentally verified and analytical distribution of magnetic fields as well as their gradients, together with a nonlinear Langevin magnetization model of the ferrofluid, (2) deriving the hydrodynamic viscous drag force with an velocity profile of the channel obtained from COMSOL Multiphysics (Version 3.5, COMSOL Inc., Burlington, MA), (3) solving governing equations of motion using analytical expressions of magnetic buoyancy force and hydrodynamic viscous drag force in MATLAB (MathWorks Inc., Natick, MA). The

parameters of simulation (device dimension and geometry, fluid and cell properties, and magnetic fields) reflected exact experimental conditions.

Polystyrene microparticles (Polysciences, Inc., Warminster, PA) with diameters of 15.7 μm were mixed together with WBCs at the concentration of 1×10^4 particles mL^{-1} for model calibration. Microparticle and cell mixtures were injected into inlet A of a FCS device with a flow rate of 1.2-6 mL h^{-1}. The flow rate of inlet B was fixed at 6 mL h^{-1} for all experiments. The magnet was placed 1 mm away from the channel, which corresponded to magnetic field strengths 443 mT and magnetic field gradients 56.2 T m^{-1} (Figure 5.2). A ferrofluid with a concentration of 0.26% (v/v) were used in calibration experiments.

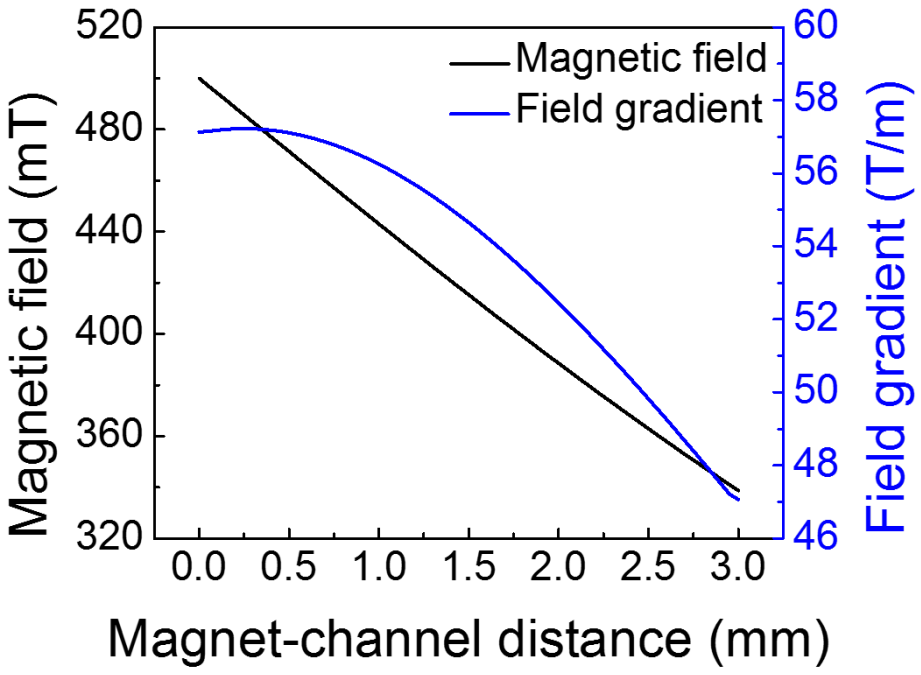

Figure 5.2: Measured magnetic field and its gradient of the center of magnet's surface vs. distance between the magnet's surface and the microfluidic channel wall.

5.3.2 Custom-Made Biocompatible Ferrofluids

A water-based ferrofluid with maghemite nanoparticle was synthesized by a chemical co-precipitation method and made biocompatible following a protocol previously described.[95, 201] Size and morphology of the maghemite nanoparticles were characterized via transmission electron microscopy (TEM; FEI Corp., Eindhoven, the Netherlands). Magnetic properties of the resulting biocompatible ferrofluid were measured at room temperature using a vibrating sample magnetometer (VSM; MicroSense, LLC, Lowell, MA). Briefly, particle size distribution of the custom-made ferrofluid was 10.24±2.52 nm. Saturation magnetization of the as-synthesized ferrofluid was 0.96 kA m^{-1}, corresponding to an estimated 0.26% volume fraction of magnetic content. This ferrofluid was colloidally stable for up to 10 months' storage, did not show particle agglomeration during microfluidic operations, and was made to be isotonic and have a 7.0 pH and neutral surfactant for biocompatible cell separation.

5.3.3 Cell Culture and Sample Preparation

Six cancer cell lines (ATCC, Manassas, VA) including three lung cancer cell lines (H1299, A549 and H3122), one prostate cancer cell line (PC-3), and two breast cancer cell lines (MCF-7 and HCC1806) were used in this study. H1299, A549, H3122, PC-3, and HCC1806 cells were cultured in RPMI-1640 medium (Mediatech, Inc., Manassas, VA) supplemented with 10% (v/v) fetal bovine serum (FBS; Life Technologies, Carlsbad, CA) and 1% (v/v) penicillin/streptomycin solution (Mediatech, Inc., Manassas, VA). MCF-7 cells were cultured in Dulbecco's modified eagle medium (DMEM; Life Technologies, Carlsbad, CA) supplemented with 10% (v/v) FBS, 1% (v/v) penicillin/streptomycin solution and 0.1 mM MEM non-essential amino acid (NEAA;

Life Technologies, Carlsbad, CA). All cell cultures were maintained at 37 °C under a humidified atmosphere of 5% CO_2. Cell lines were released through incubation with 0.05% Trypsin-EDTA solution (Life Technologies, Carlsbad, CA) at 37 °C for 5-10 minutes before each use.

Cancer cells were fluorescently stained by incubation with 2 μm CellTracker Green (Life Technologies, Carlsbad, CA) for 30 minutes before each use. Probe solution was replaced with culture medium by centrifuging at 200×*g* for 5 minutes. Cells were counted with a hemocytometer (Hausser Scientific, Horsham, PA) and serially diluted in culture medium to achieve a solution with approximately 1×10^4 cells per mL. Cells were then counted with a Nageotte counting chamber (Hausser Scientific, Horsham, PA) to determine the exact number of cells per μL. Desired number of cancer cells (50, 100, 200, 500, 1000, or 2000) were spiked into 1 mL of WBCs (RBC-lysed whole blood). The number of cancer cells spiked was determined by the average of two counts, with an average of 5.2% difference between the counts. We chose to focus on separating cancer cells from WBCs because of the size of WBCs (8-14 μm) were much closer to cancer cells (15-25 μm) than RBCs (6-9 μm).

Human whole blood from healthy subjects (Zen-Bio, Research Triangle Park, NC) was lysed by RBC lysis buffer (eBioscience, San Diego, CA) with a volume ratio of 1:10 for 5 minutes at room temperature. Cell mixtures were centrifuged at 800×*g* for 5 minutes and the pellet was suspended in the same volume of ferrofluid containing 0.1% (v/v) Pluronic F-68 non-ionic surfactant (Thermo Fisher Scientific, Waltham, MA). WBCs were fixed by 4% (w/v) paraformaldehyde (PFA; Santa Cruz Biotechnology, Dallas, TX) at 4 °C for 30 minutes for long-term use.

5.3.4 Biocompatibility study of FCS

Short-term cell viability after FCS was examined using a Live/Dead assay (Life Technologies, Carlsbad, CA). 1×10^6 H1299 cancer cells suspended in 1 mL of ferrofluids were injected into inlet A of a FCS device at a flow rate of 6 mL h^{-1}. After separation, cells from outlet 6 were collected and washed with phosphate buffered saline (PBS; Life Technologies, Carlsbad, CA) three times. Cells were then incubated with working solution (2 μM calcein-AM and 4 μM ethidium homodimer-1 (EthD-1)) for 30 minutes at room temperature. After the solution was removed and washed with PBS, labeled cells were observed under a fluorescence microscope (Carl Zeiss, Germany) for counting.

For long-term proliferation, separated H1299 cells from a FCS device were collected into a centrifuge tube and washed three times with culture medium to remove the nanoparticles, and then the cells were suspended in culture medium and seeded into a 24-well plate (Corning Inc., Corning, NY). Cells were then cultured at 37 °C under a humidified atmosphere of 5% CO_2, the medium was refreshed every 24 h during the first 3 days. Cellular morphology was inspected every 24 hours.

Surface biomarker expression change was studied by immunofluorescence staining of cancer cells with EpCAM and cytokeratin antibodies. HCC1806 cancer cells were collected after FCS and seeded on a coverslip. After 24-h incubation, cells were fixed with 4% (w/v) PFA for 30 minutes and subsequently permeabilized with 0.2% (v/v) Triton X-100 (Sigma-Aldrich, St. Louis, MO) in PBS for 10 minutes. Cells were then blocked by 0.5% (w/v) bovine serum albumin (BSA; Miltenyi Biotec, San Diego, CA) in PBS for 20 minutes. After blocking nonspecific binding sites, cells were immunostained with primary antibodies, anti-cytokeratin 8/18/19 (Abcam, Cambridge, MA), human

EpCAM/TROP-1 (R&D System, Minneapolis, MN). Appropriately matched secondary Alexa Fluor-conjugated antibodies (Life Technologies, Carlsbad, CA) were used to identify cells. Nuclei were stained with 4',6-Diamidino-2-Phenylindole (DAPI; Life Technologies, Carlsbad, CA). After immunofluorescence staining, cells were washed with PBS and stored at 4 °C or imaged with a fluorescence microscope.

5.3.5 FCS Device Calibration and Cell Separation

Microfluidic devices were made of polydimethylsiloxane (PDMS) using standard soft lithography techniques. The thickness of the microfluidic channel was measured to be 52 μm by a profilometer (Veeco Instruments, Chadds Ford, PA). One NdFeB permanent magnet (K&J Magnetics, Pipersville, PA) was embedded into the PDMS channel with their magnetization direction vertical to the channel during the curing stage. The magnet is 5.08 cm in length, 1.27 cm in both width and thickness. Flux density at the center of magnet's surface was measured to be 0.5 T by a Gauss meter (Sypris, Orlando, FL) and an axial probe with 0.381 mm diameter of circular active area. Detailed geometries of device setup can be found in Figure 5.3. Fabricated devices were first flushed by 70% ethanol for 10 minutes at the flow rate of 6 mL h^{-1} and then primed with 1× PBS supplemented with 0.5% (w/v) BSA and 2 mM EDTA (Thermo Fisher Scientific, Waltham, MA) for 10 minutes at the flow rate of 6 mL h^{-1} before each use.[185]

During a typical experiment, a microfluidic device was placed on the stage of an inverted microscope (Carl Zeiss, Germany) for observation and recording. Two fluid inputs were controlled by individual syringe pumps (Chemyx, Stafford, TX) at tunable flow rates. Blood samples were injected into inlet A of a FCS device, sheath flow (ferrofluids) was injected into inlet B. Images and videos of microparticles and cells were

recorded with a high-resolution CCD camera (Carl Zeiss, Germany). After separation, cells were collected in a serpentine collection chamber for cell counting.

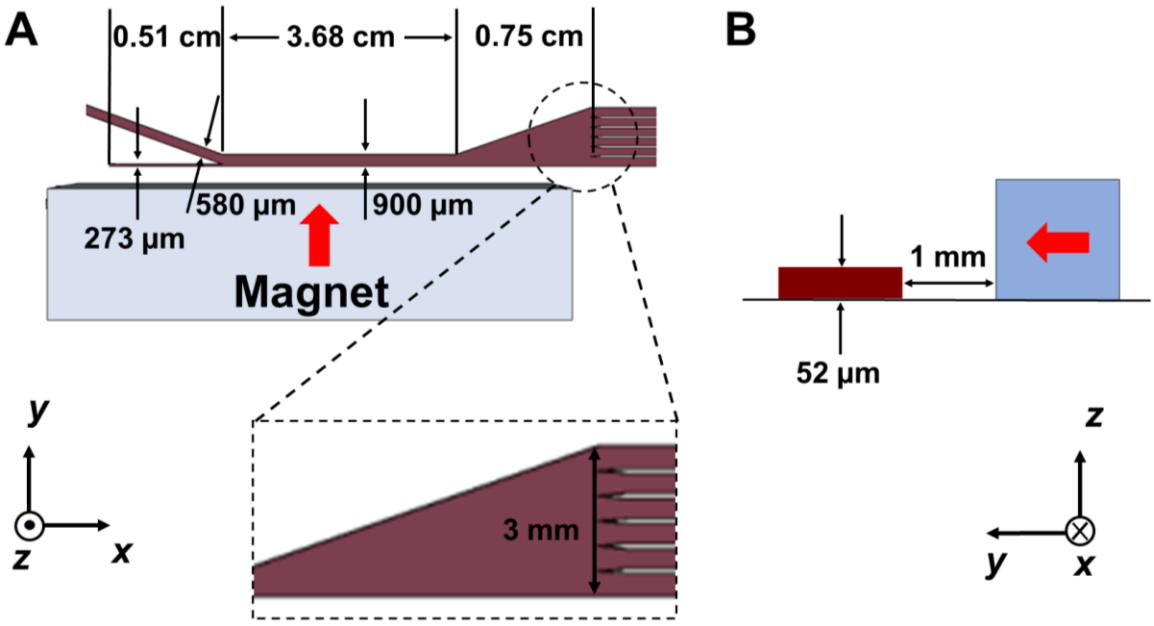

Figure 5.3: Schematic and relevant dimensions of a FCS device. (a) Top-view of the FCS device and relevant dimensions. (b) Cross-section view of the FCS device. The red arrow indicates the direction of permanent magnet's magnetization.

5.3.6 NSCLC Patient Blood Processing

De-identified blood samples were obtained from newly diagnosed advanced NSCLC patients before treatment with informed consents according to a protocol approved by Institutional Review Board (IRB) at Augusta University. All blood samples were collected into vacutainer tubes (BD, Franklin Lakes, NJ,) containing the anticoagulant K_2EDTA and were processed within 3 hours of blood draw. In a typical process, every 1 mL of whole blood was lysed by 10 mL of RBC lysis buffer for 5 minutes at room temperature. WBCs were then collected by spinning down the solution at 800×*g* for 5 minutes and the pellet was suspended in 1 mL of ferrofluid containing

0.1% (v/v) Pluronic F-68. The sample was then loaded into a 10-mL syringe (BD, Franklin Lakes, NJ,) followed by processing with the FCS device at a flow rate of 6 mL h^{-1}. A stainless-steel sphere (BC Precision, Chattanooga, TN) with a diameter of 1.6 mm was also loaded into a syringe. A magnet was used to gently agitate the sphere to prevent blood cells from settling down every 5-10 minutes. After separation, the FCS device was flushed by PBS or ThinPrep PreservCyt solution (Hologic, Marlborough, MA) at 30 mL h^{-1} for 20 minutes to remove any cells in outlet reservoir. During the separation, the cells from outlet 6 of a FCS device were directly preserved in ThinPrep PreservCyt solution for further analysis.

5.3.7 CTC Identification

After processing of blood with a FCS device, collected cells were preserved in ThinPrep PreservCyt solution. Samples collected in ThinPrep vials were directly loaded into ThinPrep 2000 processor (Hologic, Marlborough, MA), which is an automated slide-processing instrument that was routinely used in cytology laboratory for preparing gynecologic and non-gynecologic samples. The instrument transferred diagnostic cells in the sample to a slide that was then immersed in cell fixative bath ready for staining. Papanicolaou (Pap) staining of the slides was performed using Shandon Gemini stainer (Thermo Fisher Scientific, Waltham, MA) followed by cover-slipping using permount. ThinPrep slides were afterwards evaluated by a cytopathologist using light microscopy to identify and count the number of CTCs. Collected cells were also fixed with 4% (w/v) PFA for 30 minutes and subsequently permeabilized with 0.2% (v/v) Triton X-100 in PBS for 10 minutes. Cells were then blocked by 0.5% (w/v) BSA in PBS for 20 minutes. After blocking nonspecific binding sites, cells were immunostained with primary

antibodies, anti-cytokeratin 8/18/19, human EpCAM/TROP-1, and anti-CD45 (Abcam, Cambridge, MA). Following, the appropriately matched secondary Alexa Fluor-conjugated antibodies (Life Technologies, Carlsbad, CA) were used to identify cells. After immunofluorescence staining, cells were washed with PBS and stored at 4 °C or imaged with a fluorescence microscope.

5.4 Results and Discussion

5.4.1 Optimization of FCS for High-Throughput, High-Recovery and Biocompatible CTC Separation

Previous ferrohydrodynamic cell sorting devices were developed to process cells at low throughput and high spike ratios,[38, 44, 95, 201] therefore cannot be realistically used to separate CTCs from blood. CTCs are extremely rare in the blood circulation, occurring usually at a concentration of less than 100 CTCs per mL of blood.[130, 164, 165] These cells are dispersed in a background of billions of RBCs and millions of WBCs, making the separation of CTCs a significant challenge. For any CTC separation method, it is necessary for it to be able to process several milliliters of blood within one hour with a high CTC recovery rate to enrich sufficient numbers of viable CTCs. Thus, high-throughput, high recovery rate, reasonable purity and biocompatible separation of viable CTCs are four criteria for any separation method targeting clinical applications. For ferrohydrodynamic cell separation (FCS) method, the parameters that will affect the above-mentioned criteria include device geometry, magnetic field and its gradient, flow rate of cells, and ferrofluid properties (i.e., magnetic volume fraction or concentration, pH, tonicity, materials and surfactants of nanoparticles, colloidal stability). These parameters are highly coupled with each other and for this reason an effective model was

needed for systematic device optimization. To search for parameters for high-throughput, high recovery rate, reasonable purity and biocompatible CTC separation, we first started with a device geometry depicted in Figure 5.1d that operated in low Reynolds number laminar flow region when its cell flow rates were from 1.2 to 7.2 mL h^{-1}. The corresponding Reynolds numbers were from 0.5 to 3.1, and the upper limit of this flow rate range was close to the clinically relevant throughput in typical CTC separation. We then created an analytical model that could predict three-dimensional (3D) trajectories of cancer cells and blood cells in ferrofluids inside this device coupled with a permanent magnet. We considered both magnetic buoyancy force and hydrodynamic drag force in simulating the cell trajectories.

The dominant magnetic force in ferrohydrodynamic cell sorting (FCS) is a magnetic buoyancy force generated on diamagnetic cells immersed in ferrofluids. Particles immersed in ferrofluids experience this force under a non-uniform magnetic field,[27]

$$\vec{F}_m = \mu_0 V_c \left[\left(\vec{M}_c - \vec{M}_f \right) \cdot \nabla \right] \vec{H} \tag{5.1}$$

where $\mu_0 = 4\pi \times 10^{-7}$ H m^{-1} is the permeability of free space, V_c is the volume of the magnetized body, in this case a cell, $\vec{M}_c$ is its magnetization (close to zero for most cells), $\vec{M}_f$ is magnetization of the ferrofluid surrounding the body, and $\vec{H}$ is magnetic field strength at the center of the body.[27] For cell separation in ferrofluids under a strong magnetic field, magnetization of the ferrofluid with superparamagnetic particles in it can be modeled via Langevin function,[27]

$$\frac{\vec{M}_f}{\phi_f \vec{M}_{f,b}} = L(\alpha_f) = \coth(\alpha_f) - \frac{1}{\alpha_f} \tag{5.2}$$

where $a_f = \pi\mu_0 M_{f,b} H d_f^3 / 6 k_B T$, f_f is the volume fraction of the magnetic materials in ferrofluids, [27] $M_{f,b}$ is saturation moment of the bulk magnetic materials, and d_f is the diameter of nanoparticles in a ferrofluid. k_B is the Boltzmann constant, *T* is temperature. In ferrohydrodynamic cell sorting, the magnetization of the cell $\vec{M}_p$ is less than its surrounding magnetic liquid $\vec{M}_f$, and the direction of the magnetic force $\vec{F}_m$ on the cell is pointing towards magnetic field minima.

The hydrodynamic viscous drag force exerted on diamagnetic cell takes the form,

$$\vec{F}_d = -3\pi\eta D_c \left(\vec{U}_c - \vec{U}_f\right) f_D \tag{5.3}$$

where η is the viscosity of ferrofluids, D_c is the diameter of the cell, $\vec{U}_c$ and $\vec{U}_f$ are the velocity vectors of the cell and ferrofluids respectively, f_D is the hydrodynamic drag force coefficient for a cell moving near a solid surface, often referred to as the "wall effect".[48, 50, 202] Because of the low Reynolds number in FCS devices, inertial effects on the cell were neglected and motion of cells in ferrofluids could be determined by the balance of hydrodynamic viscous drag force and magnetic buoyancy force. From Equations 4.1-4.3, it can be seen that cells with different volumes experience different magnitudes of magnetic buoyancy force, which can result in the separation of these cells in ferrofluids in a continuous-flow manner.

We first confirmed the validity of the model by comparing simulated trajectories (Figure 5.4) with experimental ones (Figure 5.5) that were obtained from imaging 15.6-μm-diameter polystyrene beads and 11.1-μm-diameter WBCs in a FCS device, as shown in Figure 5.6. We then used the model to optimize the FCS device for CTC separation. The optimization was focused on the study of separating cancer cells from WBCs,

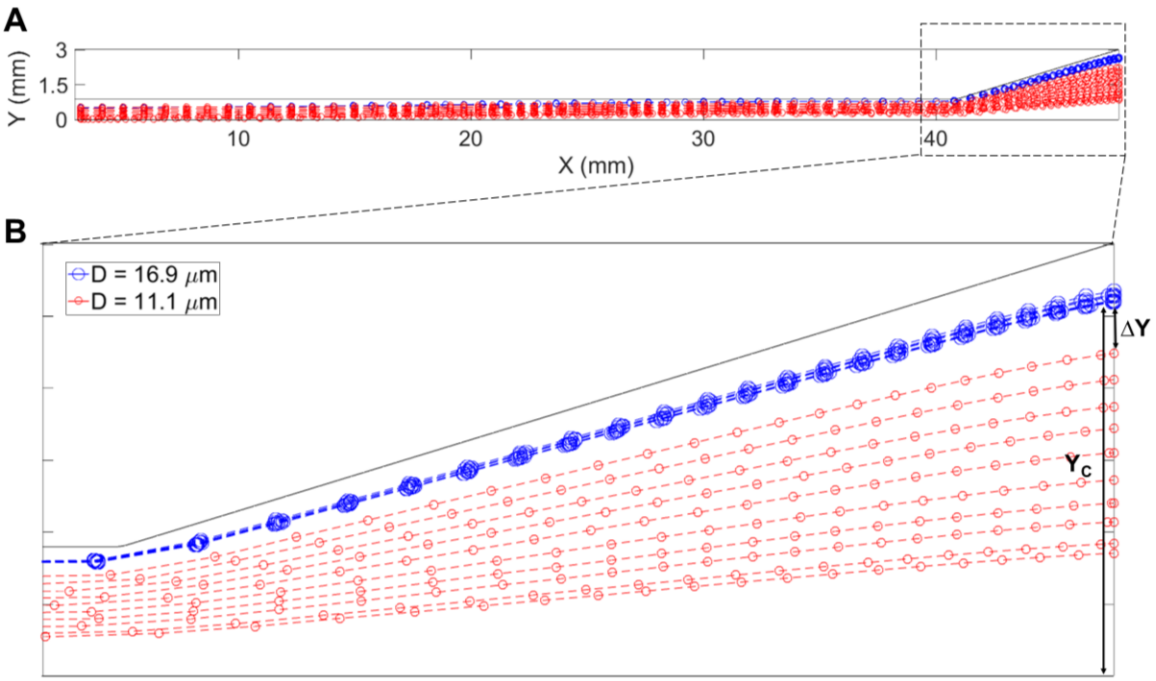

Figure 5.4: (a) Cell trajectory simulation of H1299 lung cancer cell (16.9 μm) and WBCs (11.1 μm) in a FCS device. (b) Zoomed-in view of cell trajectories at the end of FCS device. Blue and red trajectories indicate H1299 and WBCs, respectively. Flow rate of cell inlet (Inlet A) was fixed at 6 mL h^{-1}, ferrofluid concentration was fixed at 0.26% (v/v), and magnetic field was fixed at 443 mT and its gradient was fixed at 56.2 T m^{-1} for this simulation.

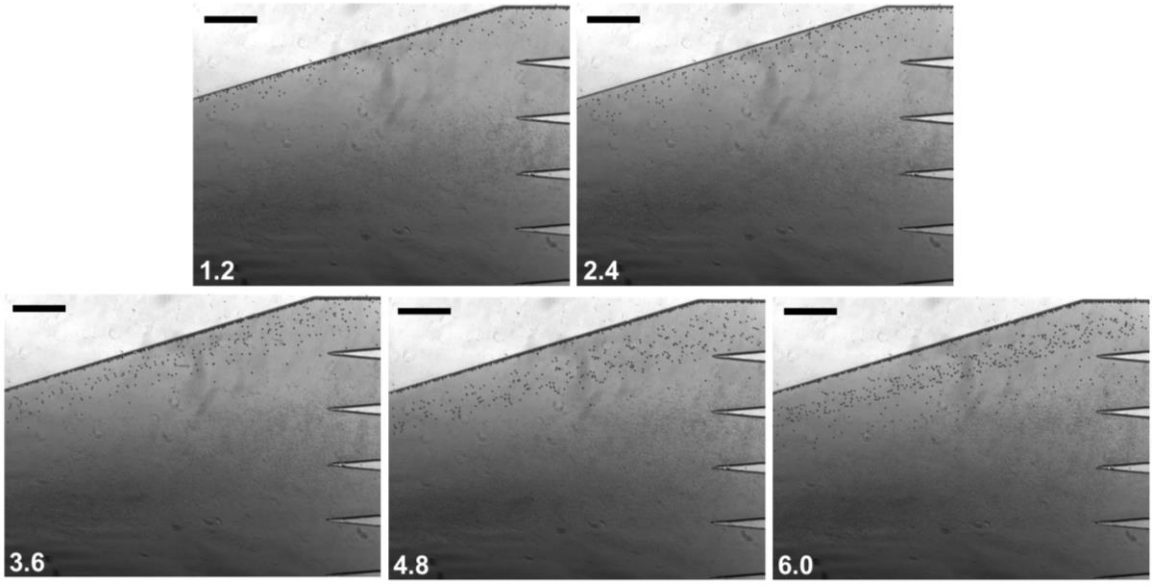

Figure 5.5: FCS device calibration with H1299 cells (replaced with beads of similar size, 15.6 μm) and WBCs (11.1 μm). The left-bottom number in each figure indicates the

associated flow rate of cell inlet A (mL h^{-1}). Flow rate of cell inlet (Inlet A) was fixed at 6 mL h^{-1}, ferrofluid concentration was fixed at 0.26% (v/v), and magnetic field was fixed at 443 mT and its gradient was fixed at 56.2 T m^{-1} for this calibration. ~1×10^4 polystyrene microparticles were mixed with 1 mL of undiluted WBCs. Scale bars: 500 µm.

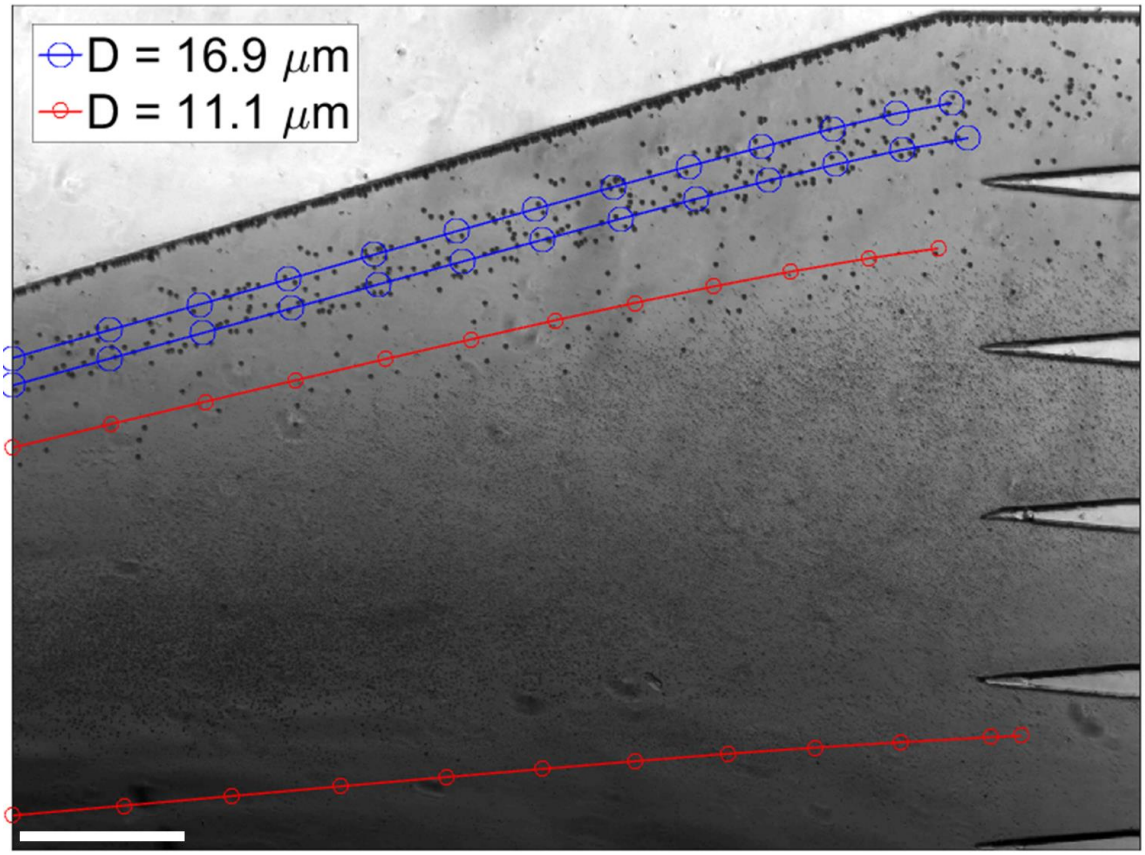

Figure 5.6: Comparison of cell trajectories from calibration experiments and simulations of H1299 cells and WBCs at the end of FCS device. Blue lines are the boundary of the simulated H1299 cell trajectory, and red lines are the boundary of the simulated WBC trajectory. The simulated trajectories considered the initial width of microparticle and cell streams at the entry of the channel, therefore had an up and low bound of trajectories. Overall the simulated trajectories matched well with the experimental calibration trajectories, therefore could be used for subsequent FCS device optimization. Flow rate of cell inlet (Inlet A) was fixed at 6 mL h^{-1}, ferrofluid concentration was fixed at 0.26% (v/v), and magnetic field was fixed at 443 mT and its gradient was fixed at 56.2 T m^{-1} for simulation and calibration. Scale bar: 500 µm.

because of their subtle size difference. Briefly, we allowed cancer cells and WBCs (H1299 lung cancer cells with a mean diameter of 16.9 µm, and WBCs with a mean

diameter of 11.1 μm) to enter the channel and simulated their trajectories in ferrofluids under external magnetic fields. From their simulated trajectories, we calculated two outputs – a deflection in the *y*-direction (see Figure 5.1 and Figure 5.3) for cancer cells, denoted as Y_C, and a separation distance between the two types of cells, denoted as ΔY (Figure 5.4). Both outputs were optimized using parameters including flow rates of cell inlet (1.2-7.2 mL h^{-1}), magnetic fields and gradients (field: 471-415 mT; gradient: 57.1-54.6 T m^{-1}, as shown in Figure 5.2), and ferrofluid concentrations (up to 1% v/v). The goal here was to achieve high cell flow rate, cancer cell recovery rate and recovered cancer cell purity, which translated to maximizing both Y_C and ΔY simultaneously. Figure 5.7a shows when the magnetic field gradient increased, the deflection distance of cancer cells Y_C increased monotonically for all flow rates. This was because the driving force, magnetic buoyancy force on cells, was proportional to the magnitude of magnetic field gradient. As the cell inlet flow rate increased, Y_C decreases due to reduced time in the channel. Figure 5.7b shows similar trend of separation distance ΔY increasing as the field gradient increased when flow rates are 4.8, 6.0 and 7.2 mL h^{-1}. Interestingly, when cell input flow rates are smaller (*e.g.*, 1.2, 2.4 and 3.6 mL h^{-1}), the separation distance ΔY between two cell types had different trends. This was due to the fact that both cell types at slower flow rates reached their maximum deflections very quickly, resulting in a mixing rather than separation of the two types. For practical CTC separation, we chose a cell flow rate of 6 mL h^{-1} and a magnetic field gradient of 56.2 T m^{-1} that could be generated realistically through magnet and channel integration in a FCS device to achieve high-throughput and high recovery rate cell separation. It should be noted here that the optimization was conducted on a single-channel device, and higher cell flow rates and

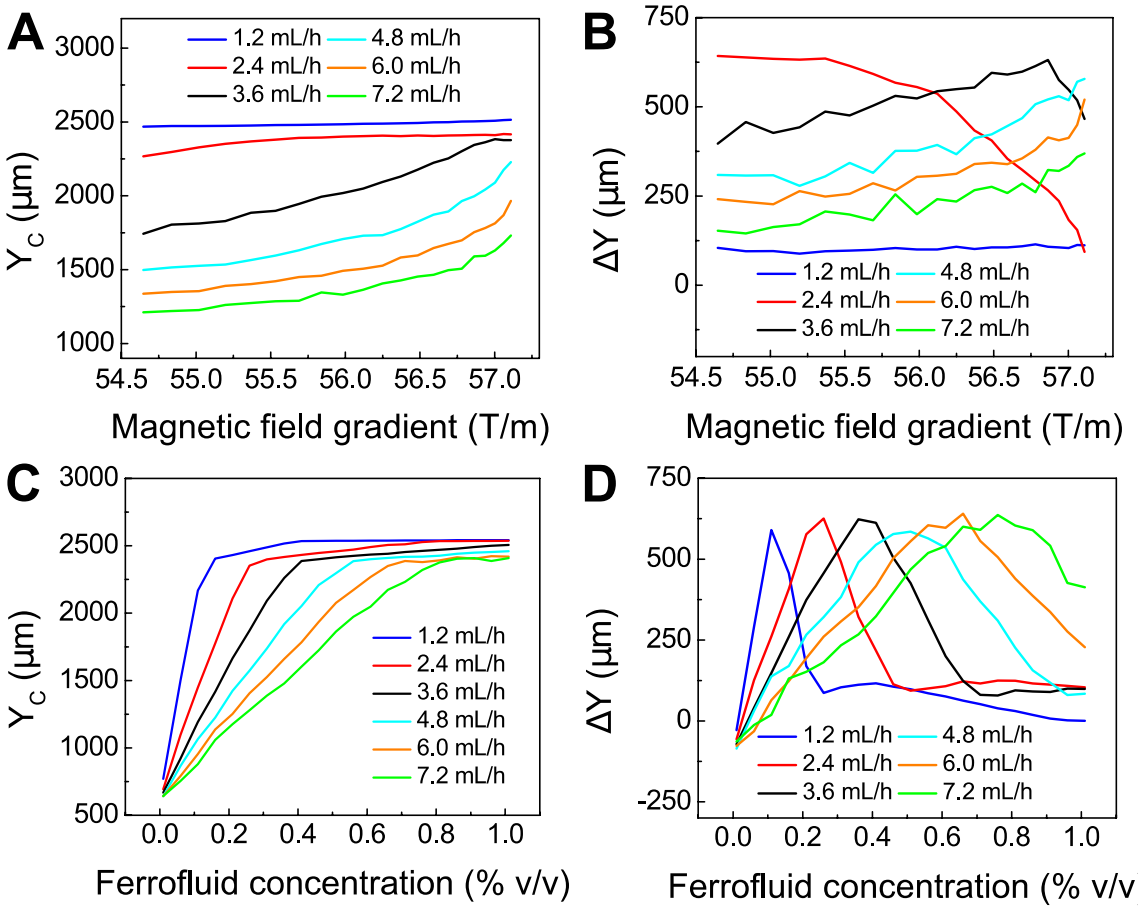

Figure 5.7: Optimization of FCS devices with their device geometry shown in Figure 5.1 for high-throughput, high-recovery and biocompatible CTC separation. A 3D analytical model considering magnetic buoyancy force, hydrodynamic drag force, laminar flow profiles and cancer/blood cell physical properties was developed to guide the optimization. The validity of the model was confirmed by comparing its simulated trajectories with experimental ones. Numerical optimization of deflection distance Y_C and separation distance ΔY (corresponding to recovery rate and purity) at the end of the FCS device was conducted with parameters including: (a) & (b) magnetic field gradient, and (c) & (d) ferrofluid concentration at flow rates between 1.2 and 7.2 mL h^{-1}. Ferrofluid concentration was fixed at 0.26% (v/v) for (a) & (b). Magnetic field was fixed at 443 mT and its gradient was fixed at 56.2 T m^{-1} for (c) & (d).

throughputs were possible with device scale-up or multiplexing.

After optimizing flow rate and magnetic field gradient, another critical parameter that still needs to be optimized is the ferrofluid itself. Ideally, the ferrofluid needs to possess properties that are not only biocompatible to CTCs but also enable its colloidal

stability under high flow rates and strong magnetic fields. Therefore, its pH value, tonicity, materials and surfactants of nanoparticles need to be optimized as a biocompatible medium for cells, while at the same time the overall colloidal stability of the ferrofluid will have to be well maintained. Based on our previous work,[95, 201] we have developed a water-based ferrofluid with maghemite nanoparticles in it that was tested to be biocompatible for cancer cells from cultured cells lines. The particles had a mean diameter of 11.24 nm with a standard deviation of 2.52 nm. The diameter of the nanoparticles was chosen to preserve the colloidal stability of ferrofluids against agglomeration due to gravitational settling and magnetic dipole-dipole attraction. As a result, our ferrofluids remained colloidally stable after at least 10 months' storage. The nanoparticles were functionalized with a graft copolymer as surfactants to prevent them from coming too close to one another when there was a magnetic field. The volume fraction of the magnetic content of the ferrofluid is 0.26%. This low volume fraction of the ferrofluid not only leaded to excellent biocompatibility for cell sorting, but also enabled us to observe cell motion in microchannel directly with bright-field microscopy, which was difficult with opaque ferrofluids of high solid volume fractions. The ferrofluid was made to be isotonic and its pH was adjusted to 7.0 for biocompatible cell separation. We further optimized the ferrofluid concentration for high-throughput and high recovery separation. From Equation 5.1, the magnetic buoyancy force depends on the magnetization of the ferrofluid and affects the cell separation outcome. Therefore, the concentration of ferrofluid had an impact on the process of cell separation. A higher concentration could lead to a higher magnitude of magnetic buoyancy force on cells and a larger deflection Y_C (Figure 5.7c), but not necessarily a larger ΔY (Figure 5.7d). Figure

5.7d shows there was an optimal ferrofluid concentration close to 0.6% (v/v) at 6.0 mL h^{-1} flow rate for ΔY. Concentrations higher than 0.6% (v/v) resulted in larger Y_C but smaller ΔY. This again was because both cell types achieved sufficient deflections in a strongly magnetized ferrofluid, resulting in mixing rather than separation of the two. In addition, ferrofluid biocompatibility could be compromised as its nanoparticle concentration increases.[201] Based on these considerations, we chose a 0.26% (v/v) ferrofluid concentration to strike a balance between high-recovery and biocompatible cell separation at a flow rate of 6 mL h^{-1}.

5.4.2 Verification of FCS for High-Throughput and High-Recovery Spiked Cancer Cell Separation

We performed experimental verification of high-throughput, high-recovery and biocompatible separation of spiked cancer cells of cultured cell lines from WBCs based on the optimal parameters obtained from simulation and calibration. During separation experiments, a permanent magnet was placed 1 mm away from the channel (magnetic field: 443 mT, magnetic field gradient: 56.2 T m^{-1}), and ferrofluids with a concentration of 0.26% (v/v) were used. We first studied the CTC recovery rate at different flow rates using spiked H1299 lung cancer cells in WBCs. The concentration of WBCs was 3-7×10^6 cells mL^{-1}; CTCs were simulated by spiking ~100 CellTracker Green stained H1299 cancer cells into 1 mL of WBCs. The cells were loaded into a FCS device at variable flow rates of 1.2-6 mL h^{-1} for recovery rate evaluation. Figure 5.8 shows a typical cancer cell (Lung cancer H1299) separation process in the FCS device. When the magnetic field was not present, all cell types including cancer cells and WBCs were flowing near the bottom sidewall of the channel and exiting through outlets 1 and 2 (Figure 5.8a). When

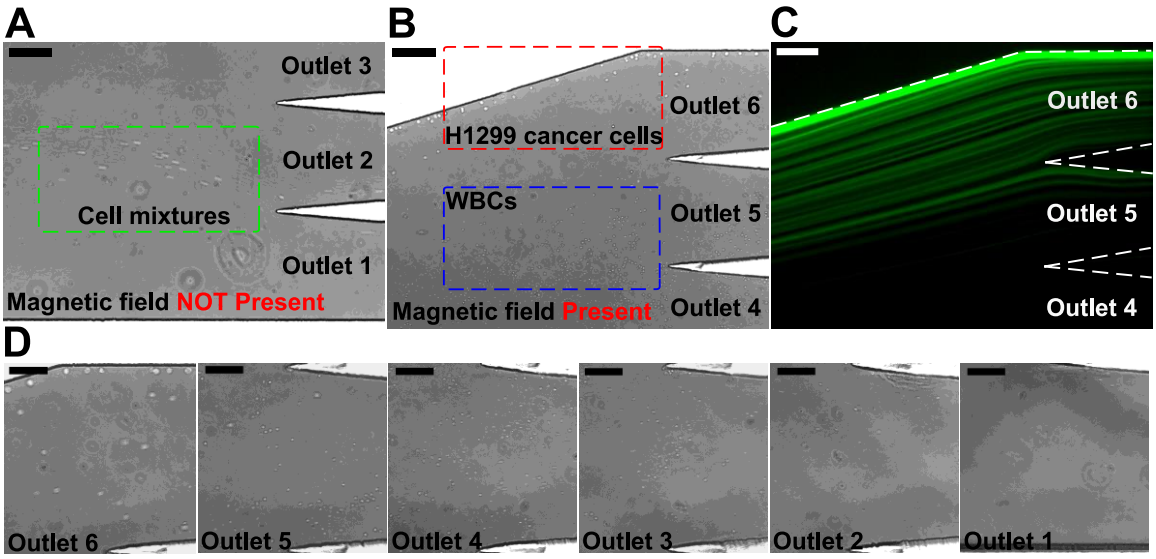

Figure 5.8: Micrographs of spiked cancer cells of cell culture lines and undiluted WBCs separation process in a FCS device. In order to image the separation process, 1×10^5 cells H1299 lung cancer cells were spiked into 1 mL of undiluted WBCs to increase the cancer cell concentration so that their fluorescent signals were visible. The cell mixture was processed at the flow rate of 6 mL h^{-1}. A ferrofluid with its concentration of 0.26% (v/v) was used; magnetic field was fixed at 443 mT and its gradient was fixed at 56.2 T m^{-1}. (a) In absence of magnetic fields, cell mixtures exited the channel through outlets 1 and 2. Scale bar: 200 µm. (b) When magnetic fields were present, larger H1299 lung cancer cells and some WBCs were deflected and exited through outlets 5 and 6 (collection outlets), while smaller WBCs exited through lower outlets (outlets 1-4, waste outlets). Scale bar: 200 µm. (c) Fluorescence image of spiked H1299 lung cancer cell streams during the separation process when magnetic fields were present. H1299 cells were stained by CellTracker Green. Scale bar: 200 µm. (d) Zoomed-in bright-field images of outlets 1-6 when the magnetic fields were present. Scale bars: 100 µm.

the magnetic field was present, a separation between cancer cells and WBCs was visible. Magnetic buoyancy forces deflected larger H1299 cancer cells with a mean diameter of 16.9 µm from the cell mixture toward outlets 5 and 6, as shown in Figures 5.8b-d. Meanwhile, magnetic buoyancy forces on WBCs were insufficient to deflect them above outlet 5, resulting in a spatial separation of the cell mixtures at the end of the channel. Cells from outlets 5 and 6 after separation were collected into a serpentine collection chamber as illustrated in Figure 5.9, which was used to accurately enumerate fluorescently labeled cancer cells. Representative images for outlet 6 reservoir and

collection chambers are shown in Figure 5.10. The recovery rate was defined as the ratio of the number of identified cancer cells collected from outlets 5 and 6 of the FCS device over the total number of spiked cancer cells from outlets 1-6.

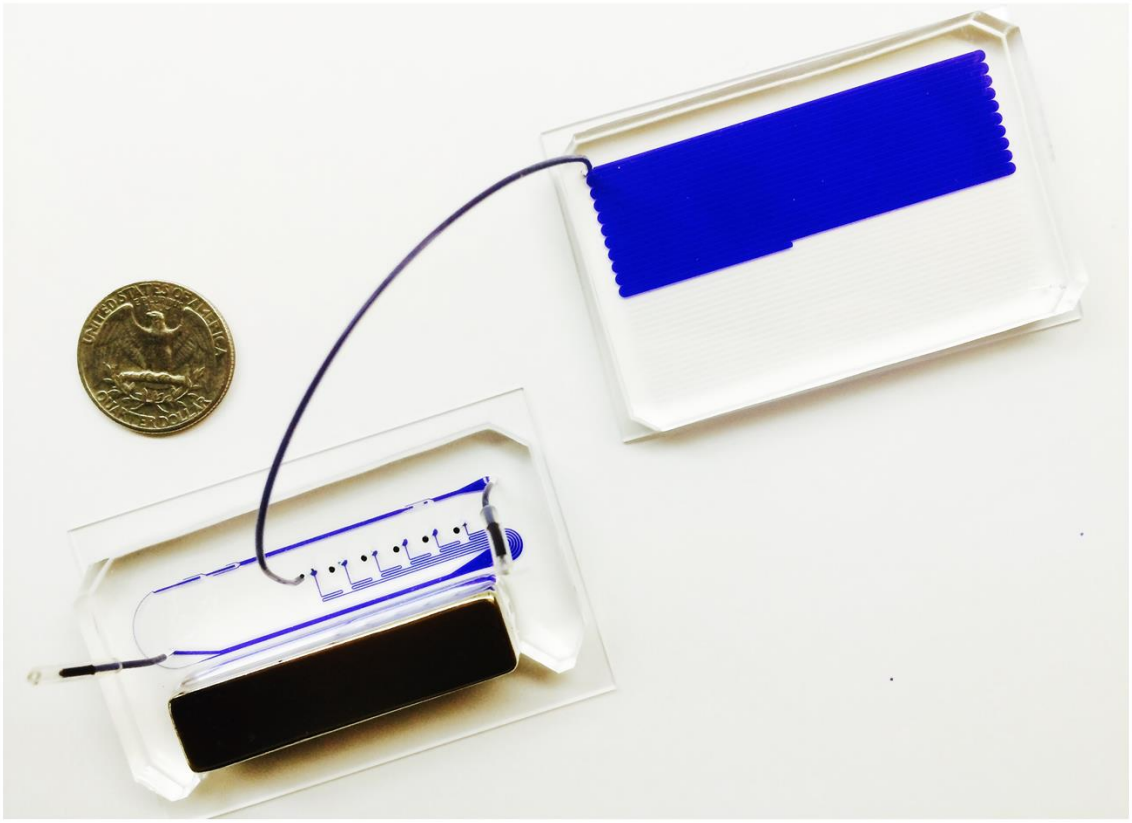

Figure 5.9: An image of a FCS device and an attached collection chamber. The FCS device was connected to a serpentine collection chamber that was used to accurately enumerate cancer cells for the FCS calibration using cultured cancer cell lines. The depth of collection chamber is 50 μm. The size of the glass slide is 75 × 50 mm. Blue dye was used to visualize the microchannel.

Figure 5.11a shows the relationship between cancer cell recovery rates and flow rates for H1299 cancer cells. As flow rates increased from 1.2 mL h^{-1} to 6 mL h^{-1}, recovery rates decreased from 98.6±5.0% to 92.3±3.6%. An average recovery rate of 92.3% was achieved for current FCS devices with a throughput of 6 mL h^{-1} when ~100 H1299 cancer cells were spiked into 1 mL of WBCs. To validate that the device has the

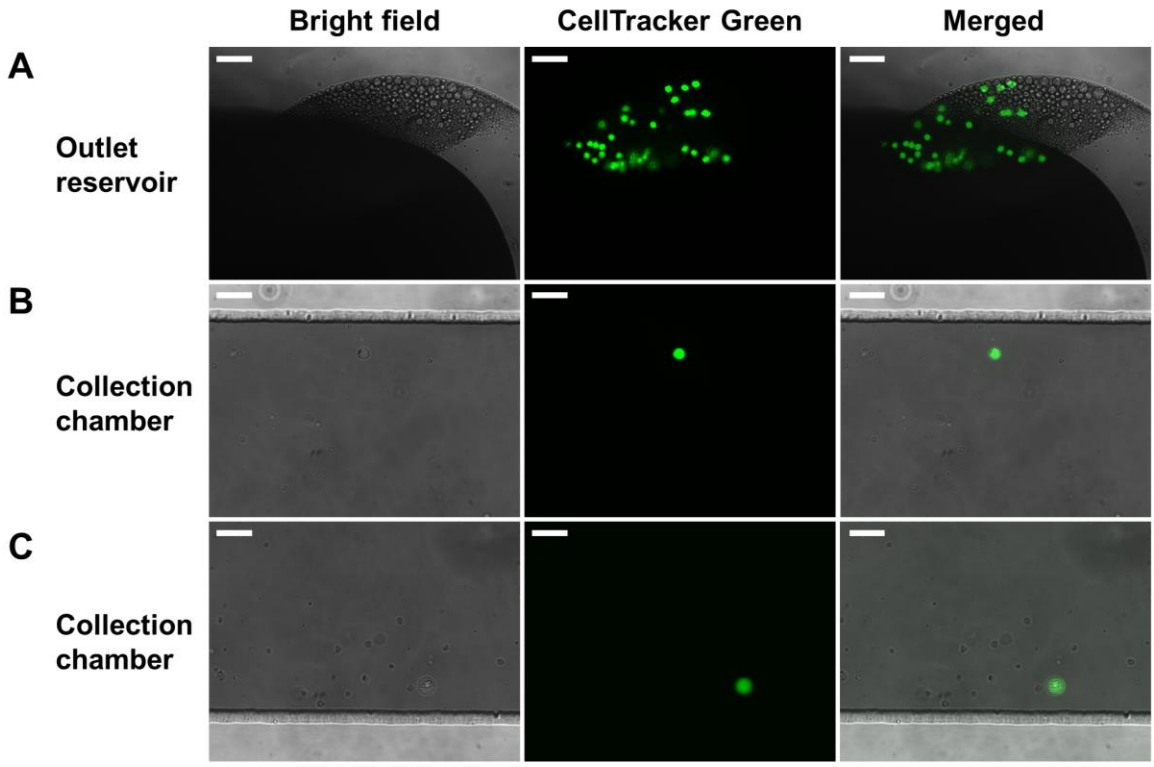

Figure 5.10: Representative micrographs of lung cancer H1299 cells and WBCs after a separation of spiked cancer cells in a FCS device at a throughput of 6 mL h^{-1}. ~100 CellTracker Green stained H1299 cells were spiked into 1 mL of undiluted WBCs. (a) H1299 lung cancer cells and WBCs were identified in the outlet (outlet 6) reservoir. Scale bars: 100 µm. (b) and (c) H1299 lung cancer cells and WBCs were identified in the serpentine collection chamber. Scale bars: 50 µm.

potential to process clinically relevant blood samples, a series of spike-in experiments in which a certain number of H1299 cells (50, 100, 200, 500, 1000, and 2000) were spiked into 1 mL of WBCs. As shown in Figure 5.11b, an average recovery rate of 91.9% was achieved in the FCS device for this particular lung cancer cell line. Figure 5.11c shows the relationship between removal rates of WBCs and cell input flow rates. As the flow rate increased, more WBCs were removed during the separation process. For example, 99.92±2.2% of WBCs were removed at the flow rate of 6 mL h^{-1} when ~100 H1299 cancer cells were spiked into 1 mL of WBCs. The corresponding purity of separated cancer cells was 11.1%±1.2%. The purities of separated cancer cells in other spike-in

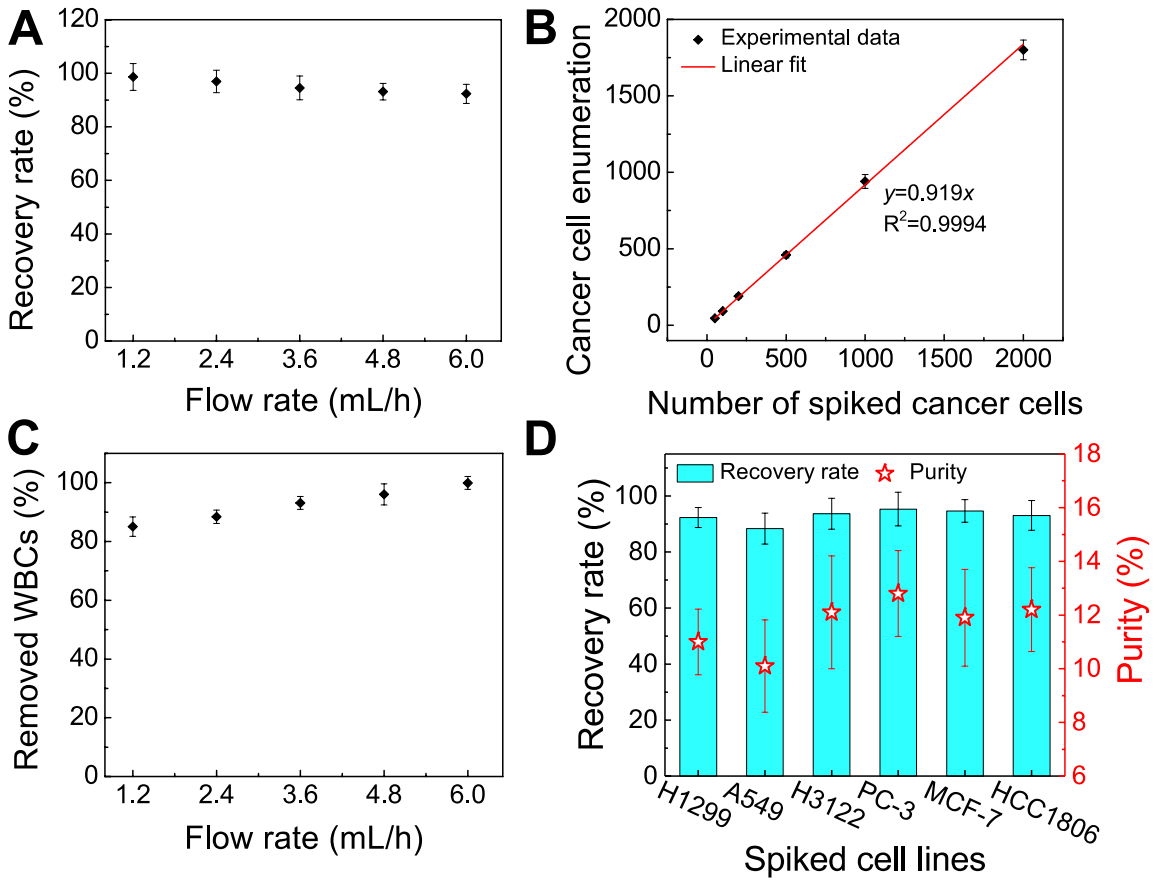

Figure 5.11: Verification of FCS devices for high-throughput and high-recovery spiked cancer cells separation. (a) Recovery rates of spiked H1299 lung cancer cells from undiluted WBCs at flow rates from 1.2 mL h^{-1} to 6.0 mL h^{-1}. ~100 H1299 cancer cells were spiked into 1 mL of undiluted WBCs. Recovery rates decreased from 98.6±5.0% to 92.3±3.6% when flow rate increased from 1.2 mL h^{-1} to 6.0 mL h^{-1}. (b) A series of spike-in separation experiments in which a certain number (50, 100, 200, 500, 1000, and 2000) of H1299 cells were spiked into 1 mL of undiluted WBCs to simulate clinically relevant CTC concentration at the flow rate of 6.0 mL h^{-1}. An average recovery rate of 91.9% (linear fit, the coefficient of determination R^2=0.9994 was calculated between the number of cells counted and the number of cells spiked) was achieved for H1299 lung cancer cells. (c) The removal rate of WBCs increased with the flow rate. 99.92±2.2% of WBCs were removed at a flow rate of 6 mL h^{-1}. ~100 H1299 cancer cells were spiked into 1 mL of undiluted WBCs. (d) Recovery rates and purity of separated cancer cells (~100 cell mL^{-1}) for different cancer cell lines at the flow rate of 6 mL h^{-1}. Recovery rates of 92.3±3.6%, 88.3±5.5%, 93.7±5.5%, 95.3±6.0%, 94.7±4.0%, and 93.0±5.3% were achieved for H1299 (lung cancer), A549 (lung cancer), H3122 (lung cancer), PC-3 (prostate cancer), MCF-7 (breast cancer), and HCC1806 (breast cancer) cell lines, respectively. The corresponding purities of cancer cells of each cell line are 11.1±1.2% (H1299), 10.1±1.7% (A549), 12.1±2.1% (H3122), 12.8±1.6% (PC-3), 11.9±1.8 (MCF-7), and 12.2±1.6% (HCC1806), respectively. For all experiments above, a ferrofluid with its

concentration of 0.26% (v/v) was used; magnetic field was fixed at 443 mT and its gradient was fixed at 56.2 T m^{-1}. Error bars indicate standard deviation (s.d.), n=3.

experiments were 4.8%-67.4% (4.8±1.6%, 20.3±2.8%, 31.2±4.7%, 41.7±4.9%, and 67.4±3.3% when 50, 200, 500, 1000, and 2000 H1299 cancer cells were spiked into 1 mL of WBCs). The purity was defined as the number of identified cancer cells over the total number of cells from FCS device's collection outlets. As the number of spiked cells increased, the number of separated cancer cells also increased, which leaded to a higher purity value. The cell type distribution in each outlet is illustrated in Figure 5.12.

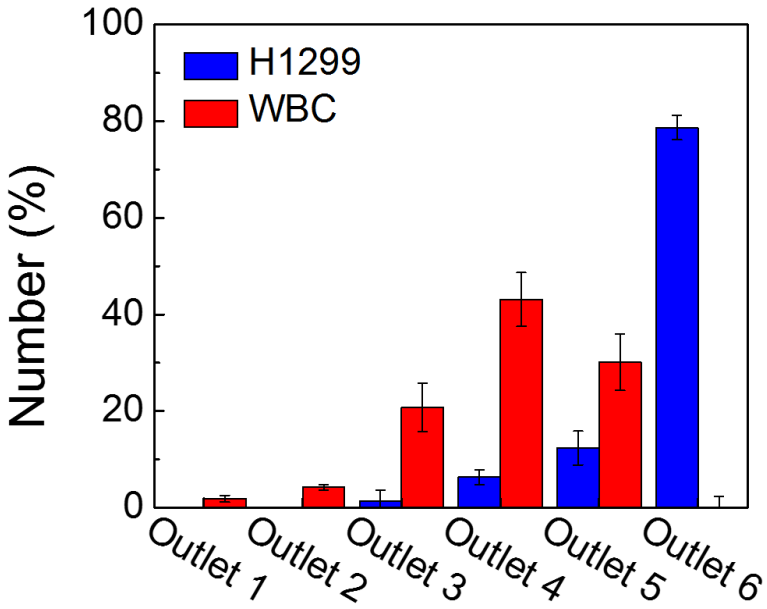

Figure 5.12: Cell type distribution of cells collected from outlets 1-6 after a separation of ~100 H1299 cells spiked into 1 mL of undiluted WBCs using a FCS device at a throughput of 6 mL h^{-1}.

After successfully demonstrating low-concentration cancer cell separation using H1299 lung cancer cell line, we also characterized the FCS device with 5 other types of cancer cells lines. Size distribution of CTCs from clinical samples is unknown, it is

therefore important to characterize the performance of FCS devices with cancer cell culture lines with different sizes. For this purpose, lung cancer, prostate cancer, and breast cancer cell culture lines were used to characterize the cancer cell recovery rates at 6 mL h^{-1} throughput with a ~100 cells mL^{-1} spike ratio. As shown in Figure 5.11d, the average recovery rates of 88.3±5.5%, 93.7±5.5%, 95.3±6.0%, 94.7±4.0%, and 93.0±5.3% were achieved for A549 (lung cancer), H3122 (lung cancer), PC-3 (prostate cancer), MCF-7 (breast cancer), and HCC1806 (breast cancer) cell lines, respectively. The corresponding purities of separated cancer cells for each cell line were 10.1±1.7% (A549), 12.1±2.1% (H3122), 12.8±1.6% (PC-3), 11.9±1.8% (MCF-7), and 12.2±1.6% (HCC1806), confirming the robustness of the FCS device for cancer cell separation. The recovery rate increased as the mean cell size of cancer cells increased (Table 5.1 and Figure 5.13), which was expected as FCS was based on size difference of cell types. In

Table 5.1: Rare cell separation with spiked cancer cells from cultured cell lines. ~100 cancer cells were spiked into 1 mL of undiluted WBCs ($3\text{-}7\times10^6$ cells mL^{-1}). The recovery rate was defined as the ratio of the number of identified cancer cells collected from collection outlets (outlets 5 and 6) over the total number of spiked cancer cells from all outlets. The purity was defined as the number of identified cancer cells over the total number of cells from FCS device's collection outlets. Waste outlets were outlet 1-4. Data are expressed as mean ± standard deviation (s.d.), n=3.

Cancer cell line	Cancer cell type	Measured average cell diameter (μm)	No. of spiked cancer cells	No. of cells (collection outlets)	No. of cells (waste outlets)	Recovery rate	Purity
A549	Lung	15.5	99 ± 2	89 ± 4	10 ± 6	88.3±5.5%	10.1±1.7%
H1299	Lung	16.9	99 ± 3	91 ± 1	8 ± 4	92.3±3.6%	11.1±1.2%
HCC1806	Breast	17.6	100 ± 4	93 ± 4	7 ± 4	93.0±5.3%	12.2±1.6%
H3122	Lung	17.8	101 ± 4	92 ± 6	9 ± 4	93.7±5.5%	12.1±2.1%
MCF-7	Breast	18.7	100 ± 3	94 ± 3	6 ± 3	94.7±4.0%	11.9±1.8%
PC-3	Prostate	18.9	100 ± 7	95 ± 7	5 ± 7	95.3±6.0%	12.8±1.6%

summary, we experimentally verified that the optimized FCS device was capable of separating cancer cells from WBCs with a flow rate of 6 mL h^{-1}, with a cancer cell recovery rate of 92.9% and a separated cancer cell purity of 11.7% averaged from all 6 cancer cell lines at ~100 cells mL^{-1} spike ratio, which allowed us to use the devices to process the clinical samples.

A

Cell type	Average cell size (μm)
H1299	16.9
A549	15.5
H3122	17.8
PC-3	18.9
MCF-7	18.7
HCC1806	17.6
WBC	11.1

B

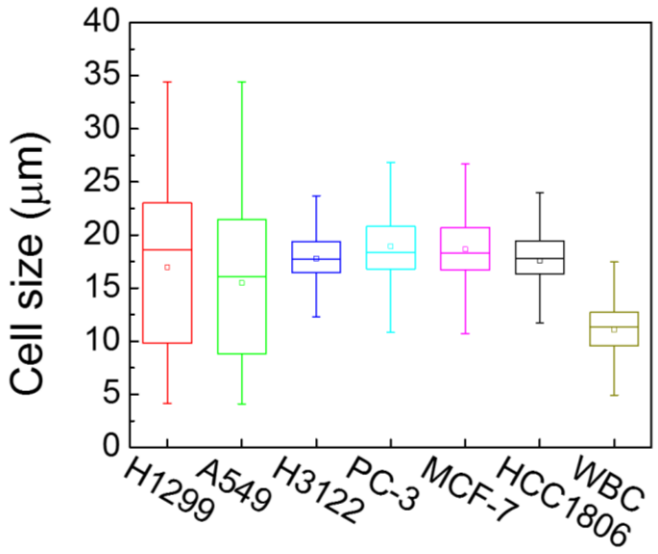

Figure 5.13: (a) The average cell size of six cancer cell lines and WBCs measured by a cell counter. (b) Size distribution of cancer cells and WBCs.

5.4.3 Effect of FCS on Cancer Cell Viability, Proliferation and Biomarker Expressions

As discussed above, the operating parameters of the FCS device need to preserve cell integrity during its cell separation process. To investigate the impact of ferrofluids and current separation conditions on cell integrity, we examined short-term cell viability, long-term cell proliferation, as well as biomarker expression of cancer cells following the separation process.

The short-term viability of cancer cells in ferrofluids was first evaluated by 3-(4,5-dimethylthiazol-2-yl)-2,5-diphenyl-tetrazolium bromide (MTT) assay for 12-h incubation with different concentrations of ferrofluids. The results show that H1299 lung cancer cells had a cell viability of 80.8±2.4% after 12-h incubation with 0.26% (v/v) ferrofluids. Next, we investigated the short-term cell viability after ferrohydrodynamic cell separation using a Live/Dead assay. Cells in 1 mL of ferrofluids (1×10^6 H1299 cells) were processed by the FCS device at a flow rate of 6 mL h^{-1}. The device-operating parameters were chosen to be the same as those used in aforementioned cancer cell separation experiments. After running the cell sample through the device, cancer cells collected from outlet 6 were stained with 2 μM calcein-AM and 4 μM EthD-1 for 30 minutes at room temperature to determine their viability. Cells with a calcein-AM+/EthD-1– staining pattern were counted as live cells, whereas cells with calcein-AM–/EhD-1+ staining patterns were counted as dead cells. As shown in Figure 5.14a, cell viability of H1299 cells before and after separation groups were determined to be 98.9±0.9% and 96.3±0.9%, respectively, indicating a very slight decrease in cell viability before and after the ferrohydrodynamic separation process. Representative fluorescence images of cells are shown in Figure 5.14b.

After determining short-term cell viability, we examined whether separated cancer cells continued to proliferate normally after the separation process. To simulate the actual separation conditions, 1×10^6 H1299 cells were spiked into 1 mL of ferrofluids and passed through the FCS device. The flow rate and ferrofluid concentration were chosen to be the same as those used in cancer cell separation experiments. Following cell collection, the recovered H1299 cells were washed with culture medium to remove

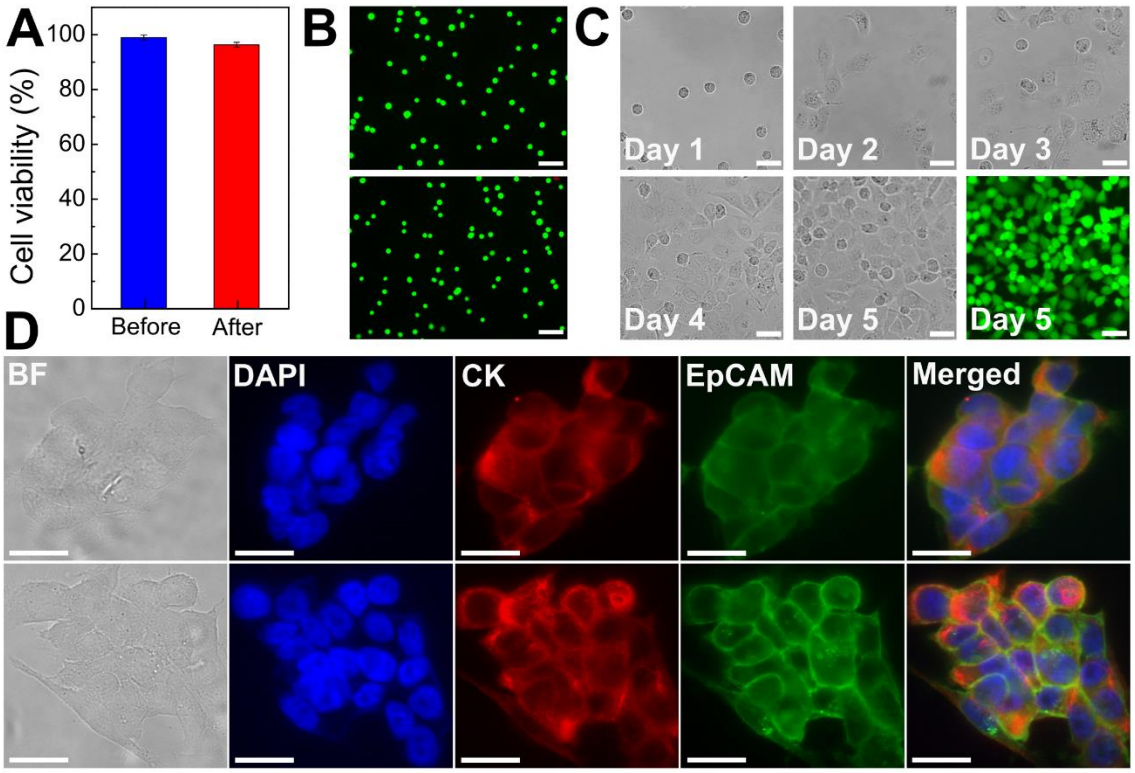

Figure 5.14: Effect of FCS on cancer cell viability, proliferation and biomarker expressions. (a) Short-term cell viability comparison before and after FCS process using a Live/Dead assay. Cell viabilities of H1299 lung cancer cells before and after separation process were determined to be 98.9±0.9% and 96.3±0.9%, respectively. Error bars indicate standard deviation (s.d.), n=3. (b) Representative images of Live/Dead cell staining for before (top) and after (bottom) separation groups. Calcein AM (green, live cells) and EhD-1 (red, dead cells) channels were merged. Scale bars: 100 µm. (c) Bright field images of cultured H1299 cells collected after separation from day 1 to day 5. A Live/Dead staining of the cultured cells on day 5 showed excellent cell viability. Scale bars: 50 µm. (D) Comparison of expressions of two key biomarkers (epithelial cell adhesion molecule-EpCAM and cytokeratin-CK) on HCC1806 breast cancer cells before (top) and after (bottom) separation. They showed qualitatively similar EpCAM and CK fluorescence. Scale bars: 20 µm.

maghemite nanoparticles and transferred to an incubator. Cells were cultured at 37 ^{o}C under a humidified atmosphere of 5% CO_2. Figure 5.14c shows the images of the cultured H1299 cells over a 5-day period. These cells were able to proliferate to confluence and maintain their morphologies after the ferrohydrodynamic separation

process. Fluorescence image in Figure 5.14c also confirms that cells were viable after the 5-day culture.

In order to determine whether the FCS process would alter the expression of cell surface biomarkers, we looked for changes in biomarker expression using immunofluorescence staining. Specifically, we compared expressions of epithelial cell adhesion molecule (EpCAM) and cytokeratin (CK), two key biomarkers in CTC studies, in paired sets of pre- and post-FCS process. Results shown in Figure 5.14d indicate there was no visible change in either EpCAM or CK expression on HCC1806 breast cancer cells because of the FCS process. Collectively, the short-term viability, long-term cell proliferation and biomarker studies presented here demonstrated that the FCS method was biocompatible for cancer cell separation and could enable downstream characterization of separated CTCs.

5.4.4 Enrichment of CTCs from NSCLC Patient Blood Using FCS

There was a large variance in reported numbers of captured CTCs for advanced metastatic cancer patients.[164] The exact reasons for this variance are still an area of active research. Nonetheless, most CTC separation methods chose to use blood from advanced metastatic patients for technology validation.[3, 166, 170-173, 184, 185, 189, 190] As a clinical validation of this method, we validated FCS devices with blood samples obtained from two patients with advanced NSCLC. Peripheral blood was collected from patients with newly diagnosed NSCLC (stage IVB) before initiation of treatment. Blood was lysed to remove RBCs and then processed with FCS devices within 3 hours of blood draw. 6.5 mL of blood was processed from patient A, and 5.6 mL of blood was processed from patient B. After separation, cells from FCS device's outlet 6 were directly preserved in

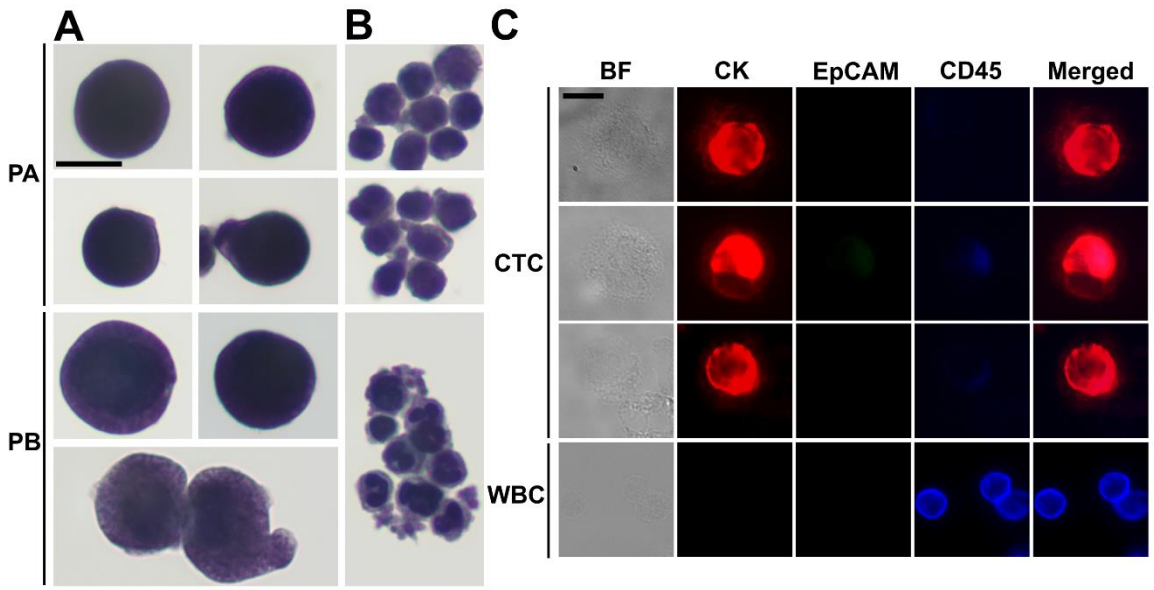

Figure 5.15: Enrichment of CTCs from NSCLC patient blood using FCS devices, and CTC identification with cytopathology and immunofluorescent staining. CTCs (a) and WBCs (b) from the blood of two NSCLC patients (PA and PB) were enriched by FCS devices and stained with Papanicolaou procedure, then identified by a cytopathologist. (c) Immunofluorescence images of enriched cells from blood samples from patient B. Three channels including CK, EpCAM and CD45 were examined. Cells were identified as CTCs if the staining pattern is CK+/CD45- or EpCAM+/CD45- or CK+/EpCAM+/CD45-, WBC were identified as CK-/EpCAM-/CD45+. Scale bars: 10 μm.

ThinPrep PreservCyt solution. These enriched cells were concentrated and stained using the Pap stain, which was commonly used for cytopathology analysis of clinical samples. Enriched cells were then inspected by a cytopathologist and CTCs were enumerated. Criteria used to identify CTC were as follows: (1) large cells with high nuclear to cytoplasmic ratio; (2) cells with irregular chromatin distribution and nuclear contours; (3) cells that are 4-5 times the size of a WBC. Figure 5.15a and Figure 5.16 shows a few Pap-stained CTCs and WBCs separated from two NSCLC patients. Both patients showed high CTC counts through cytopathology: 1165 and 369 CTCs were identified from 6.5 and 5.6 mL of blood samples, respectively. Purity of CTCs (defined as the number of

identified CTCs over the total number of cells from FCS device's collection outlets) from these two patients was 17.0±7.8%. Additionally, Immunofluorescent staining of CK8/18/19, EpCAM, and leukocyte marker CD45 was also used to confirm the presence CTCs separated from patient B's blood. Cells were identified as CTCs if the staining pattern is CK+/CD45- or EpCAM+/CD45- or CK+/EpCAM+/CD45-, otherwise, cells were identified as WBCs. Typical fluorescent images are shown in Figure 5.15b based on this immunostaining detection criteria.

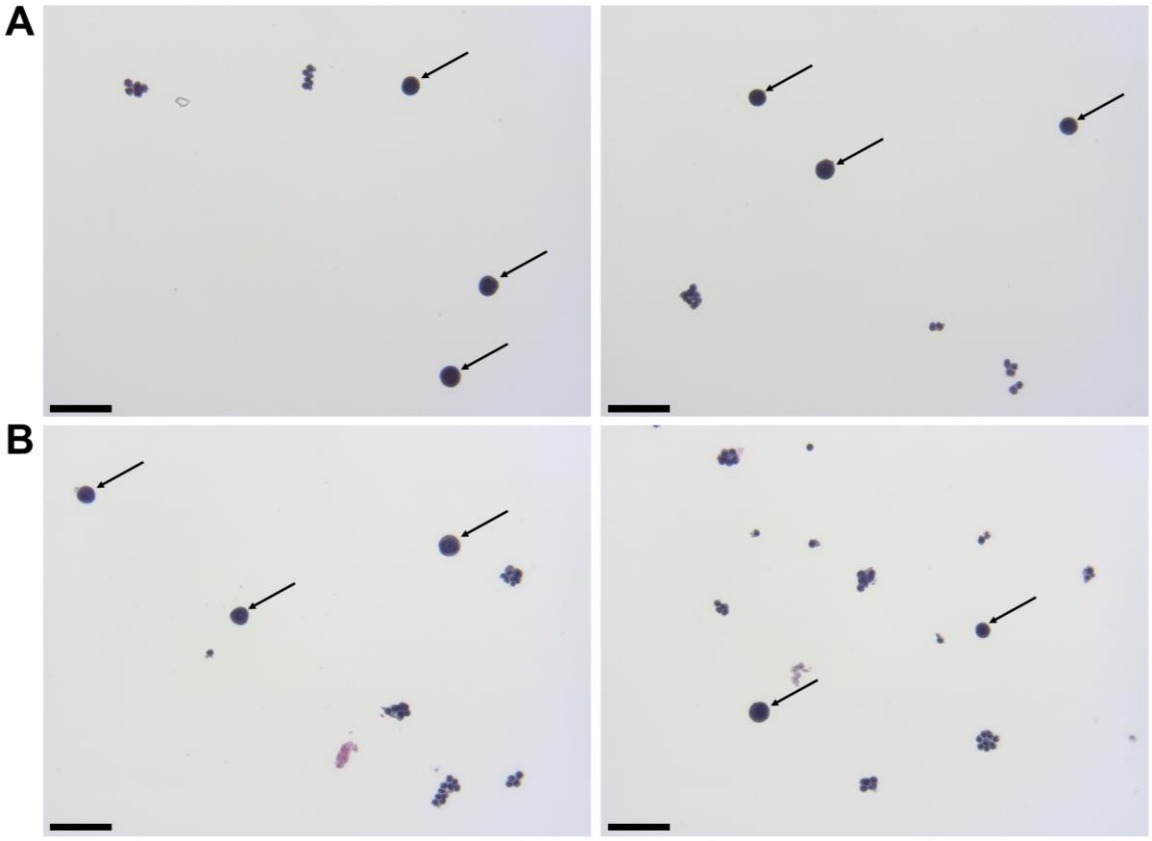

Figure 5.16: Representative images of CTC identification from patient A and B, with their blood processed by FCS devices. Black arrows indicate the identified CTCs. Scale bars: 50 µm.

5.5 Discussion

In this paper, we developed a ferrohydrodynamic cell separation (FCS) method for CTC separation and its devices that were capable of high-throughput (6 mL h^{-1}), high recovery rate (92.9%, an average from 6 cancer cell lines at ~100 cells mL^{-1} spike ratio) and biocompatible enrichment of cancer cells from RBC-lysed blood with an average 11.7% purity, by systematically investigating the device operating parameters on its separation performance. The FCS process involved multiple parameters that could affect the cell separation performance, including cell flow rates, magnetic fields and its gradient, ferrofluid concentrations and compositions. All of these parameters were highly coupled with each other and required an effective model for device optimization. We have developed and validated such an analytical model that considered magnetic buoyancy force, hydrodynamic drag force, laminar flow profiles and cancer/blood cell physical properties to guide the optimization and design of a high-throughput, high recovery rate FCS devices. We also considered the chemical makeup of the ferrofluids, including its nanoparticle concentration, pH value, nanoparticle size and surfactant, tonicity to optimize a colloidally stable and biocompatible ferrofluid suitable for cancer cell separation. After systematic optimization, we demonstrated that FCS devices were capable of separating various types of low-concentration cancer cells of cultured cell lines (~100 cells mL^{-1}) from WBCs under a flow rate of 6 mL h^{-1}. The recovery rates of spiked cancer cells were on average 92.9% from all tested cell lines at clinically relevant CTC occurrence rates. The recovered cancer cells were viable, could proliferate to confluence and expressions of a few key biomarker remained unaffected. These results indicated the practical use of this method in separating CTCs from patient blood were

feasible. We further demonstrated FCS devices worked well with clinical samples by successfully separating and identifying CTCs from blood samples of two late-stage (IVB) non-small cell lung cancer patients.

While current FCS devices demonstrated a high-recovery and biocompatible separation of rare cancer cells at a clinically relevant throughput, and was validated with NSCLC patient blood, it was still at its early stage of development and could benefit from further system optimization or integration with other methods in order to achieve high-throughput, high-recovery, high-purity separation of intact CTCs. When comparing FCS performance to other size-based label-free CTC separation methods, its rate of recovery of cancer cells was higher than the current average reported value of 82%,[157] including methods based on standing surface acoustic wave (>83%),[166] dean flow (>85%),[170, 184, 185] vortex technology (up to 83%),[171-173] and deterministic lateral displacement (>85%).[203] Although the throughput of current FCS device (6 mL h^{-1}) was sufficiently high to process clinically relevant amount of blood, it was slower than a few hydrodynamics-based methods that had extremely high flow rates, including the dean flow (56.25 mL h^{-1}),[170, 184, 185] the vortex technology (48 mL h^{-1}),[171-173] and DLD (10 mL min^{-1}).[203] Further system optimization, scale-up or multiplexing of FCS devices should be conducted in order to process more blood quickly. The average purity of separated cancer cells in current FCS devices was 11.7%. Reported purity values varied dramatically from 0.1% to 90% in label-free methods,[166-173, 184, 185] as most of them focused on improving recovery instead of purification of rare cells. Nonetheless, hydrodynamics-based methods including the dean flow (50%)[170, 184, 185] and the vortex technology (57-94%)[171-173] reported significantly higher purity of cancer cells in their collection outputs than FCS.

Low cancer cell purity due to WBC or other cell contamination could interfere with subsequent CTC characterization. It is therefore necessary for future FCS devices to further deplete these contamination cells.

FCS currently distinguished cells primarily based on their size difference. For cancer cells that have similar size as WBCs, this method will result in lower separated cancer cell purity than label-based method. Additional cell characteristics or methods could be integrated with FCS to further improve the purity of separated cancer cells. One possible strategy is for future FCS devices to exploit both size and magnetic labels of cells for CTC separation.[125] For example, WBCs in blood can be labeled with sufficient number of anti-CD45 magnetic beads so that the overall magnetization of the WBC-bead complex $\vec{M}_{WBC-Bead}$ is larger than its surrounding ferrofluids $\vec{M}_f$. The direction of magnetic force on the complex is then pointing towards magnetic field maxima. On the other hand, magnetization of the non-labeled CTCs $\vec{M}_{CTC}$ is zero and less than its surrounding ferrofluids $\vec{M}_f$, the direction of magnetic force on CTCs is therefore pointing towards magnetic field minima. In this scenario, both label-based magnetophoresis and size-based FCS co-exist in one system, i.e., $\vec{M}_{CTC-bead} > \vec{M}_f > \vec{M}_{CTC}$, magnetic force will attract WBC-bead complex towards field maxima while pushes CTCs towards field minima.

5.6 Conclusions

In this study, we reported a label-free ferrohydrodynamic cell separation (FCS) method that used magnetic buoyance force for size-based CTC separation, which was biocompatible and could enrich rare CTCs from patient blood with a high throughput and a high rate of recovery. We performed systematic optimization of this method and

determined parameters in a laminar flow microfluidic device that achieved an average 92.9% recovery rate and an average 11.7% purity of low-concentration (~100 cells mL^{-1}) cancer cells using six different cultured cell lines from undiluted WBCs, with a clinically relevant processing throughput of 6 mL of per hour. These parameters include magnetic field and its gradient (magnetic field: 443 mT, magnetic field gradient: 56.2 T m^{-1}), and ferrofluid concentration (0.26%, v/v). Specifically, for each cell lines at ~100 cells mL^{-1} spike ratio, the recovery rates of cancer cells were 92.3±3.6% (H1299 lung cancer), 88.3±5.5% (A549 lung cancer), 93.7±5.5% (H3122 lung cancer), 95.3±6.0% (PC-3 prostate cancer), 94.7±4.0% (MCF-7 breast cancer), and 93.0±5.3% (HCC1806 breast cancer), and the corresponding purities of separated cancer cells were 11.1%±1.2% (H1299 lung cancer), 10.1±1.7% (A549 lung cancer), 12.1±2.1% (H3122 lung cancer), 12.8±1.6% (PC-3 prostate cancer), 11.9±1.8% (MCF-7 breast cancer), and 12.2±1.6% (HCC1806 breast cancer). Separated H1299 lung cancer cells from FCS showed a short-term viability of 96.3±0.9%, and they were successfully cultured and demonstrated normal proliferation to the confluence. Separated HCC1806 breast cancer cells from FCS showed unchanged expressions of two key biomarkers including EpCAM and CK. FCS devices were validated with blood samples obtained from two patients with advanced NSCLC. 1165 CTCs were enriched and identified from 6.5 mL of blood samples from one patient, while 369 CTCs were enriched and identified from 5.6 mL of blood samples from the other patient. Although FCS is still at its early stage of development, it could be a complementary tool for rare cell separations because of its high recovery rate and excellent biocompatibility, as well as its potential for further optimization and integration with other compatible methods.

REFERENCES

1. S. K. Arya, B. Lim and A. R. A. Rahman, *Lab on a Chip*, 2013, **13**, 1995-2027.
2. P. Li, Z. S. Stratton, M. Dao, J. Ritz and T. J. Huang, *Lab on a Chip*, 2013, **13**, 602-609.
3. S. Nagrath, L. V. Sequist, S. Maheswaran, D. W. Bell, D. Irimia, L. Ulkus, M. R. Smith, E. L. Kwak, S. Digumarthy, A. Muzikansky, P. Ryan, U. J. Balis, R. G. Tompkins, D. A. Haber and M. Toner, *Nature*, 2007, **450**, 1235-1239.
4. L. Yu, S. R. Ng, Y. Xu, H. Dong, Y. Wang and C. M. Li, *Lab on a Chip*, 2013, **13**, 3163-3182.
5. J. Chen, J. Li and Y. Sun, *Lab on a Chip*, 2012, **12**, 1753-1767.
6. C. W. Yung, J. Fiering, A. J. Mueller and D. E. Ingber, *Lab on a Chip*, 2009, **9**, 1171-1177.
7. J. H. Kang, S. Krause, H. Tobin, A. Mammoto, M. Kanapathipillai and D. E. Ingber, *Lab on a Chip*, 2012, **12**, 2175-2181.
8. A. J. Mach and D. Di Carlo, *Biotechnol Bioeng*, 2010, **107**, 302-311.
9. A. M. Foudeh, T. F. Didar, T. Veres and M. Tabrizian, *Lab on a Chip*, 2012, **12**, 3249-3266.
10. Y. Zheng, J. Nguyen, Y. Wei and Y. Sun, *Lab on a Chip*, 2013, **13**, 2464-2483.
11. D. H. Kim, P. K. Wong, J. Park, A. Levchenko and Y. Sun, *Annu Rev Biomed Eng*, 2009, **11**, 203-233.

12. V. Lecault, A. K. White, A. Singhal and C. L. Hansen, *Curr Opin Chem Biol*, 2012, **16**, 381-390.

13. W. A. Bonner, H. R. Hulett, R. G. Sweet and L. A. Herzenberg, *Rev Sci Instrum*, 1972, **43**, 404-409.

14. D. R. Gossett, W. M. Weaver, A. J. Mach, S. C. Hur, H. T. K. Tse, W. Lee, H. Amini and D. Di Carlo, *Anal Bioanal Chem*, 2010, **397**, 3249-3267.

15. X. L. Mao and T. J. Huang, *Lab on a Chip*, 2012, **12**, 4006-4009.

16. N. Pamme, *Lab on a Chip*, 2007, **7**, 1644-1659.

17. H. Tsutsui and C. M. Ho, *Mech Res Commun*, 2009, **36**, 92-103.

18. A. Lenshof and T. Laurell, *Chem Soc Rev*, 2010, **39**, 1203-1217.

19. J. Voldman, *Annu Rev Biomed Eng*, 2006, **8**, 425-454.

20. D. G. Grier, *Nature*, 2003, **424**, 810-816.

21. F. Petersson, L. Aberg, A. M. Sward-Nilsson and T. Laurell, *Anal Chem*, 2007, **79**, 5117-5123.

22. N. Pamme, *Lab on a Chip*, 2006, **6**, 24-38.

23. C. X. Liu, T. Stakenborg, S. Peeters and L. Lagae, *J Appl Phys*, 2009, **105**, 102014.

24. M. A. M. Gijs, F. Lacharme and U. Lehmann, *Chem Rev*, 2010, **110**, 1518-1563.

25. N. T. Nguyen, *Microfluid Nanofluid*, 2012, **12**, 1-16.

26. T. B. Jones, *Electromechanics of Particles*, Cambridge University Press, Cambridge, UK, 1995.

27. R. E. Rosensweig, *Ferrohydrodynamics*, Cambridge University Press, Cambridge, UK, 1985.

28. S. S. Shevkoplyas, A. C. Siegel, R. M. Westervelt, M. G. Prentiss and G. M. Whitesides, *Lab on a Chip*, 2007, **7**, 1294-1302.

29. M. Hejazian, W. H. Li and N. T. Nguyen, *Lab on a Chip*, 2015, **15**, 959-970.

30. N. Pamme and A. Manz, *Anal Chem*, 2004, **76**, 7250-7256.

31. A. I. Rodriguez-Villarreal, M. D. Tarn, L. A. Madden, J. B. Lutz, J. Greenman, J. Samitier and N. Pamme, *Lab on a Chip*, 2011, **11**, 1240-1248.

32. D. Robert, N. Pamme, H. Conjeaud, F. Gazeau, A. Iles and C. Wilhelm, *Lab on a Chip*, 2011, **11**, 1902-1910.

33. N. Pamme and C. Wilhelm, *Lab on a Chip*, 2006, **6**, 974-980.

34. M. D. Tarn, S. A. Peyman, D. Robert, A. Iles, C. Wilhelm and N. Pamme, *J Magn Magn Mater*, 2009, **321**, 4115-4122.

35. G. Mihajlovic, K. Aledealat, P. Xiong, S. Von Molnar, M. Field and G. J. Sullivan, *Appl Phys Lett*, 2007, **91**, 172518.

36. K. van Ommering, J. H. Nieuwenhuis, L. J. van IJzendoorn, B. Koopmans and M. W. J. Prins, *Appl Phys Lett*, 2006, **89**, 142511.

37. Y. Jing, N. Mal, P. S. Williams, M. Mayorga, M. S. Penn, J. J. Chalmers and M. Zborowski, *Faseb J*, 2008, **22**, 4239-4247.

38. A. R. Kose, B. Fischer, L. Mao and H. Koser, *P Natl Acad Sci USA*, 2009, **106**, 21478-21483.

39. M. D. Krebs, R. M. Erb, B. B. Yellen, B. Samanta, A. Bajaj, V. M. Rotello and E. Alsberg, *Nano Lett*, 2009, **9**, 1812-1817.

40. S. A. Peyman, E. Y. Kwan, O. Margarson, A. Iles and N. Pamme, *Journal of Chromatography A*, 2009, **1216**, 9055-9062.

41. F. Shen, H. Hwang, Y. K. Hahn and J. K. Park, *Anal Chem*, 2012, **84**, 3075-3081.

42. T. T. Zhu, F. Marrero and L. D. Mao, *Microfluid Nanofluid*, 2010, **9**, 1003-1009.

43. A. T. Skjeltorp, *Phys Rev Lett*, 1983, **51**, 2306-2309.

44. T. T. Zhu, R. Cheng, S. A. Lee, E. Rajaraman, M. A. Eiteman, T. D. Querec, E. R. Unger and L. D. Mao, *Microfluid Nanofluid*, 2012, **13**, 645-654.

45. A. Winkleman, K. L. Gudiksen, D. Ryan, G. M. Whitesides, D. Greenfield and M. Prentiss, *Appl Phys Lett*, 2004, **85**, 2411-2413.

46. T. T. Zhu, D. J. Lichlyter, M. A. Haidekker and L. D. Mao, *Microfluid Nanofluid*, 2011, **10**, 1233-1245.

47. G. P. Krishnan and D. T. Leighton Jr, *Physics of Fluids*, 1995, **7**, 2538-2545.

48. M. E. Staben, A. Z. Zinchenko and R. H. Davis, *Physics of Fluids*, 2003, **15**, 1711-1733.

49. Y. Iiguni, M. Suwa and H. Watarai, *Journal of Chromatography A*, 2004, **1032**, 165-171.

50. P. Ganatos, R. Pfeffer and S. Weinbaum, *Journal of Fluid Mechanics*, 1980, **99**, 755-783.

51. S. Odenbach, *Magnetoviscous Effects in Ferrofluids*, Springer, New York, 2002.

52. A. Winkleman, R. Perez-Castillejos, K. L. Gudiksen, S. T. Phillips, M. Prentiss and G. M. Whitesides, *Anal Chem*, 2007, **79**, 6542-6550.

53. K. A. Mirica, S. T. Phillips, S. S. Shevkoplyas and G. M. Whitesides, *J Am Chem Soc*, 2008, **130**, 17678-17680.

54. K. A. Mirica, S. S. Shevkoplyas, S. T. Phillips, M. Gupta and G. M. Whitesides, *J Am Chem Soc*, 2009, **131**, 10049-10058.

55. N. D. Shapiro, K. A. Mirica, S. Soh, S. T. Phillips, O. Taran, C. R. Mace, S. S. Shevkoplyas and G. M. Whitesides, *J Am Chem Soc*, 2012, **134**, 5637-5646.

56. S. Tasoglu, J. A. Khoory, H. C. Tekin, C. Thomas, A. E. Karnoub, I. C. Ghiran and U. Demirci, *Adv Mater*, 2015, **27**, 3901-3908.

57. N. D. Shapiro, S. Soh, K. A. Mirica and G. M. Whitesides, *Anal Chem*, 2012, **84**, 6166-6172.

58. D. H. Carr, J. Brown, G. M. Bydder, R. E. Steiner, H. J. Weinmann, U. Speck, A. S. Hall and I. R. Young, *Am J Roentgenol*, 1984, **143**, 215-224.

59. R. B. Lauffer, *Chem Rev*, 1987, **87**, 901-927.

60. E. Kanal, K. Maravilla and H. A. Rowley, *Am J Neuroradiol*, 2014, **35**, 2215-2226.

61. N. G. Durmus, C. Tekin, S. Guven, K. Sridhar, A. A. Yildiz, G. Calibasi, I. Ghiran, R. W. Davis, L. M. Steinmetz and U. Demirci, *P Natl Acad Sci USA*, 2015, **112**, 3661-3668.

62. S. Knowlton, C. H. Yu, N. Jain, I. C. Ghiran and S. Tasoglu, *Plos One*, 2015, **10**, 134400.

63. M. Baday, S. Calamak, N. G. Durmus, R. W. Davis, L. M. Steinmetz and U. Demirci, *Small*, 2015, **12**, 1222-1229.

64. D. K. Bwambok, M. M. Thuo, M. B. Atkinson, K. A. Mirica, N. D. Shapiro and G. M. Whitesides, *Anal Chem*, 2013, **85**, 8442-8447.

65. N. V. Plechkova and K. R. Seddon, *Chem Soc Rev*, 2008, **37**, 123-150.

66. P. Brown, A. Bushmelev, C. P. Butts, J.-C. Eloi, I. Grillo, P. J. Baker, A. M. Schmidt and J. Eastoe, *Langmuir*, 2013, **29**, 3246-3251.

67. S. Hayashi and H.-o. Hamaguchi, *Chemistry Letters*, 2004, **33**, 1590-1591.

68. U. T. Andres, *Materials Science and Engineering*, 1976, **26**, 269-275.

69. M. D. Tarn, N. Hirota, A. Iles and N. Pamme, *Sci Technol Adv Mat*, 2009, **10**, 014611.

70. M. D. Tarn, S. A. Peyman and N. Pamme, *RSC Advances*, 2013, **3**, 7209-7214.

71. M. Vojtisek, M. D. Tarn, N. Hirota and N. Pamme, *Microfluid Nanofluid*, 2012, **13**, 625-635.

72. M. S. Martina, J. P. Fortin, C. Menager, O. Clement, G. Barratt, C. Grabielle-Madelmont, F. Gazeau, V. Cabuil and S. Lesieur, *J Am Chem Soc*, 2005, **127**, 10676-10685.

73. S. J. Lee, J. R. Jeong, S. C. Shin, J. C. Kim, Y. H. Chang, Y. M. Chang and J. D. Kim, *J Magn Magn Mater*, 2004, **272**, 2432-2433.

74. M. D. Shultz, S. Calvin, P. P. Fatouros, S. A. Morrison and E. E. Carpenter, *J Magn Magn Mater*, 2007, **311**, 464-468.

75. Q. A. Pankhurst, J. Connolly, S. K. Jones and J. Dobson, *J Phys D Appl Phys*, 2003, **36**, R167-R181.

76. Q. A. Pankhurst, N. T. K. Thanh, S. K. Jones and J. Dobson, *J Phys D Appl Phys*, 2009, **42**, 224001.

77. E. H. Kim, H. S. Lee, B. K. Kwak and B. K. Kim, *J Magn Magn Mater*, 2005, **289**, 328-330.

78. R. Y. Hong, B. Feng, L. L. Chen, G. H. Liu, H. Z. Li, Y. Zheng and D. G. Wei, *Biochem Eng J*, 2008, **42**, 290-300.

79. C. Alexiou, W. Arnold, P. Hulin, R. J. Klein, H. Renz, F. G. Parak, C. Bergemann and A. S. Lubbe, *J Magn Magn Mater*, 2001, **225**, 187-193.

80. S. Odenbach, *Ferrofluids: Magnetically Controllable Fluids and Their Applications*, Springer, London, 2002.

81. M. V. Berkovsky BM, Krakov MS *Magnetic Fluids: Engineering Applications*, Oxford University Press, New York, 1993.

82. R. M. Erb, H. S. Son, B. Samanta, V. M. Rotello and B. B. Yellen, *Nature*, 2009, **457**, 999-1002.

83. B. B. Yellen, O. Hovorka and G. Friedman, *P Natl Acad Sci USA*, 2005, **102**, 8860-8864.

84. K. H. Li and B. B. Yellen, *Appl Phys Lett*, 2010, **97**, 083105.

85. M. Kawano and H. Watarai, *Anal Bioanal Chem*, 2012, **403**, 2645-2653.

86. H. Watarai and M. Namba, *Analytical sciences*, 2001, **17**, 1233-1236.

87. H. Watarai and M. Namba, *Analytical Sciences*, 2002, **17**, 169-171.

88. H. Watarai and M. Namba, *Journal of chromatography A*, 2002, **961**, 3-8.

89. J. J. Zhu, L. T. Liang and X. C. Xuan, *Microfluid Nanofluid*, 2012, **12**, 65-73.

90. D. Huh, W. Gu, Y. Kamotani, J. B. Grotberg and S. Takayama, *Physiol Meas*, 2005, **26**, R73-R98.

91. T. D. Chung and H. C. Kim, *Electrophoresis*, 2007, **28**, 4511-4520.

92. X. C. Xuan, J. J. Zhu and C. Church, *Microfluid Nanofluid*, 2010, **9**, 1-16.

93. J. Zeng, Y. X. Deng, P. Vedantam, T. R. Tzeng and X. C. Xuan, *J Magn Magn Mater*, 2013, **346**, 118-123.

94. A. R. Kose and H. Koser, *Lab on a Chip*, 2012, **12**, 190-196.

95. W. Zhao, T. Zhu, R. Cheng, Y. Liu, J. He, H. Qiu, L. Wang, T. Nagy, T. D. Querec, E. R. Unger and L. Mao, *Advanced Functional Materials*, 2016, **26**, 3990-3998.

96. L. T. Liang and X. C. Xuan, *Biomicrofluidics*, 2012, **6**, 044106.

97. T. T. Zhu, R. Cheng and L. D. Mao, *Microfluid Nanofluid*, 2011, **11**, 695-701.

98. L. T. Liang, J. J. Zhu and X. C. Xuan, *Biomicrofluidics*, 2011, **5**, 034110.

99. L. T. Liang and X. C. Xuan, *Microfluid Nanofluid*, 2012, **13**, 637-643.

100. J. Zeng, C. Chen, P. Vedantam, T. R. Tzeng and X. C. Xuan, *Microfluid Nanofluid*, 2013, **15**, 49-55.

101. J. J. Wilbanks, G. Kiessling, J. Zeng, C. Zhang, T. R. Tzeng and X. C. Xuan, *J Appl Phys*, 2014, **115**, 044907.

102. Y. Zhou, D. T. Kumar, X. Lu, A. Kale, J. DuBose, Y. Song, J. Wang, D. Li and X. Xuan, *Biomicrofluidics*, 2015, **9**, 044102.

103. J. Zeng, C. Chen, P. Vedantam, V. Brown, T. R. J. Tzeng and X. C. Xuan, *J Micromech Microeng*, 2012, **22**, 105018.

104. T. T. Zhu, R. Cheng, G. R. Sheppard, J. Locklin and L. D. Mao, *Langmuir*, 2015, **31**, 8531-8534.

105. K. Zhang, Q. L. Liang, X. N. Ai, P. Hu, Y. M. Wang and G. A. Luo, *Lab on a Chip*, 2011, **11**, 1271-1275.

106. K. Zhang, Q. L. Liang, X. N. Ai, P. Hu, Y. M. Wang and G. A. Luo, *Anal Chem*, 2011, **83**, 8029-8034.

107. E. Furlani, *J Appl Phys*, 2006, **99**, 024912.

108. E. Furlani, *Journal of Physics D: Applied Physics*, 2007, **40**, 1313.

109. E. Furlani and Y. Sahoo, *Journal of Physics D: Applied Physics*, 2006, **39**, 1724.

110. R. Cheng, T. T. Zhu and L. D. Mao, *Microfluid Nanofluid*, 2014, **16**, 1143-1154.

111. X. T. Han, Y. Feng, Q. L. Cao and L. Li, *Microfluid Nanofluid*, 2015, **18**, 1209-1220.

112. L. Benz, K. E. Cesafsky, T. Le, A. Park and D. Malicky, *J Chem Educ*, 2012, **89**, 776-779.

113. K. A. Mirica, S. T. Phillips, C. R. Mace and G. M. Whitesides, *J Agr Food Chem*, 2010, **58**, 6565-6569.

114. E. Beaugnon and R. Tournier, *Nature*, 1991, **349**, 470.

115. E. Beaugnon and R. Tournier, *Journal de Physique III*, 1991, **1**, 1423-1428.

116. M. A. Weilert, D. L. Whitaker, H. J. Maris and G. M. Seidel, *Phys Rev Lett*, 1996, **77**, 4840-4843.

117. J. M. Valles, K. Lin, J. M. Denegre and K. L. Mowry, *Biophys J*, 1997, **73**, 1130-1133.

118. M. Motokawa, I. Mogi, M. Tagami, M. Hamai, K. Watanabe and S. Awaji, *Physica B*, 1998, **256**, 618-620.

119. A. B. Subramaniam, M. Gonidec, N. D. Shapiro, K. M. Kresse and G. M. Whitesides, *Lab on a Chip*, 2015, **15**, 1009-1022.

120. M. A. Weilert, D. L. Whitaker, H. J. Maris and G. M. Seidel, *J Low Temp Phys*, 1997, **106**, 101-131.

121. M. V. Berry and A. K. Geim, *European Journal of Physics*, 1997, **18**, 307.

122. S. Tasoglu, C. H. Yu, V. Liaudanskaya, S. Guven, C. Migliaresi and U. Demirci, *Adv Healthc Mater*, 2015, **4**, 1469-1476.

123. S. Knowlton, I. Sencan, Y. Aytar, J. Khoory, M. Heeney, I. Ghiran and S. Tasoglu, *Sci Rep*, 2015, **5**, 15022.

124. L. T. Liang, C. Zhang and X. C. Xuan, *Appl Phys Lett*, 2013, **102**, 234101.

125. T. T. Zhu, R. Cheng, Y. F. Liu, J. He and L. D. Mao, *Microfluid Nanofluid*, 2014, **17**, 973-982.

126. J. H. Kang, S. Choi, W. Lee and J. K. Park, *J Am Chem Soc*, 2008, **130**, 396-397.

127. Y. K. Hahn and J. K. Park, *Lab on a Chip*, 2011, **11**, 2045-2048.

128. P. Kauffmann, A. Ith, D. O'Brien, V. Gaude, F. Boue, S. Combe, F. Bruckert, B. Schaack, N. M. Dempsey, V. Haguet and G. Reyne, *Lab on a Chip*, 2011, **11**, 3153-3161.

129. J. M. Lang, B. P. Casavant and D. J. Beebe, *Sci Transl Med*, 2012, **4**, 141ps113.

130. C. Alix-Panabieres and K. Pantel, *Clinical chemistry*, 2013, **59**, 110-118.

131. R. Massart, *Ieee Transactions on Magnetics*, 1981, **17**, 1247-1248.

132. W. J. Zhao, R. Cheng, B. D. Jenkins, T. T. Zhu, N. E. Okonkwo, C. E. Jones, M. B. Davis, S. K. Kavuri, Z. L. Hao, C. Schroeder and L. D. Mao, *Lab on a Chip*, 2017, **17**, 3097-3111.

133. D. K. Hwang, D. Dendukuri and P. S. Doyle, *Lab Chip*, 2008, **8**, 1640-1647.

134. J. Huang, L. H. Bu, J. Xie, K. Chen, Z. Cheng, X. G. Li and X. Y. Chen, *Acs Nano*, 2010, **4**, 7151-7160.

135. N. Luciani, F. Gazeau and C. Wilhelm, *J Mater Chem*, 2009, **19**, 6373-6380.

136. D. L. J. Thorek and A. Tsourkas, *Biomaterials*, 2008, **29**, 3583-3590.

137. W. Jiang, B. Y. S. Kim, J. T. Rutka and W. C. W. Chan, *Nat Nanotechnol*, 2008, **3**, 145-150.

138. Q. Cao, X. Han and L. Li, *Lab Chip*, 2014, **14**, 2762-2777.

139. C. Lee, H. Lee and R. Westervelt, *Appl Phys Lett*, 2001, **79**, 3308-3310.

140. D. W. Inglis, R. Riehn, R. H. Austin and J. C. Sturm, *Appl Phys Lett*, 2004, **85**, 5093-5095.

141. C. X. Liu, L. Lagae and G. Borghs, *Appl Phys Lett*, 2007, **90**, 184109.

142. B. B. Yellen, R. M. Erb, H. S. Son, R. Hewlin, H. Shang and G. U. Lee, *Lab on a Chip*, 2007, **7**, 1681-1688.

143. Y. Yang, R. M. Erb, B. J. Wiley, S. Zauscher and B. B. Yellen, *Nano Lett*, 2011, **11**, 1681-1684.

144. K. S. Khalil, A. Sagastegui, Y. Li, M. A. Tahir, J. E. S. Socolar, B. J. Wiley and B. B. Yellen, *Nat Commun*, 2012, **3**, 794.

145. Y. Yang, L. Gao, G. P. Lopez and B. B. Yellen, *ACS Nano*, 2013, **7**, 2705-2716.

146. T. T. Puck, P. I. Marcus and S. J. Cieciura, *J Exp Med*, 1956, **103**, 273-283.

147. K. de Jong, R. K. Emerson, J. Butler, J. Bastacky, N. Mohandas and F. A. Kuypers, *Blood*, 2001, **98**, 1577-1584.

148. A. T. Moriarty, A. C. Clayton, S. Zaleski, M. R. Henry, M. R. Schwartz, G. M. Eversole, W. D. Tench, L. A. Fatheree, R. J. Souers and D. C. Wilbur, *Arch Pathol Lab Med*, 2009, **133**, 1912-1916.

149. H. Mitchell and G. Medley, *Cytopathology*, 1995, **6**, 368-375.

150. A. A. Renshaw, M. R. Henry, G. G. Birdsong, E. Wang, J. Haja and J. H. Hughes, *Archives of Pathology & Laboratory Medicine*, 2005, **129**, 1097-1099.

151. A. A. Renshaw, B. Dubray-Benstein, J. Haja, J. H. Hughes and C. o. A. P. Cytopathology Resource Committee, *Arch Pathol Lab Med*, 2005, **129**, 23-25.

152. Y. X. and and G. M. Whitesides, *Annual Review of Materials Science*, 1998, **28**, 153-184.

153. W. Zhao, R. Cheng, J. R. Miller and L. Mao, *Advanced Functional Materials*, 2016, **26**, 3916-3932.

154. B. Yenilmez, S. Knowlton and S. Tasoglu, *Advanced Materials Technologies*, 2016, **1**, 1600144-1600153.

155. U. Dharmasiri, M. A. Witek, A. A. Adams and S. A. Soper, *Annu Rev Anal Chem*, 2010, **3**, 409-431.

156. S. D. Conner and S. L. Schmid, *Nature*, 2003, **422**, 37-44.

157. Y. C. Chen, P. Li, P. H. Huang, Y. L. Xie, J. D. Mai, L. Wang, N. T. Nguyen and T. J. Huang, *Lab on a Chip*, 2014, **14**, 626-645.

158. G. P. Zhu, M. Hejiazan, X. Y. Huang and N. T. Nguyen, *Lab on a Chip*, 2014, **14**, 4609-4615.

159. M. D. Tarn, M. J. Lopez-Martinez and N. Pamme, *Anal Bioanal Chem*, 2014, **406**, 139-161.

160. M. Hejazian, D. T. Phan and N. T. Nguyen, *Rsc Advances*, 2016, **6**, 62439-62444.

161. M. Hejazian and N. T. Nguyen, *Micromachines-Basel*, 2017, **8**, 37.

162. Y. N. Xia and G. M. Whitesides, *Annual Review of Materials Science*, 1998, **28**, 153-184.

163. L. Mao and H. Koser, The 14th International Conference on Solid-State Sensors, Actuators and Microsystems, Lyon, France, 2007.

164. C. Alix-Panabieres and K. Pantel, *Nat Rev Cancer*, 2014, **14**, 623-631.

165. M. Yu, S. Stott, M. Toner, S. Maheswaran and D. A. Haber, *J Cell Biol*, 2011, **192**, 373-382.

166. P. Li, Z. M. Mao, Z. L. Peng, L. L. Zhou, Y. C. Chen, P. H. Huang, C. I. Truica, J. J. Drabick, W. S. El-Deiry, M. Dao, S. Suresh and T. J. Huang, *P Natl Acad Sci USA*, 2015, **112**, 4970-4975.

167. S. B. Huang, M. H. Wu, Y. H. Lin, C. H. Hsieh, C. L. Yang, H. C. Lin, C. P. Tseng and G. B. Lee, *Lab on a Chip*, 2013, **13**, 1371-1383.

168. P. R. C. Gascoyne, J. Noshari, T. J. Anderson and F. F. Becker, *Electrophoresis*, 2009, **30**, 1388-1398.

169. H. S. Moon, K. Kwon, S. I. Kim, H. Han, J. Sohn, S. Lee and H. I. Jung, *Lab on a Chip*, 2011, **11**, 1118-1125.

170. M. E. Warkiani, G. F. Guan, K. B. Luan, W. C. Lee, A. A. S. Bhagat, P. K. Chaudhuri, D. S. W. Tan, W. T. Lim, S. C. Lee, P. C. Y. Chen, C. T. Lim and J. Han, *Lab on a Chip*, 2014, **14**, 128-137.

171. J. Che, V. Yu, M. Dhar, C. Renier, M. Matsumoto, K. Heirich, E. B. Garon, J. Goldman, J. Y. Rao, G. W. Sledge, M. D. Pegram, S. Sheth, S. S. Jeffrey, R. P. Kulkarni, E. Sollier and D. Di Carlo, *Oncotarget*, 2016, **7**, 12748-12760.

172. M. Dhar, E. Pao, C. Renier, D. E. Go, J. Che, R. Montoya, R. Conrad, M. Matsumoto, K. Heirich, M. Triboulet, J. Y. Rao, S. S. Jeffrey, E. B. Garon, J. Goldman, N. P. Rao, R. Kulkarni, E. Sollier-Christen and D. Di Carlo, *Sci Rep*, 2016, **6**, 35474

173. E. Sollier, D. E. Go, J. Che, D. R. Gossett, S. O'Byrne, W. M. Weaver, N. Kummer, M. Rettig, J. Goldman, N. Nickols, S. McCloskey, R. P. Kulkarni and D. Di Carlo, *Lab on a Chip*, 2014, **14**, 63-77.

174. N. Aceto, M. Toner, S. Maheswaran and D. A. Haber, *Trends in Cancer*, 2015, **1**, 44-52.

175. J. Massague and A. C. Obenauf, *Nature*, 2016, **529**, 298-306.

176. M. Yu, A. Bardia, N. Aceto, F. Bersani, M. W. Madden, M. C. Donaldson, R. Desai, H. L. Zhu, V. Comaills, Z. L. Zheng, B. S. Wittner, P. Stojanov, E. Brachtel, D. Sgroi, R. Kapur, T. Shioda, D. T. Ting, S. Ramaswamy, G. Getz, A. J. Iafrate, C. Benes, M. Toner, S. Maheswaran and D. A. Haber, *Science*, 2014, **345**, 216-220.

177. M. Kalinich, I. Bhan, T. T. Kwan, D. T. Miyamoto, S. Javaid, J. A. LiCausi, J. D. Milner, X. Hong, L. Goyal, S. Sil, M. Choz, U. Ho, R. Kapur, A. Muzikansky, H. D. Zhang, D. A. Weitz, L. V. Sequist, D. P. Ryan, R. T. Chung, A. X. Zhu, K. J. Isselbacher, D. T. Ting, M. Toner, S. Maheswaran and D. A. Haber, *P Natl Acad Sci USA*, 2017, **114**, 1123-1128.

178. D. T. Miyamoto, D. T. Ting, M. Toner, S. Maheswaran and D. A. Haber, *Cold Spring Harbor symposia on quantitative biology*, 2016, **81**, 269-274.

179. M. Poudineh, P. Aldridge, S. Ahmed, B. J. Green, L. Kermanshah, V. Nguyen, C. Tu, R. M. Mohamadi, R. K. Nam, A. Hansen, S. S. Sridhar, A. Finelli, N. E. Fleshner, A. M. Joshua, E. H. Sargent and S. O. Kelley, *Nat Nanotechnol*, 2017, **12**, 274-281.

180. S. L. Stott, C. H. Hsu, D. I. Tsukrov, M. Yu, D. T. Miyamoto, B. A. Waltman, S. M. Rothenberg, A. M. Shah, M. E. Smas, G. K. Korir, F. P. Floyd, A. J. Gilman, J. B. Lord, D. Winokur, S. Springer, D. Irimia, S. Nagrath, L. V. Sequist, R. J. Lee, K. J. Isselbacher, S. Maheswaran, D. A. Haber and M. Toner, *P Natl Acad Sci USA*, 2010, **107**, 18392-18397.

181. A. H. Talasaz, A. A. Powell, D. E. Huber, J. G. Berbee, K. H. Roh, W. Yu, W. Z. Xiao, M. M. Davis, R. F. Pease, M. N. Mindrinos, S. S. Jeffrey and R. W. Davis, *P Natl Acad Sci USA*, 2009, **106**, 3970-3975.

182. V. Murlidhar, L. Rivera-Baez and S. Nagrath, *Small*, 2016, **12**, 4450-4463.

183. H. K. Lin, S. Y. Zheng, A. J. Williams, M. Balic, S. Groshen, H. I. Scher, M. Fleisher, W. Stadler, R. H. Datar, Y. C. Tai and R. J. Cote, *Clin Cancer Res*, 2010, **16**, 5011-5018.

184. H. W. Hou, M. E. Warkiani, B. L. Khoo, Z. R. Li, R. A. Soo, D. S. W. Tan, W. T. Lim, J. Han, A. A. S. Bhagat and C. T. Lim, *Sci Rep*, 2013, **3**, 1259

185. M. E. Warkiani, B. L. Khoo, L. D. Wu, A. K. P. Tay, A. A. S. Bhagat, J. Han and C. T. Lim, *Nat Protoc*, 2016, **11**, 134-148.

186. D. Marrinucci, K. Bethel, D. Lazar, J. Fisher, E. Huynh, P. Clark, R. Bruce, J. Nieva and P. Kuhn, *Journal of Oncology*, 2010, **2010**, 861341.

187. W. J. Allard, J. Matera, M. C. Miller, M. Repollet, M. C. Connelly, C. Rao, A. G. J. Tibbe, J. W. Uhr and L. W. M. M. Terstappen, *Clin Cancer Res*, 2004, **10**, 6897-6904.

188. Y. Dong, A. M. Skelley, K. D. Merdek, K. M. Sprott, C. Jiang, W. E. Pierceall, J. Lin, M. Stocum, W. P. Carney and D. A. Smirnov, *The Journal of molecular diagnostics : JMD*, 2013, **15**, 149-157.

189. N. M. Karabacak, P. S. Spuhler, F. Fachin, E. J. Lim, V. Pai, E. Ozkumur, J. M. Martel, N. Kojic, K. Smith, P. I. Chen, J. Yang, H. Hwang, B. Morgan, J. Trautwein, T. A. Barber, S. L. Stott, S. Maheswaran, R. Kapur, D. A. Haber and M. Toner, *Nat Protoc*, 2014, **9**, 694-710.

190. E. Ozkumur, A. M. Shah, J. C. Ciciliano, B. L. Emmink, D. T. Miyamoto, E. Brachtel, M. Yu, P. I. Chen, B. Morgan, J. Trautwein, A. Kimura, S. Sengupta, S. L. Stott, N. M. Karabacak, T. A. Barber, J. R. Walsh, K. Smith, P. S. Spuhler, J. P. Sullivan, R. J. Lee, D. T. Ting, X. Luo, A. T. Shaw, A. Bardia, L. V. Sequist, D. N. Louis, S. Maheswaran, R. Kapur, D. A. Haber and M. Toner, *Sci Transl Med*, 2013, **5**, 179ra147.

191. C. W. Shields, J. L. Wang, K. A. Ohiri, E. D. Essoyan, B. B. Yellen, A. J. Armstrong and G. P. Lopez, *Lab on a Chip*, 2016, **16**, 3833-3844.

192. C. Huang, H. Liu, N. H. Bander and B. J. Kirby, *Biomed Microdevices*, 2013, **15**, 941-948.

193. Z. B. Liu, W. Zhang, F. Huang, H. T. Feng, W. L. Shu, X. P. Xu and Y. Chen, *Biosens Bioelectron*, 2013, **47**, 113-119.

194. J. Kim, H. Cho, S. I. Han and K. H. Han, *Anal Chem*, 2016, **88**, 4857-4863.

195. B. D. Plouffe, M. Mahalanabis, L. H. Lewis, C. M. Klapperich and S. K. Murthy, *Anal Chem*, 2012, **84**, 1336-1344.

196. C. M. Earhart, C. E. Hughes, R. S. Gaster, C. C. Ooi, R. J. Wilson, L. Y. Zhou, E. W. Humke, L. Y. Xu, D. J. Wong, S. B. Willingham, E. J. Schwartz, I. L. Weissman, S. S. Jeffrey, J. W. Neal, R. Rohatgi, H. A. Wakeleebe and S. X. Wang, *Lab on a Chip*, 2014, **14**, 78-88.

197. K. Hoshino, Y. Y. Huang, N. Lane, M. Huebschman, J. W. Uhr, E. P. Frenkel and X. J. Zhang, *Lab on a Chip*, 2011, **11**, 3449-3457.

198. A. E. Saliba, L. Saias, E. Psychari, N. Minc, D. Simon, F. C. Bidard, C. Mathiot, J. Y. Pierga, V. Fraisier, J. Salamero, V. Saada, F. Farace, P. Vielh, L. Malaquin and J. L. Viovy, *P Natl Acad Sci USA*, 2010, **107**, 14524-14529.

199. L. Y. Yang, J. C. Lang, P. Balasubramanian, K. R. Jatana, D. Schuller, A. Agrawal, M. Zborowski and J. J. Chalmers, *Biotechnol Bioeng*, 2009, **102**, 521-534.

200. Y. Y. Huang, P. Chen, C. H. Wu, K. Hoshino, K. Sokolov, N. Lane, H. Y. Liu, M. Huebschman, E. Frenkel and J. X. J. Zhang, *Sci Rep*, 2015, **5**, 16047.

201. W. Zhao, R. Cheng, S. H. Lim, J. R. Miller, W. Zhang, W. Tang, J. Xie and L. Mao, *Lab Chip*, 2017, **17**, 2243-2255.

202. G. P. Krishnan and D. T. Leighton, *Physics of Fluids*, 1995, **7**, 2538-2545.

203. K. Loutherback, J. D'Silva, L. Y. Liu, A. Wu, R. H. Austin and J. C. Sturm, *Aip Adv*, 2012, **2**, 042107.